

THESIS FOR THE DEGREE OF DOCTOR OF PHILOSOPHY

Investigations of Strong Light-Matter Interactions in Nanophotonic Systems

MICHAEL STÜHRENBERG



Department of Physics

CHALMERS UNIVERSITY OF TECHNOLOGY

Gothenburg, Sweden 2019

Investigations of Strong Light-Matter Interactions in Nanophotonic Systems

MICHAEL STÜHRENBURG

ISBN 978-91-7905-146-4

© MICHAEL STÜHRENBURG, 2019.

Doktorsavhandlingar vid Chalmers tekniska högskola

Ny serie nr 4613

ISSN 0346-718X

Department of Physics

Chalmers University of Technology

SE-412 96 Gothenburg

Sweden

Telephone + 46 (0)31-772 1000

Cover: A gold nanobipyramid placed on an atomically thin tungsten diselenide bilayer. The system is excited by high energy light (blue) and emits and scatters light depending on the interaction strength of the two components.

Gothenburg, Sweden 2019

Investigations of Strong Light-Matter Interactions in Nanophotonic Systems

Michael Stührenberg

Department of Physics

Chalmers University of Technology

Abstract

Noble metal nanoparticles can support localized surface plasmon resonances (LSPR), thus behaving as open optical resonators. Outstanding optical properties as well as a subwavelength mode volume make plasmonic nanoparticles a promising platform for enhanced light-matter interactions. Light is focused to a nanoscale volume, so called ‘hot-spots’, resulting in strong electromagnetic field amplification in that region. An emitter placed in such a hot-spot can couple with the LSPR of the nanoparticle and thereby experience a dramatic change in its properties.

When the light-matter interaction becomes strong enough, the system enters a special regime, so-called *strong coupling*. In this regime, the cavity and emitter exchange their energy in a coherent manner on time scales that are faster than their respective dissipation rates. This leads to the formation of new hybrid light-matter states, referred to as polaritons. In this strong light-matter coupling regime, not only the optical but also material-related properties of the system can be modified.

The aim of this thesis is to show and discuss room temperature strong light-matter coupling as well as beneficial and limiting factors of the coupling process. Excitons in transition metal dichalcogenides (TMDC) are coupled to plasmonic resonances of individual gold nanobipyramids (BPs). Strong coupling of excitons and BPs in a single hot-spot is demonstrated. Subsequently, the asymmetric photoluminescence (PL) emission behavior of this hybrid system is investigated and discussed. Moreover, an interesting case of strong coupling arises when the TMDC material itself is made thick enough to support resonant Fabry-Pérot optical modes in the same frequency range as the exciton resonance. In such circumstances the excitons can be self-hybridized with the optical resonator made of the same material and thereby modify the absorption of the TMDC material over the whole visible spectrum.

In addition to the above-mentioned studies of strong coupling, nonlinear laser microscopy has been employed to study plasmonic, as well as biological samples. And finally, the effect of temporal PL coherence from a single plasmonic nanoparticle is demonstrated as well as different methods for sample analysis and understanding their limitations are discussed.

Keywords: *localized surface plasmon resonance, bipyramids, strong coupling, photoluminescence*

LIST OF PUBLICATIONS

This thesis is based on the work contained in the following publications:

Paper I:

Strong Light–Matter Coupling between Plasmons in Individual Gold Bi-pyramids and Excitons in Mono- and Multilayer WSe₂

M. Stührenberg, B. Munkhbat, D. G. Baranov, J. Cuadra, A. B. Yankovich, T. J. Antosiewicz, E. Olsson, T. Shegai

Nano letters, **2018**, 18 (9), 5938-5945

Paper II:

Self-Hybridized Exciton-Polaritons in Multilayers of Transition Metal Dichalcogenides for Efficient Light Absorption

B. Munkhbat, D. G. Baranov, **M. Stührenberg**, M. Wersäll, A. Bisht, T. Shegai,

ACS Photonics, **2019**, 6 (1), pp 139–147

Paper III:

Asymmetric photoluminescence from upper and lower polariton in a strongly coupled single nanoparticle plasmon mono- and bilayer WSe₂ system

M. Stührenberg, B. Munkhbat, D. G. Baranov, T. J. Antosiewicz, T. Shegai,

Manuscript **2019**

Paper IV:

Phase control of plasmon enhanced two-photon photoluminescence in resonant gold nanoantennas

V. Remesh, **M. Stührenberg**, L. Saemisch, N. Accanto, and N. F. van Hulst,

Appl. Phys. Lett. 113, 211101 (**2018**)

Paper V:

Micro- and nano-patterned elastin-like polypeptide hydrogels for stem cell culture

A. Paul,[‡] **M. Stührenberg**,[‡] S. Chen, D. Rhee, W.-K. Lee, T. W. Odom, S. C. Heilshorn, and A. Enejder,

Soft Matter, **2017**, 13, 5665 (‡ denotes equal contributions)

Declaration of Author Contribution

Paper I:

I planned the project, performed the sample preparation, dark-field, reflection and SEM measurements. I coordinated corresponding theoretical models and calculations. Finally, I analyzed the data and wrote the first draft of the manuscript.

Paper II:

I participated in the project discussions and normal incidence reflectivity measurements. I performed all AFM measurements for this project. Furthermore, I co-wrote the final manuscript.

Paper III:

I planned the project, performed the sample preparation, dark-field, reflection, photoluminescence and SEM measurements. Moreover, I conducted the data analysis and wrote the first draft of the manuscript.

Paper IV:

I participated in the project planning and discussions. Together with V. Remesh we executed the experiments and data analysis. I helped correcting the final manuscript.

Paper V:

A. Paul and I planned the project. I performed several CARS measurements, all AFM measurements and devised a way to analyze the data automatically. Finally, I co-wrote the manuscript.

Table of Contents

Chapter 1: Introduction.....	1
Chapter 2: Optical Properties of Plasmonic Nanoparticles and TMDC	5
2.1 Optical resonators	5
2.2 Plasmonic particles as open optical resonators	6
2.2.1 Free electrons in a metal, a Drude model approximation.....	7
2.2.2 Localized surface plasmon resonance	10
2.2.3 Surface plasmon polariton	14
2.2.3 Nanoholes in a thin metal film.....	15
2.3 Transition metal dichalcogenides	17
2.3.1 From bulk to monolayer	17
2.3.2 Excitons in TMDC	20
Chapter 3: Light-Matter Interactions	23
3.1 Coherent and incoherent interactions	24
3.2 Classical coupled harmonic oscillator model.....	25
3.3 Coupled mode theory.....	31
3.4 Anti-crossing characteristics	33
3.5 A notion of quantum.....	40
3.6 Photoluminescence of a strongly coupled system	41
3.6.1 Upper polariton decay to the incoherent states	42
3.6.2 Incoherent states decay to lower polariton	44
Chapter 4: Experimental Methodology.....	49
4.1 Sample preparation of BPs, TMDC and colloidal lithography	49
4.1.1 Fabrication of hybrid structures	49
4.1.2 Hole colloidal lithography	51
4.1.3 Synthesis of gold nanobipyramids	55

4.2 Atomic force microscopy	56
4.3 Dark-field microscopy	57
4.4 Photoluminescence microscopy	60
4.5 Hyperspectral imaging system	62
4.6 Electron microscopy	65
4.7 Reflectivity measurements	66
4.8 Nonlinear laser microscopy	66
4.8.1 Introduction to different nonlinear laser microscopy methods	69
4.8.2 Nonlinear laser microscope	73
4.8.2 Plasmon enhanced four-wave mixing	76
4.8.3 Near- and far-field microscopy	80
Chapter 5: Summary and Outlook	83
5.1 Discussion of appended papers	83
5.2 Outlook	87
Acknowledgements	91
BIBLIOGRAPHY	95

Chapter 1: Introduction

Seeing is believing. Being able to see is crucial for understanding our environment. Light is detected by our eyes and converted into electric signals. These signals travel to the brain, where this information is interpreted as color and shapes. This is just one example of the interaction between light and matter. In general, light-matter interactions take place on all different length-scales from whole planets down to a single atom. However, our ability to resolve small objects is limited. The first big milestone in understanding light-matter interactions has been achieved with the invention of the microscope. A new regime got accessible and for the first time, cells and other small building blocks in nature have been found and investigated. The minimum resolvable distance has been postulated by Ernst Abbe and Hermann Helmholtz [1, 2] at the end of the 19th century, as the diffraction limit of light:

$$d \approx \frac{\lambda}{2NA} \quad (1.1)$$

d the smallest resolvable distance between two point-sources, depends on the wavelength λ and the light acceptance cone of the optical system, the numerical aperture (NA). In the visible region of light this leads to a maximum resolution of around $d_{max} \approx 200 \text{ nm}$. Higher resolution can be achieved by employing even shorter wavelengths, such as X-rays, or electrons instead of light. However, most of these methods are potentially harmful for the system under study and require expensive specialized equipment.

An alternative route, for investigating or manipulating light-matter interactions, emerged with nanoscience and fabrication. Decreasing the size of an object below the wavelength of light changes the surface to volume ratio, which can lead to drastic changes in optical and material related properties and result in completely new physics, such as localized surface plasmon resonances (LSPR). Noble metal nanoparticles support LSPRs, which are coherent oscillations of the particles surface-electrons. Incident light is focused to a nanoscale volume, resulting in strong electromagnetic field intensities, so-called *hot-spots*. Therefore, the particle acts as an open resonator for light-matter interaction. LSPRs dictate many optical properties of the particle, such as absorption and scattering of light, and are very sensitive to the dielectric properties of the surrounding environment. Therefore, plasmonic particles have attracted a huge amount of interest and their applicability ranges from cancer treatment [3], cell imaging [4, 5], biosensing [6] to data storage [7], quantum optics [8, 9], optoelectronics [10, 11] and

energy harvesting [12]. The plasmonic properties of a nanoparticle depend on the material, size and shape, giving access to a precise tunability of its function. Nowadays, a plethora of various fabrication methods, such as electron beam lithography [13], hole colloidal lithography [14], seed-mediated growth [15-17] and drop-casting from solution [18], enable scientists to create a whole zoo of particles at the nanoscale.

Placing an emitter, with a resonance matching the LSPR, inside the hot-spot of a metal nanoparticle, enables coupling of the plasmon resonance to the electronic transitions of the emitter. Such a light-matter interaction may be categorized in two different regimes, depending on the coupling strength between the resonator and emitter. In case of a weak light-matter coupling, the emitter experiences a modified density of photonic states. This leads to alterations of the spontaneous emission rates, the so-called Purcell effect [19, 20]. This becomes very different in the so-called *strong coupling regime*. When the interaction between resonator and emitter becomes stronger, the plasmonic and emitter modes lead to a perturbation of the individual wave functions [21]. The rate of coherent energy exchange between matter and optical excitations becomes faster than any of their intrinsic dissipation rates. The energy can oscillate back and forth several times, between resonator and emitter, before decaying radiatively or non-radiatively to the surrounding environment. This oscillation is called Rabi oscillation and results in the splitting of the original (degenerate) modes into new indistinguishable mixtures of light and matter, so-called *polaritons*. The hybrid character of the polaritons can lead to dramatically modified optical and material related properties.

The term polariton has been defined and coined a long time ago by Fano (1956) [22] and Hopfield (1958) [23], with the polariton being a strongly coupled light-matter quasiparticle. Historically, strong coupling of a resonator with an active medium, has been demonstrated already in 1983 with a collection of Rydberg atoms in a resonant millimeter wave cavity by Haroche et al. [24]. Since then, it has attracted a tremendous amount of research interest.

What makes strong light-matter coupling so interesting, is the fact that it merges two different fields of physics, namely *quantum optics* and *material science*. From the optical perspective, strong coupling has enabled ultrafast optical switches [25], photon blockade [26], quantum information processing [27] and Bose-Einstein condensates [28]. From the material science perspective, strong coupling can also modify photophysical and photochemical processes. The formation of new polaritonic states can lead to modification of molecular relaxation pathways

and dynamics in the strong coupling regime and thereby increase the photostability of molecules, as shown by Munkhbat et al. [29] and Peters et al. [30]. Strong coupling can also modify chemical reaction rates as demonstrated by Ebbesen et al. [31-33] and Feist et al. [34]. A big advantage of strong coupling is to make many quantum optical processes accessible at ambient conditions, such as coupling with a single quantum dot [35, 36], room temperature polariton lasing [37] and Bose-Einstein condensation in a plasmonic lattice [38].

Most research in the strong coupling regime has been conducted in microcavities. Only a handful of studies has been conducted with individual plasmonic nanoparticles [29, 39-48], despite the advantage of a nanoscale mode volume with strong electric field hot-spots. This PhD project aims to contribute to a better understanding of the strong coupling process between plasmonic and excitonic modes at ambient conditions. Furthermore, the goal is to discuss some of the advantages and limitations in the coupling process.

The thesis is structured as follows: In **Chapter 2**, the individual components, that are employed in the studies for this thesis, are introduced. Basic optical properties of metals are presented and discussed according to the Drude model. Subsequently, plasmonic modes and the resulting hot-spots are derived and the resulting effects on the optical properties, like the scattering cross-section, analyzed. Furthermore, atomically thin transition metal dichalcogenide (TMDC) layers are described with focus on the semi-conducting band gap and the excitonic modes. TMDC, such as Tungsten Diselenide (WSe_2), is in bulk form an indirect band gap semi-conductor. However, thinned down to a single monolayer it experiences a transition to a direct band gap semi-conductor. In the mono- and few-layers limit this results in many interesting properties such as bound exciton-hole pairs, so-called excitons, as well as strong absorption in the visible and near-infrared spectrum. The confinement in atomically thin layers of WSe_2 leads to high binding energies, making these excitons stable at ambient conditions.

Chapter 3 constitutes the main part for this thesis and focuses on the strong coupling process of two individual modes. Different theoretical models are presented, analyzed and compared with respect to the resulting elastic scattering and luminescence processes of the coupled system. The consequence of plasmon-exciton detuning and different coupling strengths on the polariton formation as well as the property of anti-crossing is demonstrated and discussed. Furthermore, various criteria for reaching the strong coupling regime are derived and analyzed.

Since this thesis is based on experimental studies of strong coupling, the various measurement methods are described in **Chapter 4**. In the beginning of this chapter, an overview of the different fabrication methods for the nanostructures is given. Subsequently, all methods for quantifying the shape and optical properties of these nanostructures are described and illustrated. At the end of this chapter a few methods and results outside the scope of the strong coupling studies are presented, like nonlinear laser microscopy and near-field optical methods. Moreover, some results on how these methods complement each other are highlighted.

In **Chapter 5**, some concluding remarks are given. In particular, the appended publications are summarized and briefly discussed. Finally, a short outlook to where this research field could go is explored.

Chapter 2: Optical Properties of Plasmonic Nanoparticles and TMDC

Strong coupling between an optical cavity and emitters in organic and inorganic molecules has been predicted and experimentally proven as early as 1992 [49]. When the optical modes of both cavity and emitter spatially and spectrally overlap, they can couple to each other. The coupling strength of this interaction, with perfect alignment of dipole and electric field, is defined as: $g = \mu_e \sqrt{N} |E_{vac}| \propto \mu_e \sqrt{\frac{N}{V_m}}$, with E_{vac} and V_m being the vacuum field and the mode volume of the optical resonator, μ_e the transition dipole moment between the ground and excited state of an emitter and N is the number of emitters participating in the coupling process. Hence, it is important to understand the optical properties of the individual components before studying the coupled system. This chapter will first introduce optical resonators and then, more specifically, plasmonic nanoparticles as open optical resonators. Thereafter follows a description of the TMDC and emitter that have been used in the studies for this thesis.

2.1 Optical resonators

Optical resonators, or optical cavities, can store and confine light at certain (resonance) frequencies. The simplest design of an optical resonator is a Fabry-Pérot cavity composed of two opposing mirrors, where the light is trapped between them, reflecting from one mirror to the other. Such a cavity is characterized by the effective mode volume and the quality factor [50]. The effective mode volume determines the confinement of light inside the cavity and follows as [51, 52]:

$$V_{eff} = \frac{\int \epsilon(r) |E(r)|^2 d^3r}{\max(\epsilon(r) |E(r)|^2)} \quad (2.1)$$

Where $\epsilon(r)$ is the dielectric function and $E(r)$ the electric field at position r . The quality factor determines the number of reflections or oscillations a trapped photon does, before it leaves the cavity. Thus, the quality factor determines how long light can be stored in the cavity and is defined as:

$$Q = 2\pi \frac{\text{energy stored}}{\text{energy loss per cycle}} \quad (2.2)$$

With the photon lifetime $\tau_0 = \frac{1}{\Gamma}$, where Γ describes loss as a spectral width and resonance frequency ω_0 the quality factor becomes:

$$Q = \frac{\omega_0}{\Gamma} \quad (2.3)$$

A different type of optical resonator is a distributed Bragg reflector (DBR), where the mirror is fabricated by dielectric materials with alternating refractive indices. In general, DBR mirrors have a higher quality factor and are less lossy, compared to metallic mirrors [53]. However, as mentioned previously, for a light-matter interaction the coupling strength depends on the mode volume of the resonator. For DBRs the mode volume exceeds that of metallic mirrors due to multiple reflections on the different dielectric layers of the mirror.

2.2 Plasmonic particles as open optical resonators

The previous section discussed optical resonators as light being trapped between two mirrors. A plasmonic nanoparticle can likewise trap light and act as an open optical cavity. Because of high radiative and non-radiative losses, the quality factor of this kind of open optical resonator ($Q \sim 10 - 100$) is much lower than of dielectric cavities ($Q \sim 10^6$). However, a conventional closed cavity has a diffraction limited mode volume ($V \sim \left(\frac{\lambda}{2}\right)^3$), with λ the wavelength of light in the dielectric medium [54]. One of the major advantages of plasmonic nanoparticles is, that light will be squeezed in a hotspot much smaller than the diffraction limit. This compensates for a lower quality factor with much stronger field intensities. Hence, plasmonic particles, as open optical cavities, can be used for strong coupling since the ratio of V_m/Q is comparable to macroscopic high Q resonators. The following sections discuss the optical properties of metallic nanoparticles. Starting with a general description of the dielectric function and concluding with scattering spectra for particles studied in this thesis.

2.2.1 Free electrons in a metal, a Drude model approximation

Metals have been employed since many centuries because of their outstanding optical and electronic properties. They are highly reflective in the visible spectrum and furthermore have a high conductivity. These properties made metals attractive, however only in the beginning of the 20th century the first models for the theory of solids arose. Drude postulates that when metallic atoms bind to form a solid, they keep a core set of electrons tightly bound to the nucleus, but the outer shell of valence electrons is shared with all other atoms in the solid. These free electrons are treated as a weakly interacting gas of conduction electrons [55-57]. The electrons move on straight lines and the only allowed interaction is collisions of these electrons with the (immobile) heavy atom cores with a characteristic collision time τ . The difference between metals, such as gold and silver, is the electron-density and collision time.

If an external electric field is applied, then the movement of the electrons can be described via Newtons equation of motion [58]:

$$m_e \frac{d^2 \mathbf{x}}{dt^2} + m_e \gamma \frac{d\mathbf{x}}{dt} = -e\mathbf{E} \quad (2.4)$$

Where $E = E_0 e^{-i\omega t}$ is assumed to be a harmonic driving field, $x(t) = x_0 e^{-i\omega t}$ the electron displacement, m_e and e are the mass and charge of an electron, respectively and $\gamma = \frac{1}{\tau}$ the damping via collision. In the frequency space and in the quasi-static limit the solution for (2.4) can be found as:

$$\mathbf{x}(\omega) = \frac{e}{m_e(\omega^2 + i\gamma\omega)} \mathbf{E}(\omega) \quad (2.5)$$

The induced dipole moment per oscillator is $\mathbf{p} = -e\mathbf{x}$. Then the sum over all dipole moments results in the total polarization:

$$\mathbf{P} = N\mathbf{p} \quad (2.6)$$

Where N denotes the number of oscillators per unit volume. From Maxwell equations, the dielectric displacement for a linear homogenous isotropic medium is defined as:

$$\mathbf{D} = \epsilon_0 \mathbf{E} + \mathbf{P} = \epsilon_0 \epsilon(\omega) \mathbf{E} \quad (2.7)$$

And thereby (2.7) will become:

$$\mathbf{D} = \epsilon_0 \left(1 - \frac{\omega_p^2}{\omega^2 + i\gamma\omega} \right) \mathbf{E} \quad (2.8)$$

Where $\omega_p^2 = \frac{Ne^2}{\epsilon_0 m_e}$ is the plasma frequency of the system. Hence, the dielectric function for a metal is written as follows:

$$\epsilon_{Drude}(\omega) = 1 - \frac{\omega_p^2}{\omega^2 + i\gamma\omega} \quad (2.9)$$

This is the Drude model of a free-electron metal. According to this model, metals are characterized by their respective plasma frequency (electron density) and damping via electron-ion collisions. Even though this is a simplified model, the Drude approximation can describe many metallic properties [59]. An expansion to account for interband-transitions can be done with the Drude-Lorentz model. In this work, the Drude model suffices, since all excitations are in the near-infrared regime, thus far away from the interband-transitions in gold which exist above 2 eV [60].

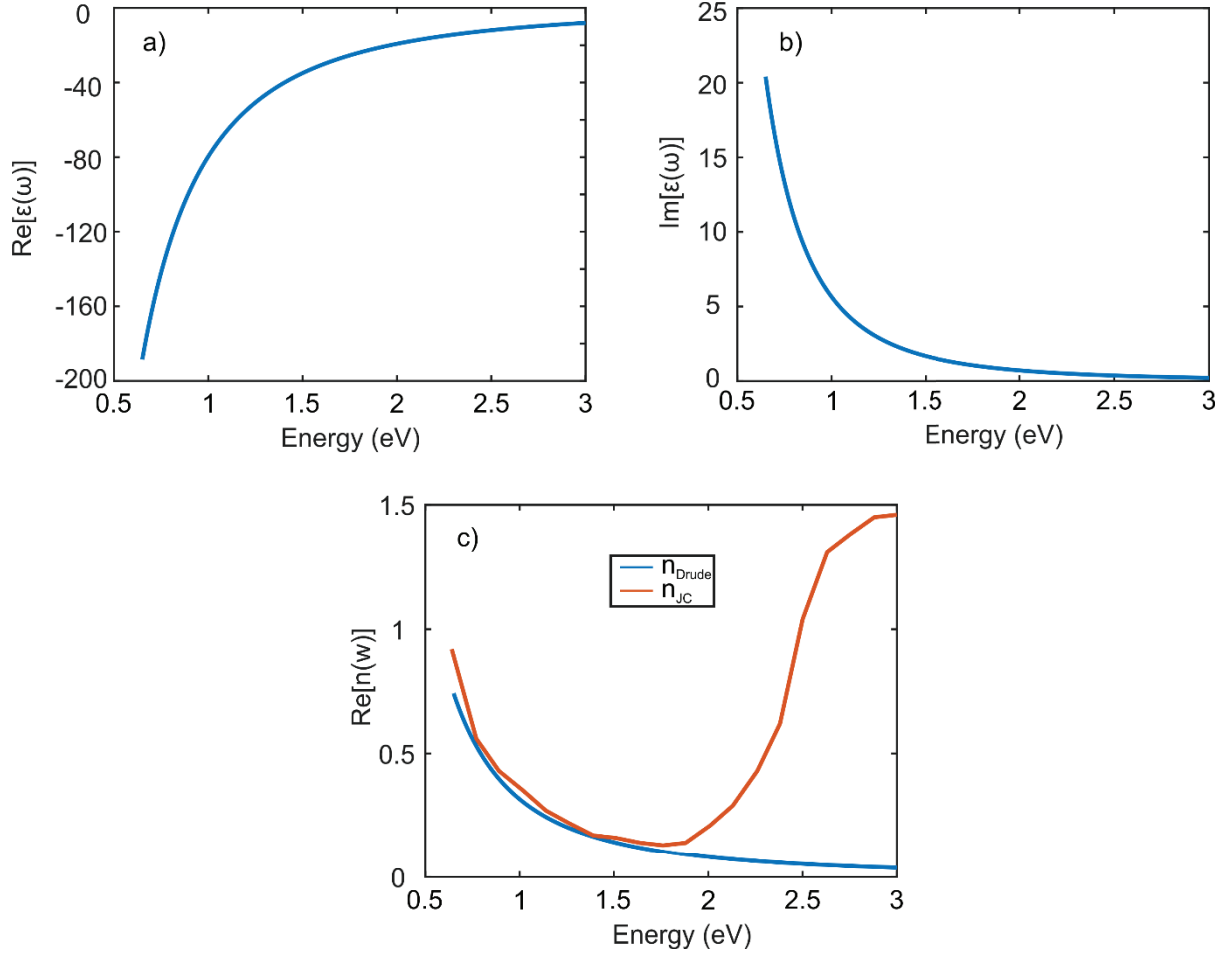


Figure 2.1. Drude dielectric function of a metal. Values are chosen to approach the real dielectric function for gold. (a) real part of ϵ , (b) imaginary part of ϵ and (c) the real part of the complex refractive index n_{Drude} as determined by the Drude model and plotted together with the real part of n_{JC} as determined by Johnson and Christy [61].

The real and imaginary part of the dielectric function (2.9) are plotted together with the real part of the complex refractive index in Figure 2.1. For the dielectric function values the plasma frequency and the collision time have been chosen to match gold as a metal. The complex refractive index is related via $n(\omega) = \sqrt{\epsilon(\omega)}$. Several things can be understood from these graphs. First, the real part of the dielectric function is negative over the whole visible spectrum since $n = \sqrt{\epsilon}$ this leads to a large imaginary part in the refractive index. This means that incoming light does not penetrate very deep in the metal [62]. Furthermore, when comparing the Drude dielectric function (blue line in Figure 2.1 (c)) to the refractive index of gold as determined by Johnson and Christy [61] (orange line), one can find that they agree well in the

visible region. Only when approaching the interband transitions around 2 eV, then the limitation of the simple Drude dielectric function becomes obvious and the model collapses.

2.2.2 Localized surface plasmon resonance

The Drude model describes a metal in bulk form, however things become very different when a metal particle becomes smaller than the wavelength of light. In such a case, the wavelength of light is long compared to the particle dimensions and the so-called quasi-static approximation is valid.

Assuming now a spherical metal nanoparticle, the complex polarizability α is defined via Clausius-Mossotti relation [57-59]:

$$\alpha = 4\pi a^3 \frac{\epsilon_{metal} - \epsilon_{medium}}{\epsilon_{metal} + 2\epsilon_{medium}} \quad (2.10)$$

With the radius a of the nanoparticle and ϵ_{medium} the dielectric function of the surrounding medium. From expression (2.10) it is obvious that the final optical properties, such as scattering and absorption, depend on the geometrical shape of the particle, the dielectric function of the metal as well as the dielectric function of the surrounding medium. The dielectric function of the metal has already been discussed in the previous section (2.2.1). The relation of the polarizability to the external medium shows that a high refractive index medium will reduce the polarizability and thus reduce the oscillation. This indicates that the metal nanoparticles optical properties change, depending on the surrounding medium, which is substantially exploited for sensing [6, 63-69]. The Clausius-Mossotti relation (2.10) is valid only for spheres, thus the dependence on the diameter of the particle leads to the definition for a geometric form-factor L_i in ellipsoidal coordinates [57] and (2.10) becomes:

$$\alpha_i(\omega) = 4\pi a_1 a_2 a_3 \frac{\epsilon(\omega) - \epsilon_{medium}}{3\epsilon_{medium} + 3L_i(\epsilon(\omega) - \epsilon_{medium})} \quad (2.11)$$

Where $a_{1,2,3}$ are the semi-axes of an ellipsoid and the geometrical form-factor:

$$L_i = \frac{a_1 a_2 a_3}{2} \int_0^\infty \frac{dq}{(a_i^2 + q) f(q)} \quad (2.12)$$

$$f(q) = \sqrt{(q + a_1^2)(q + a_2^2)(q + a_3^2)} \quad (2.13)$$

The form-factor L fulfills the condition $\sum L_i = 1$. For a spherical particle the form-factors become $L_1 = L_2 = L_3$ and from (2.11) one retrieves again (2.10). In the work done for this thesis the two most relevant shapes are: first, a bipyramid which can be described qualitatively as a prolate spheroid, see Figure 2.2 (a). And second, a flat nanodisk, more specifically the inverted structure, a nanohole in a thin gold film. For both structures two axes can be assumed to be equal $L_2 = L_3$. L_1 can be then written as a function of its eccentricity [57]. For the prolate spheroid with $a_2 = a_3$:

$$L_{1-prolate} = \frac{1 - e^2}{e^2} \left(-1 + \frac{1}{2e} \ln \frac{1 + e}{1 - e} \right) \quad (2.14)$$

and

$$e_{prolate}^2 = 1 - \frac{a_2^2}{a_1^2} \quad (2.15)$$

For the oblate spheroid with $a_1 = a_2$:

$$L_{1-oblate} = \frac{g(e)}{2e^2} \left[\frac{\pi}{2} - \tan^{-1} g(e) \right] - \frac{g^2(e)}{2} \quad (2.16)$$

$$g(e)_{oblate} = \left(\frac{1 - e^2}{e^2} \right)^{1/2} \quad (2.17)$$

$$e_{oblate}^2 = 1 - \frac{a_3^2}{a_1^2} \quad (2.18)$$

For a thin nanodisk $a_3 \ll a_2 = a_1$ and $e_{oblate} \rightarrow 1$ which leads to $L_{1-oblate} \rightarrow 0$ and $L_{2-oblate} = L_{3-oblate} = \frac{1}{2}$.

From (2.11) it is evident that the polarizability has a maximum along each axis when the real part of the denominator vanishes ($Re[\epsilon_{medium} + L_i(\epsilon_{Drude} - \epsilon_{medium})] \rightarrow 0$) and the imaginary part is only small or slowly varying. Knowing that $n = \sqrt{\epsilon}$ in mind, one derives the frequency ω_{pl} :

$$\omega_{pl} = \frac{\omega_p}{\sqrt{1 + n_{medium}^2 \left(1 + \frac{1}{L_i}\right)}} \quad (2.19)$$

Where ω_{pl} is the so-called *localized surface plasmon resonance* (LSPR). Thus, the plasmon resonance depends on the plasma frequency, the surrounding medium and geometrical form of the nanoparticle. At resonance frequency all surface electrons oscillate in a coherent manner. By displacing the free electrons coherently in the same direction away from the positively charged ions, a strong localized electric field is built up. The electrons oscillation is shown in Figure 2.2 (b). The charge gradient acts as restoring force. Note, this approximation is only valid when the particle is small compared of the wavelength of light. In order to consider effects such as dynamic depolarization, which plays an important role in bigger particles, one can correct the polarizability by the modified long wavelength approximation (MLWA) for a more accurate simulation [70].

Finally the scattering and absorption cross-sections can be calculated via the Poynting vector [57]:

$$\sigma_{sca} = \frac{k^4}{6\pi} |\alpha(\omega)|^2 \quad (2.20)$$

$$\sigma_{ext} = k \operatorname{Im}[\alpha] \quad (2.21)$$

With the wavevector $k = \frac{\omega n}{c}$ and n the refractive index of the surrounding medium. In Figure 2.2 (c) and (d) the scattering cross-sections of several prolate spheroidal nanoparticles are simulated. The chosen parameters simulate scattering in an energy region similar to the experimental data in the attached publications. From these plots one can immediately observe that on the one hand, with an increasing aspect ratio the plasmon resonance undergoes a constant redshift. On the other hand, increasing the particle volume increases the total scattering cross-section. The shift in the plasmon resonance is an important property of the plasmon resonance and will be used to recreate the dispersion relation in *Paper I* and *Paper III*.

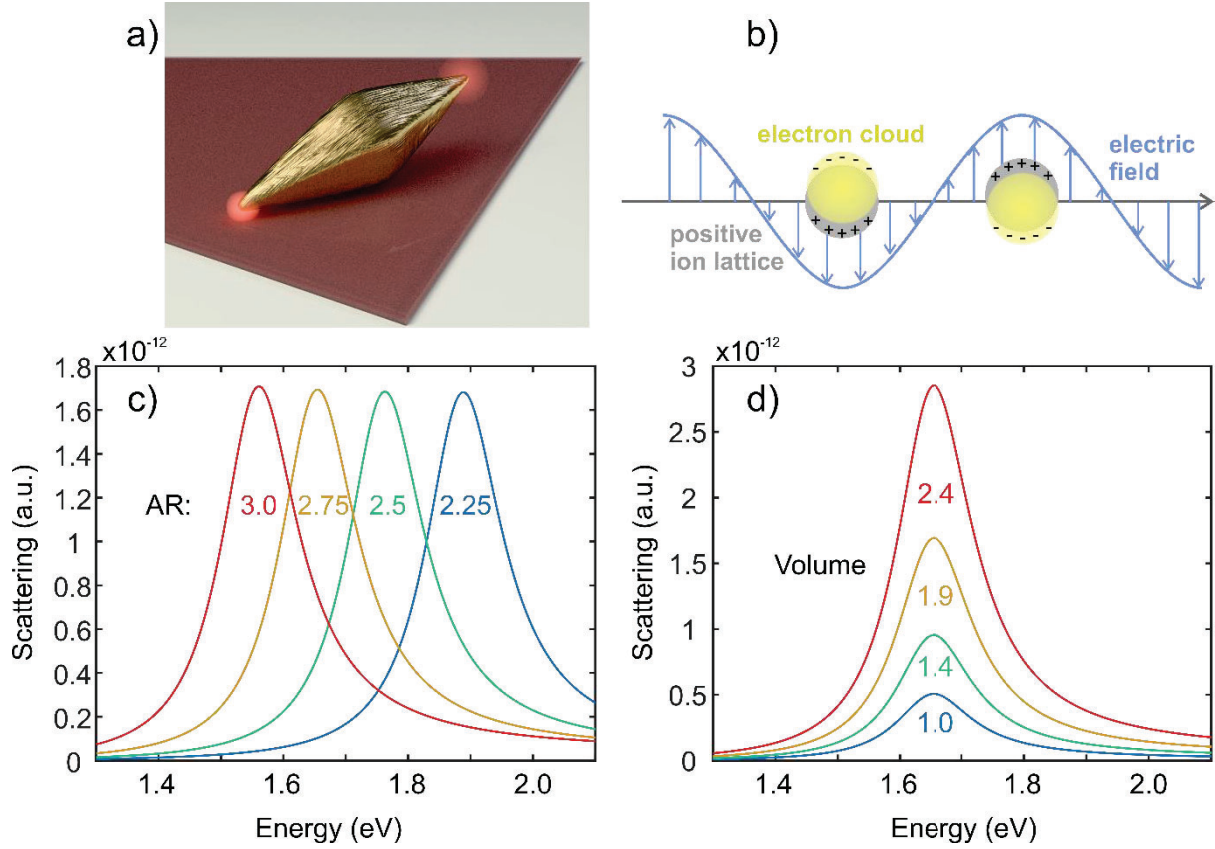


Figure 2.2. (a) Artistic image of a bipyramid gold nanoparticle with two hotspots. (b) Illustration of an LSPR. The electron cloud oscillates back and forth, displacing the negative electrons from the positive ion lattice. (c), (d) Simulated scattering of a prolate spheroid (bipyramid). Values have been chosen to imitate the same energy region as real experiments of such nanoparticles of the published results from this thesis. (c) Nanoparticles with increasing aspect ratio show an energy redshift of the plasmon resonance. (d) Nanoparticles with increasing volume scatter more effectively.

2.2.3 Surface plasmon polariton

The previous section described coherent electron oscillations in small metal nanoparticles, however, a similar coherent motion can take place at the metal-dielectric interface too. Though, this kind of light-matter excitation is not localized and can propagate over the surface. The dielectric function for metal has a negative real part over the whole visible spectrum, see Figure 2.1. This leads to surface bound interactions. An electromagnetic wave can excite surface charge density fluctuations which in turn lead to an electric field on the surface, as shown in Figure 2.3. The strong interaction of light and matter leads to a *surface plasmon polariton* (SPP). The SPP dispersion is defined as:

$$k_{SPP} = k_0 \sqrt{\frac{\epsilon_{metal}\epsilon_{medium}}{\epsilon_{medium} + \epsilon_{metal}}} \quad (2.22)$$

Where $k_0 = \frac{\omega}{c}$ is the wavevector of light in free space [71, 72]. The dispersion relation for a Drude-metal-air interface ($\epsilon_{medium} = 1$) is plotted in Figure 2.3. Immediately evident is that the SPP has a higher momentum vector than light in free space. At lower energies the wavevector of the SPP asymptotically approaches the wavevector of free space light. Furthermore, at higher energies the coupling of the electromagnetic light and the surface density oscillations becomes stronger, leading to the wavevector of the SPP bending further away from the free space light. Thereby light from free space could not excite such a surface bound wave. Nevertheless, there are several ways of exciting a SPP. In an optically thin metal film, the SPP can be excited not from the air but rather from the back side through a higher refractive index medium. In such a case the momentum is enough to excite a SPP at the metal-air interface. Furthermore, surface defects can always lead to a SPP excitation. An alternative method is to add the missing momentum by a grating on the surface with matching periodicity. With a grating of periodicity a_0 , the SPP momentum follows as:

$$k_{SPP} = k_x \pm nG_x \pm mG_y \quad (2.23)$$

With $k_x = \frac{\omega}{c} \sin \Theta$, the wavevector component of the incident photon in the plane of the grating, n, m are integers and $G_x = G_y = \frac{2\pi}{a_0}$ the grating momentum vector for a square array [73].

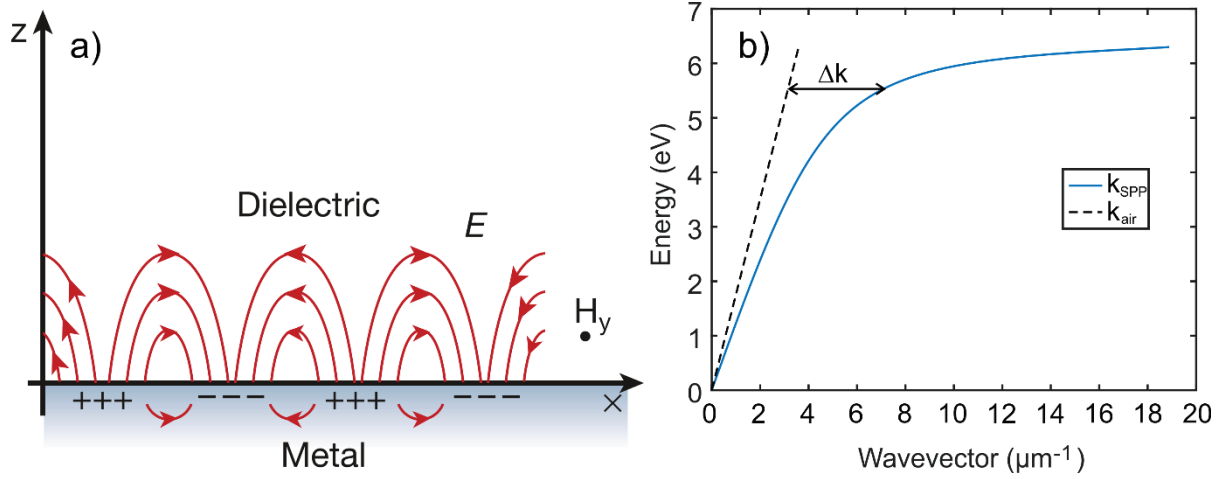


Figure 2.3. SPP formation at a dielectric-metal interface. (a) Sketch of the electromagnetic field distribution in the dielectric and the metal [71]. (b) SPP dispersion indicating that a light wave carries not enough momentum to excite a SPP.

2.2.3 Nanoholes in a thin metal film

Until now only LSPRs in a particle have been considered within this thesis. However, another very peculiar phenomenon appears at the inverse structure: Nanoholes in a metal film. When sub-wavelength holes are drilled in an optically thick metal film, then the transmitted spectrum is expected to follow [73, 74]:

$$t \sim \left(\frac{r}{\lambda}\right)^4 \quad (2.24)$$

Where r is the radius of the hole and λ the wavelength of the transmitted light. However, the actual spectrum features a so-called extraordinary transmission peak. At this peak wavelength, the amount of transmitted light can exceed values over one. The reason for this is that light forms SPPs on areas without holes, which travel on the metal surface and scatter at the edge of the nanohole.

When the metal film becomes optically thin to just few tens of nanometers thickness, then the electron cloud at the edge of the hole can oscillate in and out of the hole area, creating opposite charges across the hole, similar to a LSPR in a metal nanoparticle. This leads to high electric field intensities inside the hole and can furthermore be driven at a resonance frequency. Similar

to an LSPR of a metal nanoparticle, this effect depends on the shape and size of the nanohole as well as the refractive index of the surrounding medium [63, 68, 75]. Additionally, a very important aspect is the hole-hole interaction in a high density nanohole film. As mentioned in section (2.2.2) it is possible to achieve phase-matching for SPP excitation via a grating on the surface. This can be simply done by drilling holes in predefined distances, achieving a long-range order. However, as the manufacturing process is slow and expensive, a different approach is colloidal lithography, for more details see method section. Briefly, the result is a high density nanohole film with a specific short-range order. Excitation of a LSPR at a nanohole with an electromagnetic wave at plasmon resonance frequency is illustrated in Figure 2.4 (a). Furthermore, symmetric bonding SPPs can be excited at the holes as illustrated in Figure 2.6 (b). The anti-symmetric bonding mode would require higher energies and excitation in this configuration is not possible by normal incident light [75-77]. Depending on the nearest neighbor distance of the holes, resonant SPPs can be formed and significantly alter the extinction spectrum of the metal film. Optically thin high density nanohole films thereby offer a very interesting, albeit complicated extinction behavior containing both, LSPR and SPPs [78, 79]. Note, that with a polarization perpendicular to the plane of the metal film, the anti-bonding SPP mode could be excited. Though, this depends strongly on the film thickness and is less likely to contribute in the studies done in this thesis.

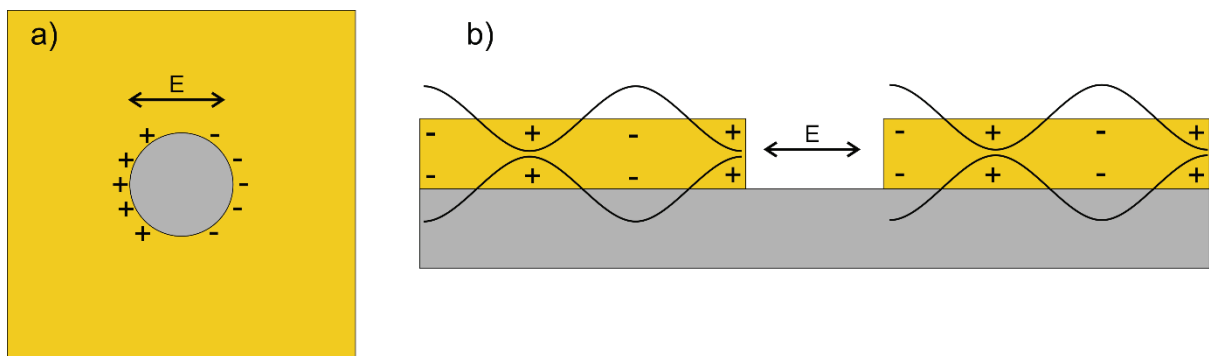


Figure 2.4. A thin gold film with nanoholes results in the combination of both, (a) LSPRs at the hole form via oscillating electron displacement along the edge of the hole and (b) SPPs in the metal film, which are mostly excited at the holes.

2.3 Transition metal dichalcogenides

The previous sections were focused on the properties of an optical cavity, which is one of the crucial components for the strong light-matter coupling. The following sections will describe the optical properties of the emitter, the second component in the coupling process. In this study the emitter consists of excitons in transition metal dichalcogenide (TMDC) thin films. A monolayer of TMDC has a height of less than a nanometer and is thereby regarded as a two-dimensional (2D) material. This results in many interesting properties, such as coupled electron-hole pairs, so-called excitons. Unusual high binding energies makes them stable even at room-temperature. TMDCs feature interesting optical properties, such as high absorption even in the single layer limit. High interest in creating TMDC few layer structures has resulted in many interesting applications such as UV absorbing contact lenses [80], ultrasensitive monolayer photodetectors [81, 82], LEDs [83, 84] and nanostructured solar cells [85]. Furthermore, excitons in such 2D materials are ideal components for strong light-matter coupling due to their high oscillator strength. The following two subsections will discuss the material properties from bulk to a single layer and the respective effects on excitons.

2.3.1 From bulk to monolayer

TMDCs can be formed by a variety of transition metal and chalcogenide atoms. The most common combinations are from the MX_2 group with Molybdenum or Tungsten as metal atoms (M) and Sulphur, Selenium and Tellurium as chalcogen atoms (X). Bulk and thin layers of TMDC have been investigated already for decades [86, 87]. Though, only with the rise of graphene many new preparation and analysis techniques became accessible and have been henceforth used to study 2D TMDC from few layers down to a single monolayer. One of the big milestones in preparation is micromechanical cleavage or ‘scotch-tape’ method. By applying scotch tape to a bulk crystal of TMDC, only a few or a single layer are removed and can be transferred to a new substrate for further use, more details can be found in the method section (4.1.1). The results are high quality, low defect crystalline flakes of usually several tens of micrometers in size. In the studies done in this thesis, mainly tungsten diselenide (WSe_2) has been employed and thus the focus is set on this TMDC. The most common and energetically stable stacking order for a WSe_2 crystal is 2H. Each tungsten atom is sandwiched

in an atomic trilayer structure between two selenium atoms in a side view of the $Se - W - Se$ structure and forms a hexagonal structure in a top-down view [88], see Figure 2.5 (a). Additional TMDC layers are stacked with a 180-degree in-plane rotation. The stacking order for WSe_2 multilayers is indicated in Figure 2.5 (b). The transition metal and chalcogenide atoms spatially alternate the positions with each layer due to the 180-degree rotation. The stacking of the different layers determines the electronic band structure of the material. This enables a new path for creating interesting material properties in hetero structures. By stacking TMDCs with a different lattice constant and adjusting the angle of rotation, so-called moiré-patterns are formed. These super-lattices can, for example, generate new resonantly hybridized inter- and intralayer excitons [89-94].

In the monolayer limit WSe_2 features a direct band gap at the K -valley point in the Brillouin zone. Via density functional theory (DFT) the band structure can be calculated, as seen in Figure 2.5 (e). Strong spin-orbit coupling (SOC) leads to the splitting of the valence-band, marked as v_1 and v_2 . The transitions at the K -valley point between the lowest point of the conduction band and v_1 are A-type excitons while transitions with v_2 and the conduction band are B-type excitons. From the reflection spectrum of a monolayer WSe_2 placed on a Si/SiO_2 substrate, the energy position of the A-excitons can be extracted with $E_A = 1.67 \text{ eV}$ and B-excitons $E_B = 2.08 \text{ eV}$ at ambient conditions (see Figure 2.5 (d)). The Energy difference is the SOC and leads to $\Delta E = E_B - E_A \sim 400 \text{ meV}$. This value agrees well with literature [95-101].

Stacking several layers of WSe_2 changes the band structure significantly. While the monolayer is a semi-conductor with a direct band gap at the K -point, already a bilayer features only an indirect band gap [97, 98, 100]. Adding more layers lowers the energy bands in the momentum space at different points than K . The indirect band gap modifies the radiative and non-radiative relaxation channels, which leads to a strong reduction of photoluminescence (PL) with an increasing number of layers. This is demonstrated in Figure 2.5 (c): From the monolayer a sharp single emission peak is visible around $E_{ex} = 1.67 \text{ eV}$. The value is very close to the absorption peak, which indicates only a small Stokes-shift. For a bilayer the PL intensity is reduced by over an order of magnitude. This is a clear evidence for the change to the indirect band gap. Interestingly the shape of the PL spectrum features two distinct peaks. One peak is situated close to the emission peak from the monolayer A-exciton and thereby is emission from the K -point in the Brillouin zone, despite this no longer being the lowest energy point in the conduction band. A second peak at lower energy $E_{I-B} = 1.56 \text{ eV}$ is emission from the indirect

band gap. This is supported by the fact that the peak ratio between the two peaks is changing for a higher number of layers toward the indirect band gap. This has been experimentally determined and confirmed via band structure calculations by Zeng *et al.* [100].

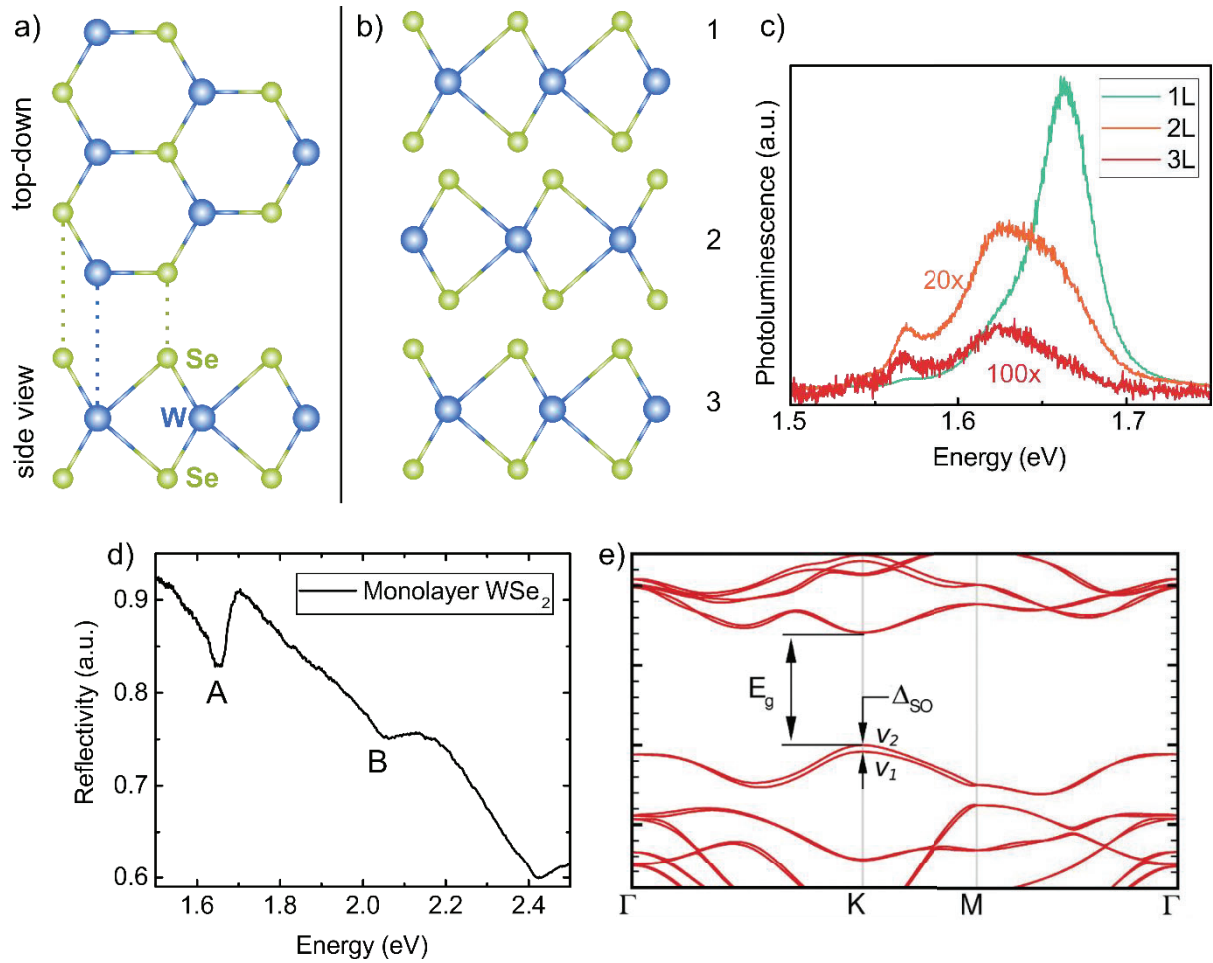


Figure 2.5. (a) 2H crystal structure of WSe₂ in top-down and side view of a monolayer. (b) Stacking of several layers of WSe₂ with weak van der Waals force between the layers. (c) Corresponding photoluminescence spectra from one up to three layers of WSe₂. (d) Reflection spectrum of a WSe₂ monolayer, marked are A and B exciton. (e) Typical band structure of a TMDC monolayer with the optical band gap energy E_g and spin-orbit coupling in the valence band [97].

2.3.2 Excitons in TMDC

Exciting an electron in a semi-conductor from the valence band in the conduction band, leaves consequently a hole in the valence band with the same wavevector k . Two opposite charges with the same group velocity, thus the same k -vector, can interact with each other and form a new energetically stable quasi-particle, an exciton [59]. The exciton is hold together via attractive Coulomb forces and carries a neutral charge. The energy of the exciton depends on the screening by other electrons and is thereby lower than the band gap of the semi-conductor. Depending on the screening strength, one often differentiates between two kinds of excitons. *Frenkel* excitons experience only a weak screening effect, which leads to strong Coulomb forces and strongly confined excitons. These tightly bound excitons are often observed in insulators and molecular crystals [102]. Frenkel excitons are localized in the atomic lattice and have a relative high binding energy, often making them stable at room temperature. The second kind of excitons is a so-called *Wannier-Mott* exciton. In semi-conductors with a high dielectric constant, the exciton is exposed to a strong screening effect, leading to a low attractive Coulomb interaction. The exciton radius takes up a larger space which exceeds the atomic lattice, making Wannier-Mott excitons delocalized and able to propagate through the crystal lattice. The low Coulomb force leads to a low binding energy of electron and hole, making these propagating excitons often only stable at cryogenic temperatures.

An exceptional case are TMDCs. Most TMDCs are, as described in the previous section, build of alternating tristructure-layers. This leads to weakly bound interlayer excitons and more importantly strongly bound intralayer excitons. In bulk form these intralayer excitons are exposed to screening from a full 3D environment, leading to a low binding energy. However, in the monolayer limit, the exciton is squeezed in a 2D environment. The electric field-lines between the opposite charges are only strongly screened inside the monolayer and begin to extend outside the semi-conductor, as evident in Figure 2.6 (a). This dielectric confinement results in potentially high binding energies of the exciton, making them delocalized as well as stable at ambient conditions.

The band structure depicted in Figure 2.5 (e) shows the optical band gap, whereby the quasi-particle band gap is necessary to determine the binding energy of the A-exciton [98]. The reduced electronic band structure for a typical TMDC is illustrated in Figure 2.6 (b). An electron can be excited from the valence band in the conduction band by an energy exceeding the quasi-particle band gap. Via inelastic phonon scattering the electron relax to the lowest

energy position of the conduction band. There the electron can interact with the opposing hole and form an exciton. The energy necessary to create an exciton is the energy required to create a free electron-hole pair, thus the quasiparticle band gap, minus the binding energy. Note, it is also possible to excite the exciton directly, since the exciton state is the energetically favorable state compared to free electron-hole pairs [102]. This leads to strong absorption lines at the exciton energy, as can be seen in Figure 2.5 (d).

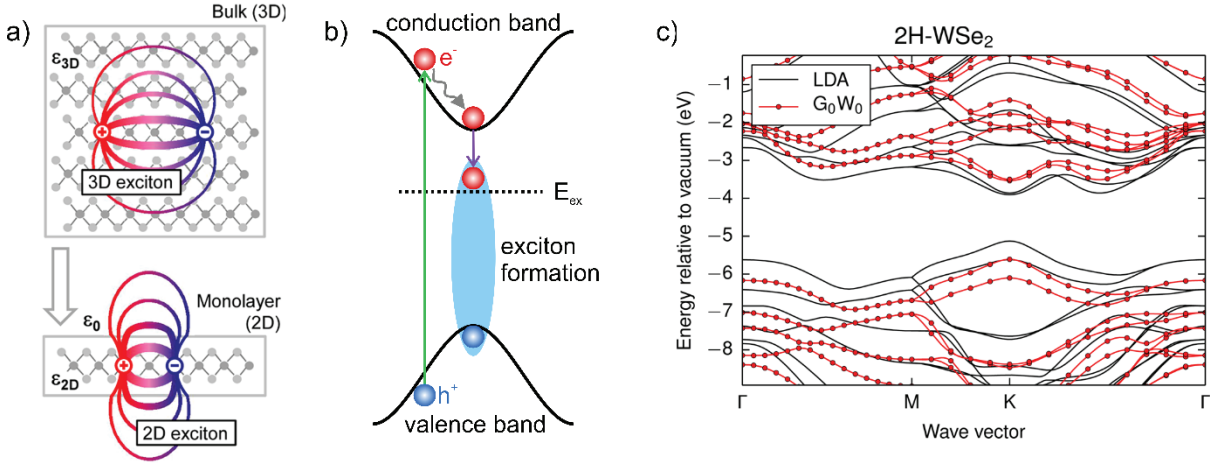


Figure 2.6. (a) Real space representation of the screening impact of a 3D vs 2D TMDC. $\epsilon_{2D,3D,0}$ are the dielectric constants for the monolayer and bulk TMDC as well as vacuum permittivity [103]. (b) Electronic band structure illustrating exciton formation with energy E_{ex} . Green arrow indicates an electron excitation and purple arrow indicates the exciton formation. (c) Band structure of a 2H-WSe₂ monolayer, calculated using low density approximation (black) and G₀W₀ (red) [98].

Rasmussen *et al.* [98] calculated for the band gap an energy of $E_{BG} = 2.08 \text{ eV}$ (Figure 2.6(c)) which corresponds well to measurements done by He *et al.* who determined $E_{BG} = 2.02 \text{ eV}$ [95]. The resulting binding energy for the A-exciton is then calculated as the difference between band gap energy and the exciton energy as determined e.g. from the absorption spectrum:

$$E_{A-binding} = E_{BG} - E_{A-exciton} \sim 0.37 \text{ eV} \quad (2.25)$$

As determined by He *et al.* [95]. For an exciton to be stable, the attractive forces have to protect it sufficiently against collisions with thermal phonons [102]. The thermal energy at room temperature is

$$U_{RT} = k_B T_{RT} = 25.5 \text{ meV} \quad (2.26)$$

with k_B the Boltzmann constant and $T_{RT} = 295 \text{ K}$ room temperature. The binding energy is about an order of magnitude higher than U_{RT} , making excitons stable even at ambient conditions [95, 97, 103-106].

Chapter 3: Light-Matter Interactions

Until now, all components, cavity and emitter, have been only considered individually, without any interaction between them. When the modes of a plasmonic nanoparticle and an emitter spatially and spectrally overlap, then the cavity photon can create a coherent polarization in the emitter medium and interact strongly with it. In an ideal case where all dipole moments are aligned with the cavity field, the strength of this interaction defines how the system is affected and follows as:

$$g = \mu_e \sqrt{N} |E_{vac}| \propto \mu_e \sqrt{\frac{N}{V_m}} \quad (3.1)$$

with E_{vac} and V_m being the vacuum field and the mode volume of the optical resonator, μ_e the transition dipole moment between the ground and excited state of an emitter and N is the number of emitters participating in the coupling process. In the weak coupling regime, the presence of the plasmonic particle can either enhance or quench the emission from the excitons (Purcell) [19]. With an increasing coupling strength, the system experiences a new interesting regime, so-called *strong coupling*. In this regime, the cavity and emitter exchange their energy back and forth coherently faster than their individual dissipation rates, leading to the formation of new hybrid modes. The first experiments on strong coupling and organic molecules has been demonstrated by Lidzey *et al.* in 1998 [107] and cavity exciton-polaritons have been observed by Weisbuch *et al.* as early as 1992 [49].

Various models, ranging from a purely classical description up to a fully quantum mechanical model, can be employed to describe the coupling between a cavity and emitter [108]. The classical harmonic oscillator model amply describes strong coupling and will be used to highlight some of the dependencies such as coupling strength, detuning and dissipation. The temporal coupled mode theory describes the system physically more accurate. A quantum mechanical approach includes the transition dipole moment and adequately incorporates vacuum Rabi splitting, the coupling case of when no photon is driving the system. In single-emitter coupling, a quantum mechanical description is necessary. However, the system studied in this work featured coupling to many emitters and thus, a simpler model is adequate.

3.1 Coherent and incoherent interactions

An important property of a process is its coherence. If optical waves, radiated from different emitters at different points \mathbf{r} , have a well-defined phase relationship, then the signal is coherent [109]. For the coherent case, the total field of all dipoles is non-vanishing $\langle E \rangle \neq 0$. A good example for such a coherent process is the LSP resonance as discussed in the previous chapters. The electrons experience a coherent motion and the displacement from the positive cores results in strong field gradients over the particle. On the contrary, if the phase between different emitters is random, then the total field will average to zero $\langle E \rangle = 0$. Note, that the intensity of an incoherent process is not zero even though the electric field of all emitter averages to zero. Coherence with respect to strong coupling is an important concept. The formation of polaritons, states of half-matter half-light, leads to the combination of different optical properties. For example, the excitons are incoherent emitters which all act independently. The plasmon resonance of the particles in this thesis work on the other hand is a coherent electron oscillation. Upon coupling strongly to each other, the new formed polaritons remain coherent properties albeit being part exciton and part plasmon.

As mentioned above, the coupling strength between an emitter and the cavity depends on the orientation Θ_i of the transition dipole moment μ to the electric vacuum field E_{vac} . This is quickly understood by realizing that the coupling strength is a scalar of both $g = \mu \cdot E_{vac}$. The resulting coupling strength of many emitters is then the sum over all individual interactions and represents an average coupling strength of the system.

$$g_{0i} = \vec{\mu}_{0i} \cdot \vec{E}_{vac} = |\vec{\mu}_{0i}| |\vec{E}_{vac}| \cos \Theta_i = g_0 \cos \Theta_i \quad (3.2)$$

And the total coupling strength, as a result of a coherent coupling over all emitters leads to:

$$g_{tot} = g_0 \sqrt{\sum_i^N \cos^2 \Theta_i} \quad (3.3)$$

Another interesting aspect of coherence is that the resulting light emission from coherent dipoles that are all in phase is much stronger, than from an incoherent source. This can be illustrated with expression (3.3), where it is obvious that the resulting coupling strength or emission intensity depend on the constructive phase alignment of each emitter. The property of coherence of an emitter can also be used or manipulated for phase-sensitive experiments, as shown in *Paper IV*.

3.2 Classical coupled harmonic oscillator model

As mentioned above, the classical harmonic oscillator model (COM) can be employed to describe a myriad of strong coupling features from a purely classical perspective [36, 110]. In this model the interaction of a resonant cavity with several emitters (excitons) ($N \geq 1$) is described by their respective equilibrium displacement coordinate $x_c(t)$ and $x_{0i}(t)$, $i = 1, 2, \dots, N$. The equations of motion for describing the system that is driven by the external force F follow as:

$$\begin{aligned}
 \frac{\partial^2 x_c}{\partial t^2} + \gamma_c \cdot \frac{\partial x_c}{\partial t} + \omega_c^2 x_c + \sum_k^N g_{0k} \frac{\partial x_k}{\partial t} &= F_c \\
 \frac{\partial^2 x_1}{\partial t^2} + \gamma_{01} \cdot \frac{\partial x_1}{\partial t} + \omega_{01}^2 x_1 - g_{01} \frac{\partial x_c}{\partial t} &= F_{01} \\
 &\vdots \\
 \frac{\partial^2 x_N}{\partial t^2} + \gamma_{0N} \cdot \frac{\partial x_N}{\partial t} + \omega_{0N}^2 x_N - g_{0N} \frac{\partial x_c}{\partial t} &= F_{0N}
 \end{aligned} \tag{3.4}$$

Where γ_c , γ_{0k} , ω_c and ω_{0k} are the corresponding dissipation rates and resonance frequencies, respectively. Note, that also a different approach to describe the system via COM exist, in which the coupling takes place via a linear displacement term rather than the first derivate, as employed in (3.4) [62]. Both describe the system qualitatively well, however, intuitively it is easier to understand that the coupling competes as a rate with other dissipation rates rather than a displacement. In the case of a plasmonic mode coupled to an excitonic mode, the plasmon interacts with an incident wave much stronger than the excitons, thus $F_c \gg F_{0N}$ and therefore $F_{0N} \rightarrow 0$ is set to zero.

The steady state amplitudes of the coupled system, driven by a harmonic wave, can be found by assuming harmonic time dependence of the plasmon and the excitons:

$$x(t) = x_0 e^{-i\omega t} \tag{3.5}$$

After Fourier transformation, the steady state expressions for the equilibrium coordinates become:

$$\tilde{x}_c(\omega) = \frac{\tilde{F}_c \prod_{j=1}^N (\omega_{0j}^2 - i\gamma_{0j}\omega - \omega^2)}{(\omega_c^2 - i\gamma_c\omega - \omega^2) \prod_{j=1}^N (\omega_{0j}^2 - i\gamma_{0j}\omega - \omega^2) - \omega^2 \sum_{j=1}^N g_{0j}^2 \prod_{k=1}^N (\omega_{0k}^2 - \omega^2 - i\gamma_{0k}\omega)^{(1-\delta_{jk})}}$$

$$\tilde{x}_k(\omega) = -\frac{i\omega g_{0k} \tilde{x}_c}{(\omega_{0k}^2 - i\gamma_{0k}\omega - \omega^2)} \quad (3.6)$$

$$\delta_{jk} = \begin{cases} 1, & j = k \\ 0, & j \neq k \end{cases}$$

The resulting coupling strength per emitter and of the total system is shown in expression (3.2) and (3.3), respectively. The coupling strength as determined by the coupled oscillator model is now referred to as g_{COM} . At resonance, the cavity drives the emitters, resulting in a coherent response from all coupled emitters. Scattering of excitons compared to plasmons is insignificant and can be neglected. The steady state expression for the equilibrium displacement corresponds to the polarization (electric dipole moment) of the plasmon mode introduced in Chapter (2.2.1) [110] and thus the scattering cross-section of the coupled system can be adequately described by:

$$\sigma_{sca}(\omega) \sim \omega^4 |\tilde{x}_c|^2 \quad (3.7)$$

Many features of the coupling process between a cavity and emitter can be explored by using this expression. Such a model, based on purely classical physics, sufficiently describes the scattering spectrum of a strongly coupled system, consisting of a BP and excitons in a monolayer WSe₂ as shown in Figure 3.1.

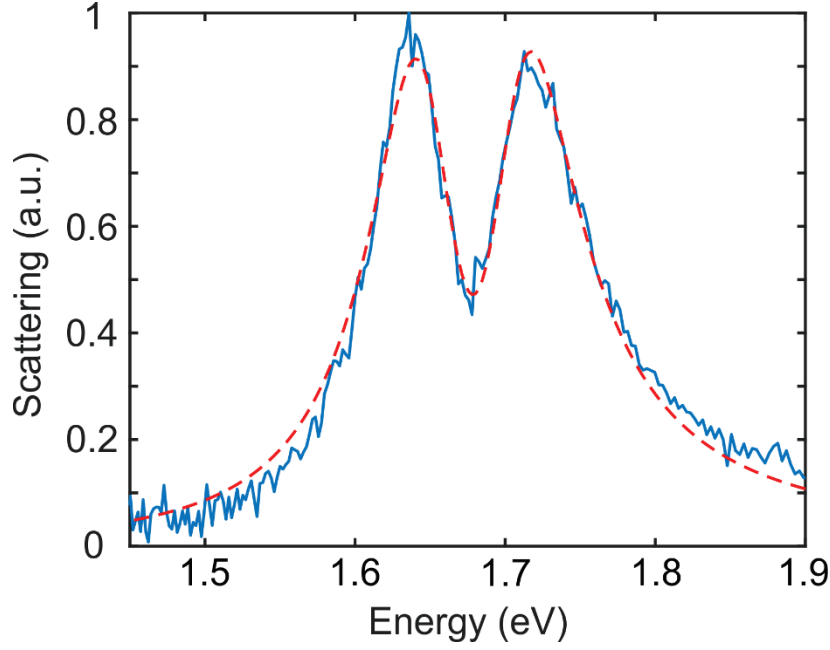


Figure 3.1. *Coupled oscillator model fit to a measured normalized dark-field scattering spectrum of a BP strongly coupled to excitons in WSe₂. The coupling strength is $g_{COM} = 65 \text{ meV}$.*

The scattering function is fitted with six different variables, which for the case of Figure 3.1 are: A scaling parameter $A = 4.9 \cdot 10^{-3}$, $\omega_c = 1.676 \text{ eV}$ and $\omega_{ex} = 1.679 \text{ eV}$ the resonance energy for the plasmonic cavity and excitons, $\gamma_c = 89 \text{ meV}$ and $\gamma_{ex} = 54 \text{ meV}$ the dissipation for the cavity and excitons and finally, the coupling strength $g_{COM} = 65 \text{ meV}$.

In each graph in Figure 3.2, a single parameter has been varied, while all other parameters are fixed. The default values were approximated to be similar to experimental values and around zero detuning: $\omega_c = \omega_{ex} = 1.67 \text{ eV}$, $\gamma_c = 100 \text{ meV}$, $\gamma_{ex} = 50 \text{ meV}$ and $g_{COM} = 75 \text{ meV}$. Since scattering scales with ω^4 the spectrum has an increasing tendency towards higher energy. As first and most interesting parameter for strong coupling, the coupling strength g_{COM} has been tuned from 0 to 125 meV. With no interaction at all ($g_{COM} = 0 \text{ meV}$) the scattering spectrum is a simple Lorentz peak, representing the scattering from the plasmonic particle. Note that, since the scattering of the exciton is much weaker than the scattering from the plasmonic particle its contribution has been neglected. Increasing the coupling strength transforms the single peak spectrum and splits slowly in two new modes. When they are weakly coupled, a small shoulder indicates a modification by the interference of the two systems

(yellow curve in Figure 3.2 (a)). With a higher coupling strength, a dip manifests and creates a certain transparency for the particle at the exciton resonance frequency (green curve). Finally, when the system enters the strong coupling regime the two modes are clearly distinguishable and shift further apart from each other (cyan, blue and purple curves). The lower energy peak is called lower polariton (LP) and the higher energy peak is called the upper polariton (UP).

Note that, the absolute value for the coupling strength depends on the treatment of the interaction and dissipation rates in the COM model. In order to compare the value with the coupling strength as derived by Törma and Barnes [108], g_{COM} needs to be divided by the factor 2, leading to $g = g_{COM}/2$. The total energy separation of these two modes is the *vacuum Rabi splitting* and follows as $\Omega = 2g = \omega_{UP} - \omega_{LP}$ (at zero detuning and neglecting dissipation). As mentioned previously, the strong coupling regime is reached when the cavity and emitter exchange coherently energy faster than their respective dissipation rates. A general rule of thumb for the strong coupling regime can then be defined as [108]:

$$\Omega \geq \frac{\gamma_c + \gamma_{ex}}{2} \quad (3.8)$$

With this formulation and the afore defined parameters in mind the transition from weak to strong coupling takes place when $\Omega \geq \frac{100 \text{ meV} + 50 \text{ meV}}{2} = 75 \text{ meV}$ (Figure 3.2. (a) cyan curve). In reality, the transition is not a sharp switch between the two coupling regimes, yet this definition serves as a general indicator in which coupling regime the system is.

When tuning the plasmon frequency from the red to the blue part of the spectrum, as indicated by the color code of Figure 3.2 (b), the visible weights of the two polaritons are shifting. The negative detuning of the two modes is $\delta = \omega_c - \omega_{ex} < 0$ and scattering at the LP frequency clearly dominates the spectrum (red curve). At zero detuning $\delta = 0$ (green curve) the two polaritonic weights balance each other and the energy difference gives the vacuum Rabi splitting Ω . With increasing plasmon energy the detuning becomes positive $\delta > 0$ and the scattering weights shift towards the UP (purple curve). From a set of red- to blue-detuned particles, the dispersion of the UP and LP branches and the anti-crossing can be reconstructed. Moreover, to avoid particle to particle variance the average coupling strength for a system of many particles can be determined. A more detailed explanation follows in Chapter 3.4.

Figure 3.2 (c) demonstrates the effect of the plasmon dissipation rate on the coupling process. Under the assumption that the coupling strength would remain constant, the biggest change in

the spectrum is the bandwidth of the UP and LP. The energy splitting experiences only a small increase while both peaks get broader with an increasing dissipation rate.

A similar observation can be done when analyzing the effect of the exciton linewidths, as shown in Figure 3.2 (d). With a small dissipation the dip in the spectrum is sharp and becomes less pronounced with an increased exciton dissipation. Furthermore, the splitting becomes slightly larger with an increased exciton bandwidth. It is evident that dissipation has a direct effect on the coupling strength.

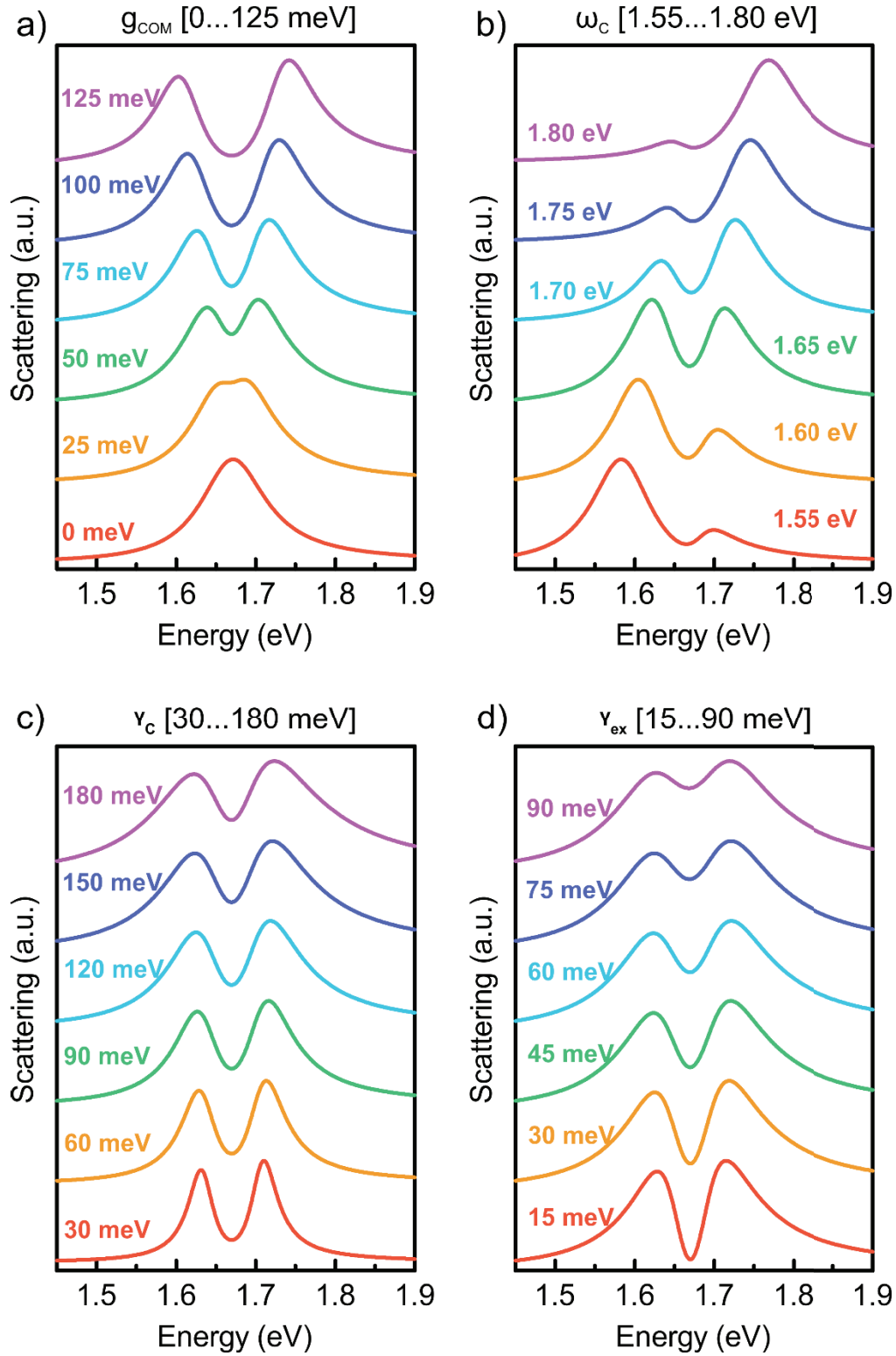


Figure 3.2. *Tuning of parameters in the coupled oscillator model. Only the parameter mentioned above each graph is varied, while the rest is fixed at a default value $g = 75$ meV, $\omega_c = 1.67$ eV, $\omega_{\text{ex}} = 1.67$ eV, $\gamma_c = 100$ meV and $\gamma_{\text{ex}} = 50$ meV. Tuning of (a) coupling strength g , (b) plasmon energy ω_c , (c) plasmon dissipation γ_c and (d) exciton dissipation γ_{ex} .*

3.3 Coupled mode theory

COM is adequate to demonstrate light-matter interaction in the strong and weak coupling regime. However, it is based on purely classical physics and treats both, plasmon and emitter as Lorentzian dipoles. A physically more accurate model is the temporal coupled mode theory (CMT) [111, 112]. In CMT the coupling between two modes is described by a Schrödinger-like equation:

$$i\hbar \frac{d|a\rangle}{dt} = \hat{H}|a\rangle + S_{inc}|\kappa\rangle \quad (3.9)$$

Where $|a\rangle = \begin{pmatrix} a_{pl} \\ a_0 \end{pmatrix}$ is the vector of the plasmon and exciton complex amplitudes. \hat{H} is the Hamiltonian of the coupled system, S_{inc} is a scalar amplitude of the incident light wave and

$|\kappa\rangle = \frac{1}{\sqrt{2}} \begin{pmatrix} \sqrt{\gamma_{pl}^{rad}} \\ \sqrt{\gamma_0^{rad}} \end{pmatrix}$ the ket-vector of radiative coupling rates. In this case the focus is on the

scattering of the system. Thereby the radiative loss from the excitons can be neglected $\gamma_0^{rad} \rightarrow 0$.

The optical Hamiltonian can be derived from the cavity quantum electrodynamics framework (cQED) [113, 114]. cQED describes the interaction of a quantized electromagnetic cavity with a single two-level atom. The atom itself has only sharp lines and for emitters such as excitons, dissipation needs to be included. It is not straight forward to introduce dissipation in a quantum mechanical system. Still an effective way to account for losses is to extend the frequency by $\omega_x = \omega_x - i\gamma_x$, where x can be the plasmon or exciton. This assumption works rather well with observables from coupled systems, such as the ones studied in this thesis [115]. The now non-Hermitian Hamiltonian reads:

$$\hat{H} = \underbrace{\hbar \begin{pmatrix} \omega_{pl} & 0 \\ 0 & \omega_0 \end{pmatrix}}_{\text{resonance energies}} - \underbrace{\frac{i\hbar}{2} \begin{pmatrix} \gamma_{pl} & 0 \\ 0 & \gamma_0 \end{pmatrix}}_{\text{dissipation}} + \underbrace{\hbar \begin{pmatrix} 0 & g \\ g & 0 \end{pmatrix}}_{\text{coupling}} \quad (3.10)$$

The first term contains the resonance energies of the plasmonic resonator (ω_{pl}) and excitons (ω_0). The middle term represents the respective dissipation or decoherence rates for cavity (γ_{pl}) and excitons (γ_0). And finally, the last term describes the coupling between the two modes

with the coupling strength g . The incident light wave is assumed to be harmonic and thereby $s_{inc}(t) = s_{inc}e^{-i\omega t}$ and $|a(t)\rangle \propto e^{-i\omega t}$. Similar to COM, the steady state solutions are:

$$a_0 = -\frac{ga_{pl}}{\omega_0 - \frac{i}{2}\gamma_0 - \omega} \quad (3.11)$$

$$a_{pl} = -\frac{s_{inc}\sqrt{\frac{\gamma_{pl}}{2}}}{\omega_{pl} - i\frac{\gamma_{pl}}{2} - \omega - \frac{g^2}{\omega_0 - i\frac{\gamma_0}{2} - \omega}} \quad (3.12)$$

Finally, the amplitude of the output signal is given by $s_{out} = \langle a|\kappa\rangle$. From this the scattering cross-section can be derived as:

$$\sigma_{scat} \propto |s_{out}|^2 = \left| \sqrt{\frac{\gamma_{pl}}{2}} a_{pl} \right|^2 = \left| \frac{\gamma_{pl}}{2\omega_{pl} - i\gamma_{pl} - 2\omega - \frac{4g^2}{2\omega_0 - i\gamma_0 - 2\omega}} \right|^2 \quad (3.13)$$

Comparing the scattering cross-sections obtained by the coupled oscillator model (3.6) and the coupled mode theory (3.13) reveals several differences in these models. The steady state solutions in COM are based on the second time derivative while in CMT they are based on the first derivative only. This manifests in the different power dependence on the participating frequencies. In COM the model scales as $\sim \frac{1}{(\omega_x^2 - \omega^2 - i\omega\gamma)}$ while in CMT the model follows $\sim \frac{1}{(\omega_x - \omega - i\gamma)}$, where x denotes plasmon or exciton. The consequence is that the derivation of the two models increases with the coupling strength. For the hybrid system, studied in this thesis, the derivation between the two models is rather insignificant. To demonstrate this the same particle scattering spectrum as for the COM has been used, as shown in Figure 3.3. The fits show qualitatively nearly no difference. However, when comparing the extracted coupling strength, then the difference seems substantial with $g_{COM} = 65 \text{ meV}$ and $g_{CMT} = 32 \text{ meV}$. Note, that this originates from a different treatment of the interaction and dissipation rates in the COM model. To better compare both models one should assume for the coupling strength in the COM: $g = \frac{g_{COM}}{2}$ [116].

Note, that the Rabi splitting scales as $\Omega \sim 2g$ and in case of the spectrum in Figure (3.3.) the peak to peak separation reaches $\Omega = 70 \text{ meV}$. With this in mind, one can find that in this energy region, both models can be applied to describe the light-matter interaction.

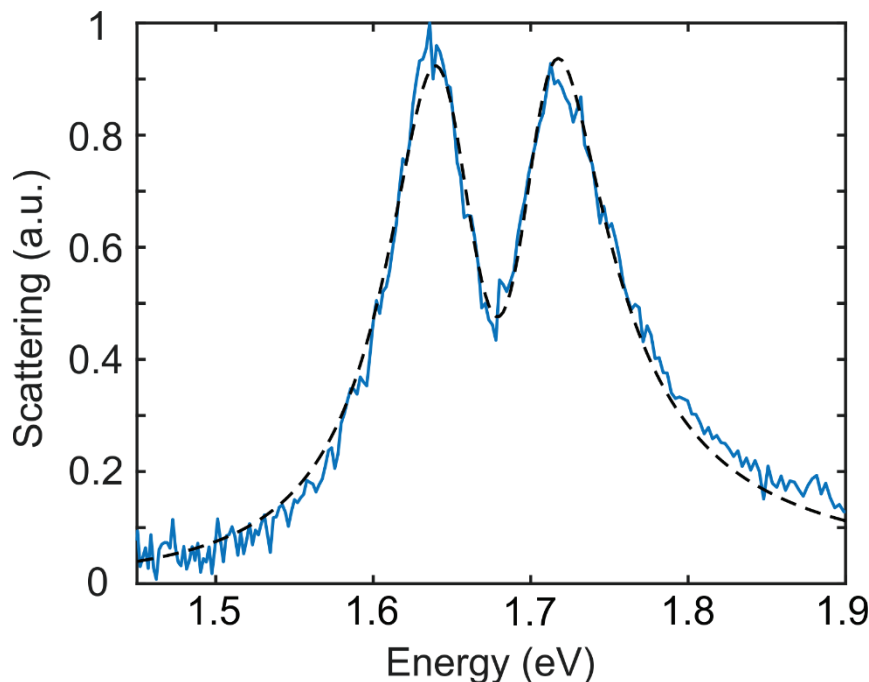


Figure 3.3. Scattering from coupled mode theory fit to a measured DF spectrum of a BP strongly coupled to excitons in WSe_2 . The coupling strength is $g_{\text{CMT}} = 32 \text{ meV}$.

3.4 Anti-crossing characteristics

One of the most prominent properties in strong coupling is the anti-crossing of the polaritonic modes [117]. This means, independent of the detuning, the new hybrid modes will never coincide. For a coupled system consisting of a plasmonic particle (bipyramid) and excitons in a 2D-material (WSe_2), the resulting coupling depends on many different parameters which are different from particle to particle, such as exact plasmon resonance, orientation of BP to the hexagonal lattice of the TMDC and more. To get a statistical invariant value for the coupling strength, a broad range of different detuned cavity-emitter systems is needed to reconstruct the dispersion relation.

We employ again the Hamiltonian that describes the coupling between plasmonic resonator and excitons in the same form as (3.10):

$$\hat{H} = \hbar \begin{pmatrix} \omega_{pl} - i\frac{\gamma_{pl}}{2} & g \\ g & \omega_0 - i\frac{\gamma_0}{2} \end{pmatrix} \quad (3.14)$$

The final polariton frequencies of the coupled system can be acquired by diagonalizing and determining the eigenvalues:

$$\hbar \begin{pmatrix} \omega_{pl} - i\frac{\gamma_{pl}}{2} & g \\ g & \omega_0 - i\frac{\gamma_0}{2} \end{pmatrix} \begin{pmatrix} \alpha \\ \beta \end{pmatrix}_{\pm} = \omega_{\pm} \begin{pmatrix} \alpha \\ \beta \end{pmatrix}_{\pm} \quad (3.15)$$

α and β are the Hopfield coefficients and represent a linear combination of the fractions of plasmon and excitons, fulfilling $|\alpha|^2 + |\beta|^2 = 1$. The eigenvalues are then obtained by solving the following equation:

$$\left(\omega_{pl} - i\frac{\gamma_{pl}}{2} - \omega_{\pm} \right) \left(\omega_0 - i\frac{\gamma_0}{2} - \omega_{\pm} \right) = g^2 \quad (3.16)$$

Where the two solutions for ω_{\pm} are:

$$\omega_{\pm} = \frac{\omega_{pl} + \omega_0}{2} - \frac{i(\gamma_{pl} + \gamma_0)}{2} \pm \sqrt{g^2 + \frac{1}{4} \left(\omega_{pl} - \omega_0 - \frac{i(\gamma_{pl} - \gamma_0)}{2} \right)^2} \quad (3.17)$$

Here \pm denotes the upper and lower polariton, respectively. Numerically this can be solved by determining the real part of the equation which corresponds the real-space frequency of the UP and LP. Analytically, the following assumption can be made: Since the resonance energy is much larger than the dissipation of the individual components, their dissipation can be neglected and (3.17) becomes:

$$\omega_{\pm} = \frac{\omega_{pl} + \omega_0}{2} \pm \sqrt{g^2 + \frac{\delta^2}{4}} \quad (3.18)$$

where $\delta = \omega_{pl} - \omega_0$ is the plasmon-exciton detuning. From this equation it is immediately clear, if no coupling takes place ($g = 0 \text{ meV}$) then the eigenvalues return simply the respective resonance energies.

As discussed earlier the vacuum Rabi splitting is determined as the separation of the LP and UP at zero-detuning $\omega_{pl} = \omega_0$, thus $\delta = \omega_{pl} - \omega_0 = 0$. With (3.17) the Rabi splitting becomes:

$$\Omega = \omega_+ - \omega_- = 2 \sqrt{g^2 - \frac{(\gamma_{pl} - \gamma_0)^2}{16}} \quad (3.19)$$

When neglecting losses, the resulting Rabi splitting becomes $\Omega = 2g$.

Moreover, from (3.19) it is evident that splitting will only occur when the term in the square root is kept positive and thereby a minimum coupling criterium can be defined as:

$$g > \frac{1}{4} |\gamma_{pl} - \gamma_0| \quad (3.20)$$

Though, (3.20) needs to be treated carefully. The limitation of this criterium becomes obvious when the respective losses (γ_{pl}, γ_0) are very large and approximately the same ($\gamma_{pl} \approx \gamma_0$), then even a small coupling strength value would be sufficient to get a positive value under the square root in (3.19). In practice however, in such a case the splitting would not be evident in any spectra. Therefore, as rule of thumb, a more intuitive criterium is the following relation: the splitting needs to overcome the dissipation rates [108].

$$\Omega \geq \frac{1}{2} (\gamma_{pl} + \gamma_0) \quad (3.21)$$

In this case the system completes at least one Rabi cycle, transferring the energy between plasmonic particle and emitter. Rajendran et al. determined experimentally a Rabi oscillation between J-aggregate excitons and a microcavity with a time period of $\sim 30 \text{ fs}$ [118].

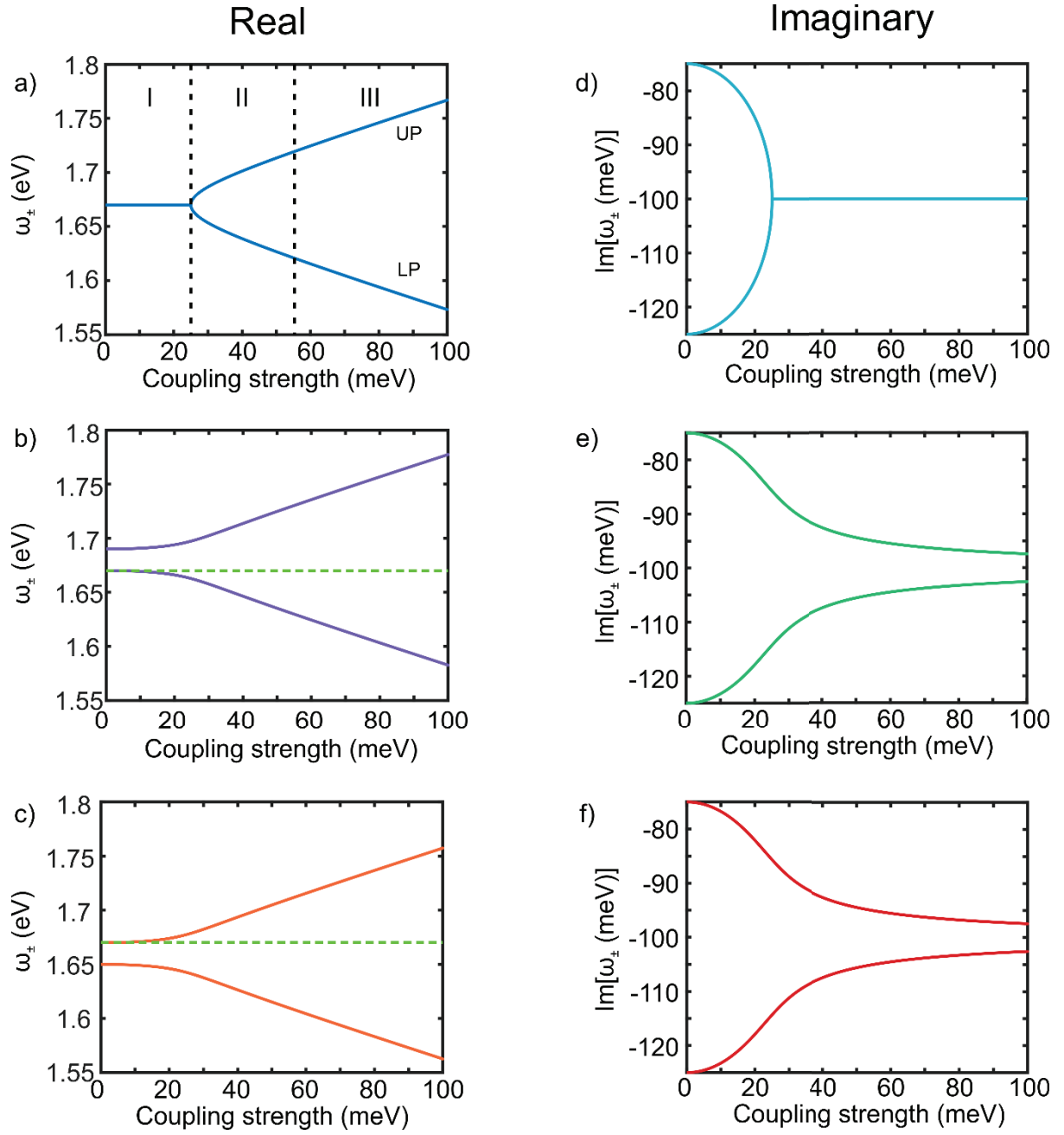


Figure 3.4. (a)-(c) Upper and lower polaritons in weak and strong coupling at (a) zero detuning, (b) positive detuning and (c) negative detuning. (d)-(f) Imaginary part of the eigenstate solutions at (d) zero detuning, (e) positive and (f) negative detuning.

The two new eigenstates ω_{\pm} as determined by (3.17) for a range of coupling strengths from the weak to the strong coupling regime as well as different plasmon-exciton detuning are plotted in Figure 3.4. Three different coupling regimes at zero detuning $\delta = \omega_{pl} - \omega_0 = 0$ are indicated in Figure 3.4 (a). In the first region (I) no splitting can be seen since the term in the square root is negative and only the real part of (3.17) represents the visible resonances. Since in this case the coupling strength is so low that nearly no interaction between plasmon and exciton happens and both individual resonances are visible.

Directly between (I) and (II) is the exceptional point, at which not only the two eigenvalues, but also the corresponding eigenvectors coalesce, rendering the Hamiltonian defective [119]. Above this coupling strength the square root term becomes positive and the new eigenstates are split. However, fulfilling the minimum criterium for splitting (3.20) does not define the strong coupling regime. Only when the third part of the diagram (III) is reached, then (3.21) is fulfilled and at least one Rabi oscillation between plasmon and exciton takes place, which is the definition of a strongly coupled system. Only in such a case the energy exchange between light and matter overcomes the individual dissipation rates. Most coupled systems with plasmonic nanoparticles are at the edge between (II) and (III) [41-43, 120], thus at the edge of a well-defined strong coupling. Graphs (b) and (c) demonstrate the effect of different detuning on the polariton splitting. Even without any coupling, the solution for (3.17) has two eigenvalues at the corresponding plasmon and exciton resonances. This outcome is surprising and careful interpretation is necessary.

Analyzing the imaginary part of expression (3.17) allows for a deeper look at the details of the coupling process. Before the system enters the strong coupling regime, expression (3.17) has two solutions that approach each other, as shown in Figure 3.4 (d). As soon as the term under the square root becomes positive both rates become degenerate and only one solution remains. This can be understood the following way: Before reaching the exceptional point both interacting modes can be still treated as individual entities while merely modifying each other. Whereas when the strong coupling regime is reached, new polaritonic hybrid states are formed with new inseparable dissipative processes. Interestingly, when plasmon and exciton are detuned, the two imaginary solutions of (3.17) do not become degenerate. Note further, that there is no difference in the rate values between positive or negative detuning. From the perspective of optical modes, the UP and LP have the same dissipative nature. However, as

will be discussed in section (3.6), this model is not sufficient to explain asymmetric photoluminescence emission between UP and LP.

An anti-crossing diagram is plotted in Figure 3.5 and demonstrates the effect of UP and LP dispersion for different coupling strengths. The dashed lines indicate the plasmon (green) and exciton (blue) resonance energies. For the case of no coupling between them, the two resonances cross each other without any interference. As soon as the coupling between the two modes overcomes the criteria in (3.20) the expected anti-crossing of two new UP and LP modes appears (orange lines). With an increasing coupling-strength the splitting becomes larger and the bending of the curves less pronounced. Furthermore, when the plasmon and exciton modes are strongly detuned, then both polaritons asymptotically approach the case of uncoupled plasmon and exciton resonance energies. This becomes further evident when analyzing the composition of the UP and LP as determined by the Hopfield coefficients. At a negative detuning the LP has a much higher plasmonic fraction and slowly approaches the case of an uncoupled system. Around zero-detuning the weights are equally distributed and the opposite appears at a positive detuning. The opposite is for the composition of the UP. Note, that even though with a small coupling strength the criterium of (3.20) is fulfilled and anti-crossing of the two eigenmodes in a scattering spectrum is evident, the system is not necessary in the strong coupling regime, as it could be a result of electromagnetic induced transparency [117, 121]. Nevertheless, when the anti-crossing of the two hybrid modes becomes evident in scattering and absorption then the system certainly is in the strong coupling regime. Note, the dispersion in a closed cavity depends on the cavity thickness and thus can be tuned by probing different angles inside the cavity. In an open cavity system, such as the BPs in these studies, there is no dispersion on an individual particle, but by analyzing many particles with slightly different plasmon resonance, the plasmon-exciton dispersion can be recreated.

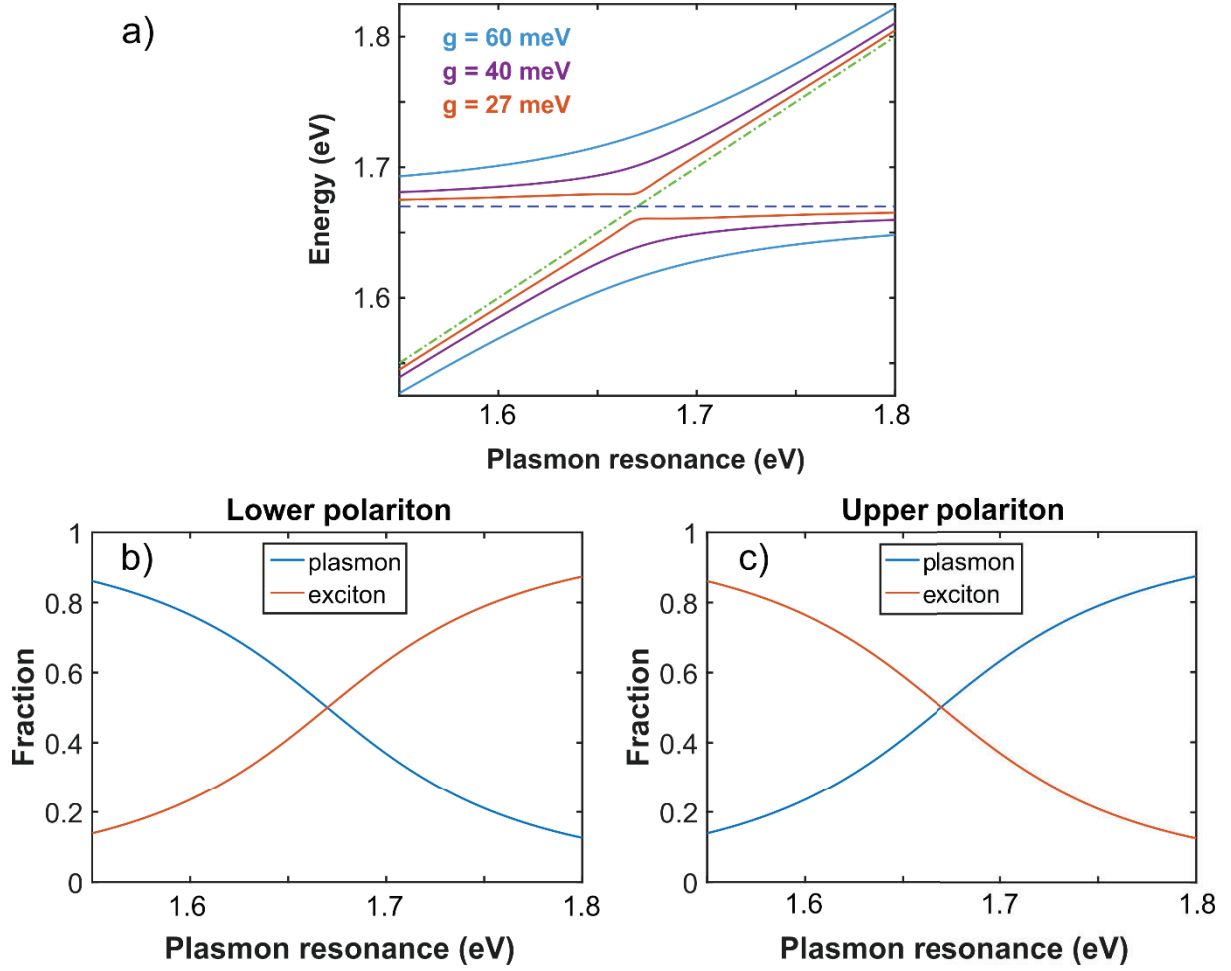


Figure 3.5. Anti-crossing curves of UP and LP at different coupling strengths. (a) Blue dashed line and green dashed line represent the exciton and plasmon energy without coupling, respectively. Solid lines are the UP and LP at different coupling strengths g . The exciton resonance is fixed at $\omega_0 = 1.67$ eV with $\gamma_0 = 50$ meV and the plasmon linewidth $\gamma_{pl} = 150$ meV. Plasmonic and excitonic compositions of the (b) LP and (c) UP.

3.5 A notion of quantum

In this thesis strong coupling is treated (semi-) classical, since the number of coupled emitters is assumed to be large and quantization effects play only a minor role. However, it is important to mention a few results from the quantum mechanical approach. For the general case of a single two-level emitter interacting with a quantized field of an optical cavity the so-called Jaynes-Cummings Hamiltonian is:

$$H_n = \hbar \left(n + \frac{1}{2} \right) \omega \begin{pmatrix} 1 & 0 \\ 0 & 1 \end{pmatrix} + \frac{\hbar}{2} \begin{pmatrix} -\delta & 2g\sqrt{n+1} \\ 2g\sqrt{n+1} & \delta \end{pmatrix} \quad (3.22)$$

$$\delta = \omega - \omega_0 \quad (3.23)$$

Where n is the photon number, ω_0 the resonance energy of the emitter and g the coupling strength. Diagonalizing the Hamiltonian in (3.22) leads to the two eigenvalues of the coupled system:

$$E_{1n} = \hbar \left(n + \frac{1}{2} \right) \omega - \frac{1}{2} \hbar \sqrt{\delta^2 + 4g^2(n+1)} \quad (3.24)$$

$$E_{2n} = \hbar \left(n + \frac{1}{2} \right) \omega + \frac{1}{2} \hbar \sqrt{\delta^2 + 4g^2(n+1)} \quad (3.25)$$

The Rabi splitting becomes then:

$$\Omega_n = E_{2n} - E_{1n} = \sqrt{\delta^2 + 4g^2(n+1)} \quad (3.26)$$

At zero detuning $\delta = 0$ expression (3.26) becomes:

$$\Omega_n = 2g\sqrt{n+1} \quad (3.27)$$

Note, that in the quantum mechanical derivation, dissipation is not considered. Comparing (3.27) with the classically derived splitting (3.19), reveals an interesting difference. In the quantum mechanically derived Rabi splitting, splitting takes place even without a photon in the cavity ($n = 0$), thus without an external driving force of a real photon. This so-called vacuum Rabi splitting is attributed to vacuum field fluctuations, i.e. the zero-point energy of the cavity [53, 108]. The hybrid system has discrete states with $n = 0, 1, 2, \dots$, which is referred to as the Jaynes-Cummings ladder. In the studies conducted for this thesis, the number of photons in the cavity rarely exceeds $n = 0$, since the plasmon decays in a matter of a few femtoseconds. The

experimentally probed Rabi splitting, in the attached papers, is therefore the vacuum Rabi splitting of the system.

The Jaynes-Cummings model is valid for a single optical cavity coupled to a single two-level emitter. Coupling of many emitters to a single cavity is described by the Dicke Hamiltonian or Tavis-Cummings model. For such a system, composed of a single cavity coupled to N non-interacting emitters, the previously employed Hamiltonian in expression (3.14), while ignoring dissipation, can be expanded to:

$$\hat{H} = \begin{pmatrix} \omega_c & g & g & \dots & g \\ g & \omega_{01} & 0 & & 0 \\ g & 0 & \omega_{02} & 0 & \\ \dots & & 0 & \dots & 0 \\ g & 0 & & 0 & \omega_{0N} \end{pmatrix} \quad (3.28)$$

With $\omega_{01}, \omega_{02}, \dots, \omega_{0N} = \omega_0$. Diagonalizing the Hamiltonian results in $N + 1$ eigenstates. Two are the bright coherent upper and lower polaritonic states. Whereas $N - 1$ incoherent states exist at ω_0 . Analyzing the corresponding eigenvectors shows that these incoherent states have only a weak photonic component compared to the coherent bright states and are therefore referred to as dark states. For determining the coupling strength or Rabi splitting from elastic scattering of the coupled hybrid system, see *Paper I*, all emitters can be assumed to be a giant super-oscillator. The eigenstates of a cavity coupled to such a giant oscillator lead to the (classically) derived upper and lower polariton. For studies of the inelastic processes, see *Paper III*, the incoherent states play an important role. They facilitate energy transitions from the upper polariton to the incoherent states and from there to the lower polariton, as will be discussed in the next section.

3.6 Photoluminescence of a strongly coupled system

Photoluminescence (PL) can usually be described in the following way: A photon is absorbed, and the molecule is brought via photoexcitation to an electronically and vibrationally excited state. Via emission of a phonon the molecule transitions to the electronically excited state and from there the molecule can decay to the ground state via emission of a photon. The transition rates depend on many factors such as absorption probability, lifetime of the electronic state and

the ratio of radiative and nonradiative rates. The lifetime of this process depends on the material and stability of the excited state. In WSe₂ monolayers, the lifetime is dictated by a fast relaxation process in the order of barely a few picoseconds (often attributed to defects) and a second one in the range of several hundreds of picoseconds [99, 122, 123].

One could expect for a strongly coupled system at zero detuning, the amount of PL from the UP and LP should be equally distributed, similar like the balance of UP and LP in scattering. However, experiments (see *Paper III*) show a very different picture of an asymmetric emission, mainly from the LP. This clearly indicates some kind of energy transfer between the UP and LP that has not been included until now.

In a strongly coupled system the energy states are modified. New states are introduced with modified optical properties such as a shorter lifetime for radiative processes [124, 125] and spatial coherence [126]. This changes the relaxation picture, which was described previously. As can be seen in *Paper III*, PL emission takes place mainly at the lower polariton. Several theoretical models are available to give a deeper understanding of this vibrational assisted scattering process. Pioneering work has been done by Litinskaya *et al.* and Agranovich *et al.* [127-129]. Lidzey *et al.* [124, 130, 131] have been contributing experimentally, while Michetti and La Rocca [132, 133] modeled a numerical approach, Herrera and Spano by introducing dark vibronic polaritons and based on the Holstein-Tavis-Cummings model [134], and Neuman and Aizpurua by applying the theory of open-quantum systems [135]. Del Pino *et al.* calculated many-body time dynamics of polaritonic states and found coherent vibration-driven oscillations between polaritons and dark states, leading to non-Markovian dynamics in the system [136]. Here the focus is set on the model introduced by Litinskaya and Agranovich [127-129]. While this model does not specifically explain photoluminescence in a strongly coupled system, it models the transition dynamics which finally can lead to the PL emission.

3.6.1 Upper polariton decay to the incoherent states

Excited with a high energetic photon the strongly coupled system can transition to a vibrationally excited upper polariton state. From there it will relax via emission of a phonon to the UP state. Beginning from this state, Litinskaya *et al.* describe the transition from the UP to

the incoherent states via the Hamiltonian for free phonons and for the interactions between molecular excitations and phonons as [127]:

$$H_{phon} = E_{vib} \sum_i b_i^\dagger b_i \quad (3.29)$$

And the interaction between exciton and phonons is described by the displaced oscillator model [137]:

$$H_{ex-phon} = \chi E_{vib} \sum_i B_i^\dagger B_i (b_i^\dagger + b_i) \quad (3.30)$$

Where E_{vib} is the energy of a vibrational quanta, b_i^\dagger and b_i are the creation and annihilation operators of an intramolecular phonon on the i^{th} molecule, χ is the exciton-phonon coupling and $B_i^\dagger B_i$ represents the number of incoherent excitations. The excitonic resonances can be assumed to be distributed Gaussian like:

$$\rho(E) = \frac{1}{\sqrt{\pi}\gamma_0} e^{-\frac{[E_0-E]^2}{\gamma_0^2}} \quad (3.31)$$

Where γ_0 is the broadening of the excitonic resonance E_0 , mainly due to structural disorder. Using Fermi's golden rule, the transition rate from the UP to the incoherent states can be calculated via:

$$W^{UP \rightarrow inc} = \frac{2\pi\chi^2 E_{vib}^2}{\hbar\sqrt{\pi}\gamma_0} e^{-\frac{[E_0-(E_{UP}-E_{vib})]^2}{\gamma_0^2}} |\beta_{UP}|^2 \quad (3.32)$$

$$|\beta_{UP}|^2 = \frac{g^2}{(E_0 - E_{UP})^2 + g^2} \quad (3.33)$$

With $|\beta_{UP}|^2$ the weight of the exciton fraction in the UP, E_{UP} is the energy of the upper polariton and $g = \frac{\Omega}{2}$ is the cavity-exciton coupling strength and Ω the Rabi splitting. At zero detuning the energy separation of the exciton and polariton corresponds to the coupling strength and the weight parameter $|\beta_{UP}|^2 = 0.5$, meaning that at zero detuning the polariton consists of equal contributions of exciton and photon. From (3.32) one can immediately derive that a maximum transition rate at zero detuning is reached when $E_0 - E_{UP} = g = E_{vib}$. Thus, the coupling strength coincides with the energy of a vibration. Furthermore, the expression (3.32) indicates the general trend of $W \sim \chi^2 E_{vib}^2$, dictating the transition rate proportional to the

phonon energy. As mentioned in Chapter 3.5 the coupled system possesses $N - 1$ incoherent states. Due to this high number of states the energy can transfer rapidly in the order of tens of femtoseconds [129]. Furthermore, this model assumes the UP being resonant with a vibronic excited state of the emitter.

3.6.2 Incoherent states decay to lower polariton

In the previous section it has been described how the upper polariton can decay to the incoherent states on a very fast timescale, offering a new effective non-radiative relaxation channel. The process takes place via inelastic scattering or emission of a phonon. Now the excitation lies in an incoherent state at a molecule p and the excitation can decay either (non-) radiatively directly to the ground state or by pumping the lower polariton and emission of a vibrational quanta [128]. Both processes take place [135], however here only the latter will be discussed. The final state is a vibrational excited lower polariton with a phonon at the s^{th} molecule. The transition must preserve energy and then the initial Hamiltonian reads similar to section (3.6.1):

$$H_{ex-phon} = \chi E_{vib} \sum_n B_n^\dagger B_n (b_n^\dagger + b_n) \quad (3.34)$$

Where $B_n^\dagger B_n$ is again the number of incoherent excitations and b_n^\dagger, b_n the creation and annihilation operators of an intramolecular phonon, χ the exciton-phonon coupling and E_{vib} the energy of a vibrational quanta. Applying Fermi's golden rule, the transition rate from the incoherent state to the LP can be derived. For the sake of simplicity, the broadening of the excitonic resonance is disregarded and the transition rate from all incoherent states (N) can be written as a mean value:

$$W(E_0) = \frac{2\pi\chi^2 E_{vib}^2}{N\hbar} \int_{q_{min}}^{q_{max}} \frac{Sdq}{(2\pi)^2} \frac{g^2}{g^2 + (E_{LP}(q) - E_0)^2} \delta(E_0 - E_{LP}(q) - E_{vib}) \quad (3.35)$$

With S being the area of the microcavity, E_{LP} the LP energy and $g = \frac{\Omega}{2}$ half the Rabi splitting. The integral is done over all possible wavevectors q before dephasing destroys the coherence of the LP. With further simplifications and the assumption that the energy difference between

the incoherent state and LP is resonant with a vibrational quantum $E_0 - E_{LP} = E_{vib}$ the integral in (3.35) becomes:

$$W^{inc \rightarrow LP} = \frac{\chi^2 S E_{vib}^2}{N 2 \pi \hbar} \frac{g^2}{g^2 + E_{vib}^2} \quad (3.36)$$

The final expression for the transition from the incoherent states to the LP features similar trends as the transition from the UP to the incoherent states (3.32). In both cases the transition probability is proportional to the energy of the phonon and furthermore has a maximum when the energy difference between incoherent states and polariton matches a vibrational excitation. The proportionality to the phonon energy leads to the conclusion, that a negative plasmon-exciton detuning results in a higher transition rate from the incoherent states to the LP and thereby will result in a stronger PL emission.

To derive at these transition rates, several assumptions have been made which in a real system are not valid, such as an infinite thin linewidth for the incoherent states. Even though, the predicted trends work remarkably well as can be seen in *Paper III* as well as [29, 45], where the different transition rates could explain the observed improved photostability in a strongly coupled system.

The possible energy transitions for the theoretical model, as described in section (3.6), are illustrated in Figure 3.7 (a). In this case the energy resides already in the UP. From there the strongly coupled system can make an energy transition to the incoherent states. The UP thereby needs to be resonant with a vibrational excited incoherent state and can from there relax to the incoherent ground state via emission of a corresponding phonon. Now the excitation can decay either via photon emission to the molecular ground state or make another energy transition to the vibrationally excited LP. Under photon emission the molecule can relax to the vibrational excited ground state and finally, via phonon emission relax to molecular ground state. Note, that the number of incoherent states outweighs by far the number of coherent polaritonic states, resulting in fast and efficient decay from the UP to the incoherent states. Furthermore, the transition rate from the incoherent states to the excited LP is rather slow compared to the transition from the UP to incoherent states [129]. Thereby, PL emission from the UP is expected to be a rather inefficient process. The transition rates are displayed in a dispersion plot of a strongly coupled system in Figure 3.7 (b). The color of the arrows represents three different plasmon-exciton-detuning regions as determined qualitatively from expressions

(3.32) and (3.36). Since the decay from the UP is rather fast the rate from the incoherent states to the LP dictates the PL emission rate. In a blue-detuned case (blue arrows) the transition rate to the LP is rather slow and little PL from the LP is expected. On the opposite side of the spectrum, for a red-detuned strongly coupled system (orange arrows) the transition is more efficient and a higher number of emitted photons from the LP is expected. This behavior continues until the wavevectors for the LP become too small or too large. Figuratively one could describe these limiting areas as when the LP asymptotically approaches either the bare plasmon at low energies or bare exciton at higher energies.

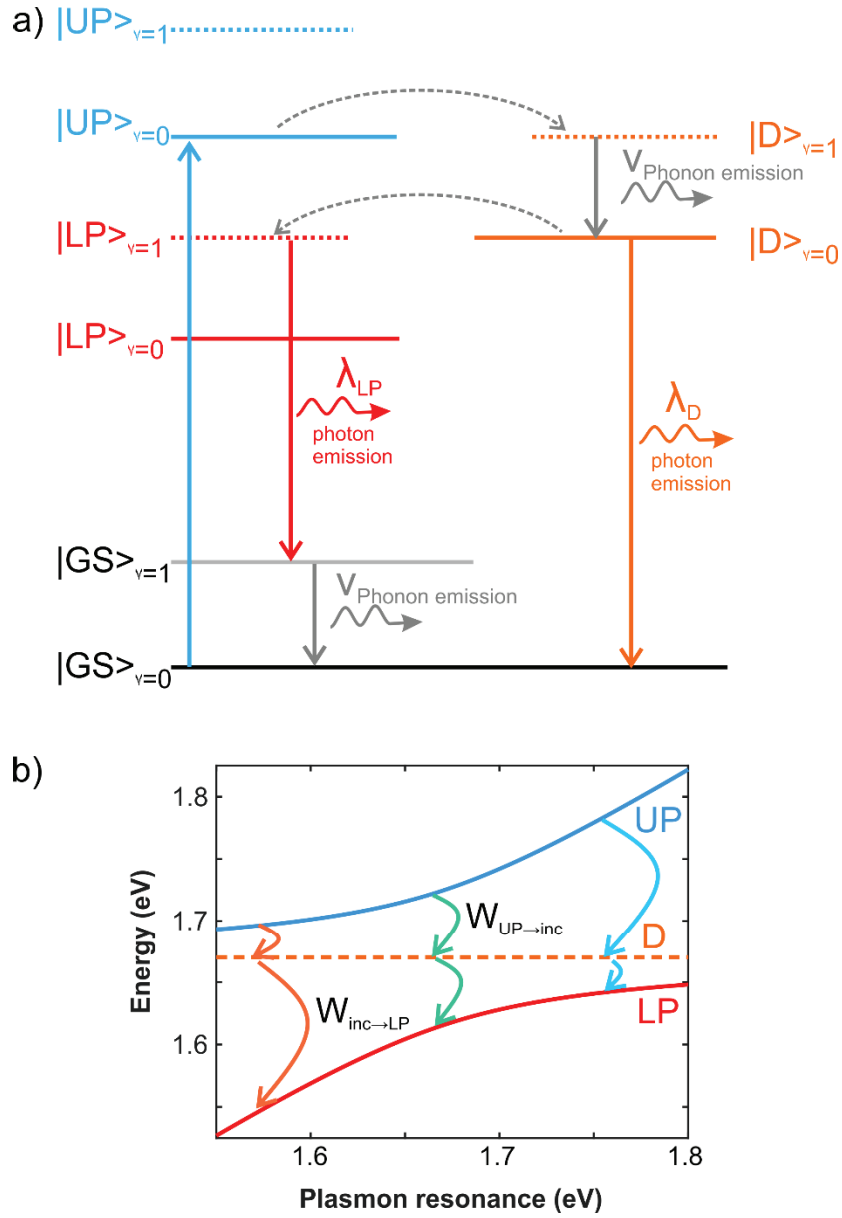


Figure 3.7. (a) Energy diagram for a strongly coupled system illustrating inelastic scattering from the upper polariton (UP) to the incoherent states (D) and the lower polariton (LP) via phonon emission. The final state is the ground state (GS). V marks the vibrational ground or excited state. (b) Dispersion plot with the UP (blue), incoherent states (orange) and LP (red). Arrows indicate the transition rates for three different plasmon-exciton detuning. A larger arrow indicates a faster transition rate.

Chapter 4: Experimental Methodology

This section is intended to present and discuss all experimental methods that were employed to study the systems in this PhD project. During my PhD studies, two major study projects have been conducted and while strong coupling is the focus of this thesis, I will also present more, unpublished data, for the sake of completeness. Therefore, this section will cover not only fabrication and characterization methods as presented in the attached publications, but additional experimental data and methods are also presented. The first part describes the fabrication methods for the nanostructures. The second part explains the spectroscopic measurements and for what they are useful. The last part focuses on results, that are not part of the main PhD project, and the focus is on nonlinear laser microscopy of nanostructures.

4.1 Sample preparation of BPs, TMDC and colloidal lithography

The following subsections are focused on the sample fabrication methods. It will cover the exfoliation and transfer of the TMDC and fabrication of the hybrid system with gold nanobipyramids. Furthermore, the fabrication of thin gold films perforated with a high density of nanoholes. The synthesis of BPs has been carried out by B. Munkhbat. However, it's described in this thesis, since the BP is one of the most important components for these studies.

4.1.1 Fabrication of hybrid structures

In order to prepare the samples for strong coupling, individual TMDC flakes have to be exfoliated onto, in case of this project, Si/SiO₂ substrates [138]. WSe₂ is available as a bulk crystal (HQ graphene). With the help of simple scotch tape, small mono- and multilayer of the WSe₂ crystal are carefully cleaved and transferred on a stamp made of polydimethylsiloxane (PDMS). This transfer process usually takes place in a cleanroom environment to not contaminate the original bulk crystal. The final transfer of the WSe₂ layers takes place under bright-field microscopy by pressing the PDMS stamp on the Si/SiO₂ substrate where the material has a higher adhesion and will remain after lifting the PDMS stamp. To fabricate the

hybrid structure, a solution containing gold nanobipyramid nanoparticles is drop-casted directly on the target mono- or multilayer. Removing the solution can be done either by letting it evaporate at ambient conditions or soaking it up carefully with a dust-free tissue. The density of particles on the sample is determined by the concentration in solution and time before removal of the rest solution on the TMDC. The orientation of particles on the sample is random whereas the size distribution is determined in the growing process of the nanoparticles. Small variations from particle to particle allow for different plasmon-exciton detuning in the experiments and thereby reconstruction of the dispersion relation in strong coupling.

Exfoliation is one of the fastest and most cost-effective ways of fabricating high quality few layer TMDC material. However, there are a few constraints with this method. First, the final flake size is limited to few tens of micrometers. Furthermore, the orientation of the material with respect to its crystal structure is essentially random and hard to control. And finally, while the resulting material after transfer is often of high quality with low defects, the transfer process itself makes use of PDMS as a transferring material. This can leave residues of PDMS on not just the TMDC itself but also on the surrounding surface on the final Si/SiO₂ substrate. This effect is for example visible in Figure 4.3 as little sticky bubbles on the substrate, potentially changing the affinity to polar solutions. During the subsequent particle transfer process, the BP solution sometimes avoids the area where PDMS residues are left on the Si/SiO₂ substrate. A slight improvement can be achieved by mixing the BP solution with isopropanol.

A different method for creating few layer TMDC material is chemical vapor deposition (CVD). In this process the material is directly evaporated on the target substrate and starts to form small seeds and grows from there. This process can create large scale areas of nearly complete coverage with TMDCs. While there has been a huge effort of producing high quality samples, the number of defects is usually higher than for exfoliated layers from a bulk crystal. However, larger size and better substrate coverage lead to a high interest in creating high quality TMDC few layer systems with CVD [139-143].

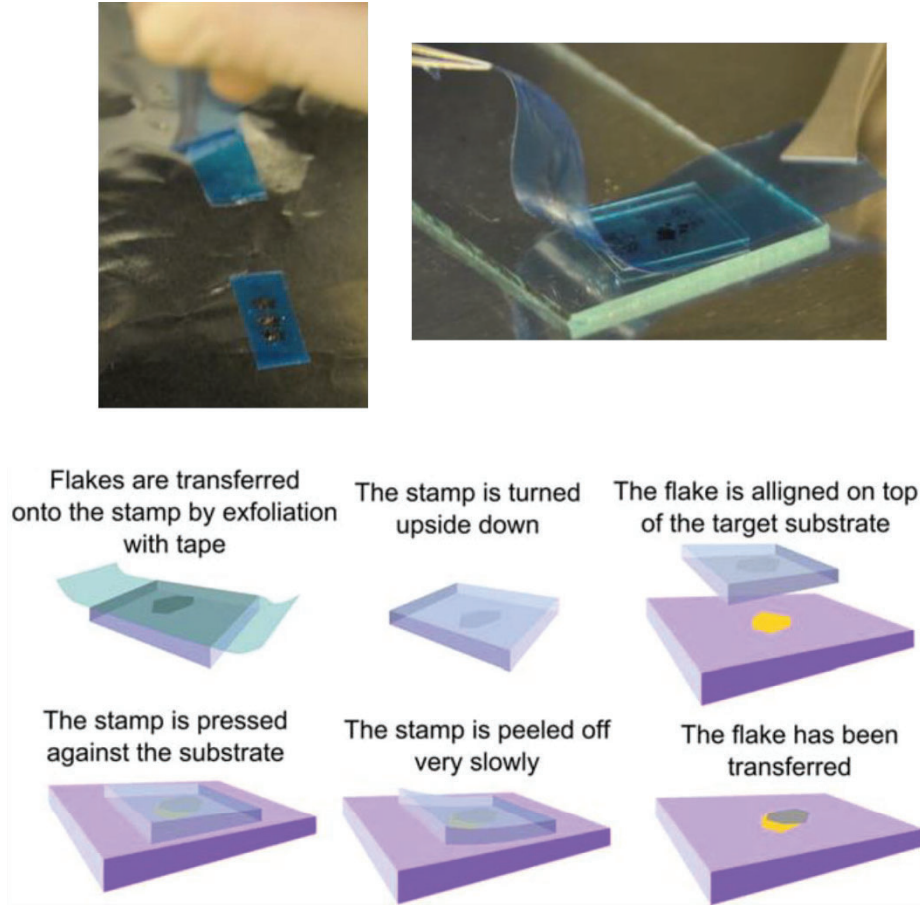


Figure 4.1. *Mechanical exfoliation of TMDC few-layer material from a bulk crystal. First, few-layer flakes are stripped of the bulk crystal with an adhesive tape. Subsequently the flakes are transferred to a PDMS stamp. In a last step they are transferred to the target substrate. Images from [138].*

4.1.2 Hole colloidal lithography

Samples with nanoholes in optically thin gold films ($d_{film\ thickness} < 100\ nm$) have been produced via hole colloidal lithography (HCL). HCL is the method of choice when large areas, fast and cost-effective production is required. The final sample will be composed of a high density of nanoholes in a metal film with a short-range order that depends on the particle size and density. The basic steps of HCL are illustrated in Figure 4.2 (a). A glass substrate is prepared by sonication in isopropanol and plasma cleaning of the surface. This process removes any unwanted residues. Afterwards a 5% solution of aluminum chlorohydrate (ACH) is put on

the surface, leaving it positively charged. After rinsing and drying the sample with nitrogen, a solution of plastic (polystyrene) colloids can be deposited on the surface. The colloids are small spheres with a negative charge. This negative charge lets them adhere to the positively charged sample surface and furthermore repel each other, resulting in self-organization. After about one to two minutes the whole sample surface is evenly covered by the colloids and the sample can be rinsed with water and dried with nitrogen gas to remove any free colloids. The result is a high-density coverage of colloids on the surface with a specific short-range order. The nearest neighbor (NN) distance is determined by the number of negative charges in the colloids, which usually correlates to the particle size. Smaller particles will have a shorter NN distance and larger nanoparticles a larger NN distance. As a reminder, in section (2.2.3) it was discussed that the distance between holes in such a thin metal film leads to SPP resonances. Tuning of the SPP resonance frequency can be done by either changing the metal film thickness, or by changing the NN distance. Note, while it is not possible to change the charge of the particle itself, it is possible to introduce salt in the particle solution resulting in more effective screening of the particles [14] and thereby a higher density on the surface with shorter NN distance, as seen in Figure 4.2 (e) and (f). However, too much screening can result in particle agglomeration.

The size of the particles will determine the final hole diameter, which will correlate to the localized plasmon resonance frequency. DF scattering from two nanoholes with the same thickness, albeit different diameter, is compared in Figure 4.2 (d). Different sized particle solution can be bought directly from companies. However, having many different solutions is not very cost effective and furthermore the size distribution in bought colloid solutions becomes worse for smaller sized particles (below $\sim 100\text{ nm}$ diameter). A different way of size control is the following process: After deposition of the colloids on the surface, the sample is washed with boiling ethylene glycol. This ‘bakes’ the particles stronger to the surface. Subsequently the size of the plastic particles can be reduced via plasma oxygen etching [68, 144]. The etching rate in this case is roughly $\sim 1.1\text{ nm/s}$ (see Figure 4.2 (b)) and thereby offers a new way for plasmon frequency control. Additionally, etching the particles does not change the NN distance and thereby the SPP resonance nearly remains constant.

When the colloids have the correct diameter, the metal evaporation process can be proceeded. First a thin 1nm film of chromium (Cr) is evaporated smoothly over the whole sample area. This serves as an adhesive layer for the target gold film, since otherwise the gold does not

properly adsorb to the glass surface. After Cr evaporation, gold can be deposited with an evaporation rate of about 1 \AA/s until the target film thickness of usually 20 to 40 nm. As a final step, scotch tape is placed on the sample. Since the polystyrene spheres are larger than the metal film thickness, the adhesive will only be in contact with the high-density colloids and not the final gold surface. With a simple lift-off the colloids stick to the scotch tape and can be peeled of the metal film. This leaves the inverted structure in the gold film, which in this case are little nanoholes. For the target localized plasmon resonance the volume of the void is determining the resonance frequency, meaning it is the combination of hole diameter to film thickness. Thereby this opens two parameters for tuning of the LSP resonance [145]. Note, that by changing the hole diameter the LSP resonance is shifting, but the transmission of light through the hole is changing too with $t \sim \left(\frac{r}{\lambda}\right)^4$. The extinction spectrum of such a nanohole film is plotted together with the extinction spectrum of an un-patterned gold film of equal thickness in Figure 4.2 (c). The pure gold film features a single extremum around $E_{IT} = 2.4 \text{ eV}$ which is the beginning of the interband transitions in gold and will result in high absorption. In the patterned gold film two new distinct extrema are visible. The first one is a peak at around $E_{SPP} = 2 \text{ eV}$ and corresponds to the SPP resonance of the film plasmons that are resonant with the average NN distance of the holes. The second one is a dip in the extinction spectrum at around $E_{LSP} = 1.6 \text{ eV}$. This dip corresponds to a localized plasmon resonance and is depending on the hole diameter and film thickness. Finally, it is also possible to fabricate isolated hole samples. By reducing either the concentration of spheres in solution or by shortening the adhesion time, it is possible to get samples with very low densities of holes, where each hole can be treated individually without any interaction of other holes. This reduces possible interactions to the LSP mode only.

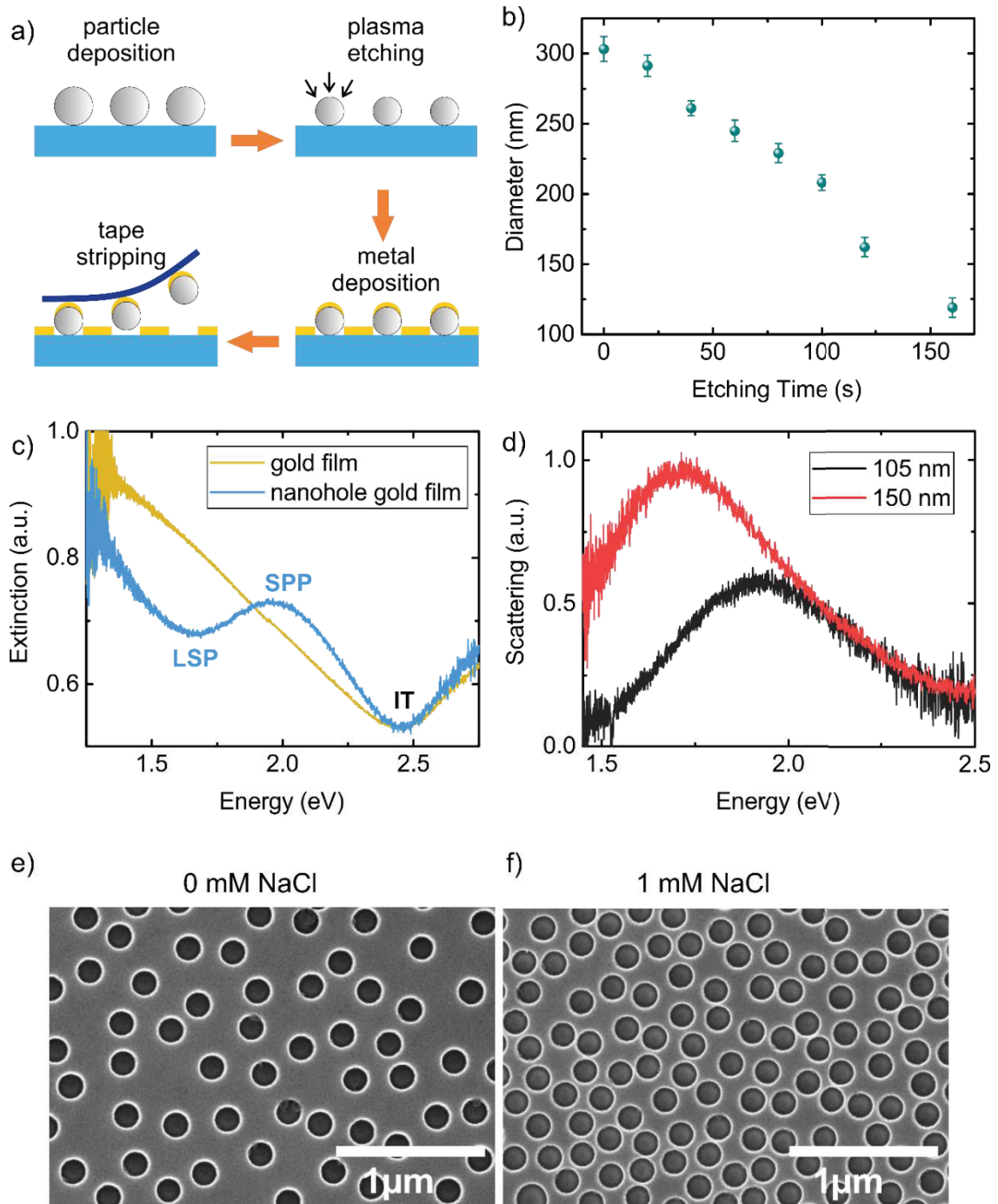


Figure 4.2. Hole colloidal lithography. (a) Illustration of fabrication process. (b) Final nanohole diameter vs etching time. (c) Extinction spectrum of a pure gold film (yellow) and a gold film with same thickness but a high density of 150 nm nanoholes. IT indicates the beginning of the interband transitions in gold, SPP and LSP mark the two additional extrema in the nanohole thin film. (d) Scattering of two individual nanoholes with different diameter but same thickness. (e), (f) SEM image of a high density nanohole film, where the solution had (e) 0 mM NaCl and (f) 1 mM NaCl.

4.1.3 Synthesis of gold nanobipyramids

Materials: Silver nitrate (AgNO_3 , 99.9999%), Gold(III) chloride trihydrate ($\text{HAuCl}_4 \cdot 3\text{H}_2\text{O}$), L-ascorbic acid (AA), trisodium citrate dihydrate, sodium borohydride (NaBH_4 , 99%), 1N hydrochloric acid solution (HCl), and hexadecyltrimethylammonium bromide (CTAB) were purchased from Sigma-Aldrich at the highest purity grade available. All glassware and stir bars were thoroughly pre-cleaned and dried prior to use. Ultra-pure distilled water (Millipore, 18 $M\Omega\text{cm}$) was used in all preparations.

Synthesis of gold nanobipyramids: Gold nanobipyramids were synthesized using a seed-mediated method in aqueous solution according to [15-17]. Briefly, citrate-capped pentatwinned crystalline gold seed particles were prepared by adding a fresh, ice-cold 150 μL of 10 mM NaBH_4 solution into a mixture solution composed of 125 μL of 10 mM HAuCl_4 , 250 μL of 10 mM sodium citrate, and 9.625 mL of DI water. The seed solution was kept for 2 hours at room temperature before use. Then, a CTAB growth solution was prepared by sequential addition of 2 mL HAuCl_4 (10 mM), 400 μL of 10 mM AgNO_3 , 800 μL of 1 M HCl, and 320 μL of 100 mM ascorbic acid into 40 mL of aqueous CTAB solution (100 mM). The seed-solution (0.1 – 2 mL) was then added into the growth solution, followed by gentle inversion mixing for 10 s. The reaction solution was left undisturbed overnight at room temperature. The pentagonal form of the BP is based on the crystalline structure of the seed. A CTAB bilayer and silver monolayer passivate the sides and restrict further growth. The plasmon resonance of the gold nanobipyramids samples grown in the CTAB growth solutions was tuned by varying the amount of the seed solution and growth time. Finally, the product was washed several times to get rid of excess chemicals and redispersed in DI water for further use.

The resulting nanobipyramids have a high crystallinity, a pentagonal base and are elongated with two sharp edges at the end. A detailed STEM image can be found in Figure 4.3 and more in the supporting information of *Paper I* in Figure S5 and S6, highlighting the crystallinity and sharpness of the tip. The optimal size of the BP, to couple with exciton in WSe_2 , is about 100 $nm \times 40 nm$ with an aspect ratio of about ~ 2.75 . Due to the elongated shape, the BP supports a narrow plasmon resonance around 750 nm along the long axis with two hotspots at the ends. Compared to nanorods, the sharp edges lead to sharper linewidths with higher electric field intensities and higher sensitivity to the surrounding medium [16, 146, 147]. The

geometrical shape of the BP, when placed on a flat surface, allows only one of the two hotspots to be in close vicinity with this surface while the other will be lifted by the full transversal height of the BP and its electric field strength decays before reaching the surface.

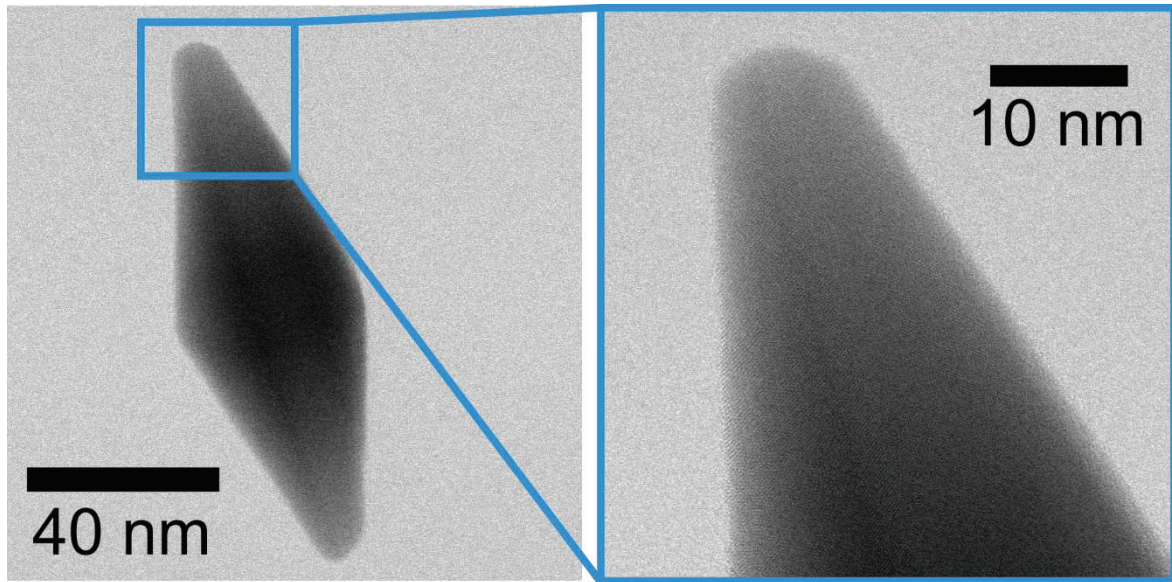


Figure 4.3. *STEM image of a nanobipyramid.*

4.2 Atomic force microscopy

In nanophotonics, often it is important to investigate surface specific features, but the samples are smaller than the diffraction limit of light. Light microscopy is not suitable in such a case and a near-field approach needs to be chosen. Atomic force microscopy (NTERGA, NT-MDT) has been employed to study the topography in certain projects for this thesis. An atomically sharp gold coated single-crystal silicon tip with a tip-curvature radius of 6 nm (NSG01 and NSG10) is probing the surface in non-contact mode. The tip is driven at resonance frequency and brought into contact with the sample surface. While approaching, the tip will be exposed to fields on the surface and be repulsed when getting near contact. This will be reflected in a change in the actual frequency, which is probed with a laser being reflected from the tip. The difference between driving frequency and actual frequency is translated to the distance between tip and surface and feeds a feedback loop of the AFM. This way with an AFM the topography

of a sample can be scanned. The maximum possible resolution hereby depends on the ‘sharpness’ of the tip. The collected raw data is finally processed by data leveling to remove any possible tilt of the surface or tip movement. A topographic image of a multi-layer WSe_2 flake with a thickness of around 200 nm is shown in Figure 4.4.

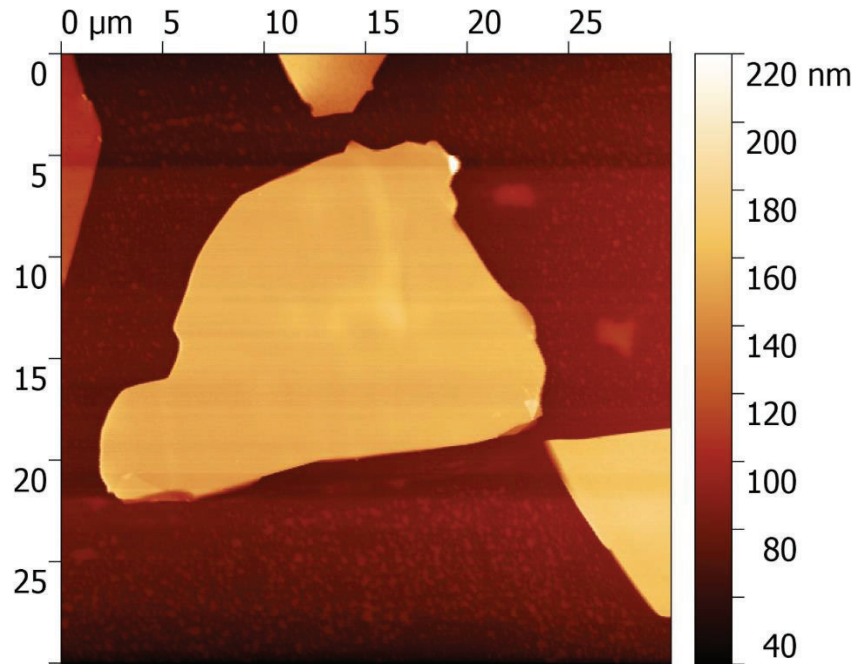


Figure 4.4. AFM image of a WSe_2 multilayer flake with a thickness of around 200 nm.

4.3 Dark-field microscopy

Nanoparticles are difficult and sometimes even impossible to observe and analyze in conventional transmission-light microscopy because of their small scattering and absorption cross-sections, see section (2.2.2). One way to study them is simply by reducing the background signal. Dark-field (DF) microscopy utilizes the idea of only collecting light which has actively interacted with the sample, as illustrated in Figure 4.5. In DF microscopy a special condenser illuminates the sample with high angular excitation light, in air usually around 0.8 – 0.9 NA. In transmission mode the collection is done with an objective lens with lower numerical aperture, unable to collect the direct transmitted light beam. In reflection mode the light collection-path includes a mechanical object, usually a specific ring, that blocks the high-

angular light rays. Without any sample in the focus the image remains dark. However, if a small particle is placed in the excitation focus, it will scatter light at different angles and intensities, depending on its geometrical form and composition. This scattered light can pass the ring and reach the detector. Thus, in DF microscopy such a particle would appear as a bright spot on a dark background. With small noble metal nanoparticles, LPSRs can be utilized to enhance the scattering cross-section at the plasmon resonance frequency, making DF the method of choice for plasmonic nanoparticle analysis. A polarization analyzer placed in the detection path permits to determine the orientation of plasmonic particles, whose dipoles are aligned along the plasmon oscillation at resonance. As last steps the collected signal needs to be corrected by a reference spectrum which is a representation of the actual light source spectrum. And finally, according to expression (2.20) the intensity needs to be corrected by ω^4 to receive the true scattering cross-section.

For this thesis project an upright Nikon Eclipse LV150N microscope, equipped with a standard (100 W) halogen lamp operated at maximum intensity for white light illumination has been employed. A special lens focuses the light through the outer ring of an 100x objective lens (Nikon TU Plan ELWD 100x $NA = 0.8$), illuminating the sample at high incident angle. The collection aperture is limited to a smaller NA than 0.8 and thus limits the collection to light scattered at a non-zero diffraction order. The light detection is achieved with the hyperspectral imaging system, more details in Chapter (4.5). In short, the collected photons pass through a liquid crystal tunable filter (LCTF) (VariSpec SNIR, 650 – 1100 nm), acting as linear polarization analyzer and spectral filter, and finally are detected by an electron-multiplying charge-coupled device (EM-CCD) camera (Andor, iXon DV887).

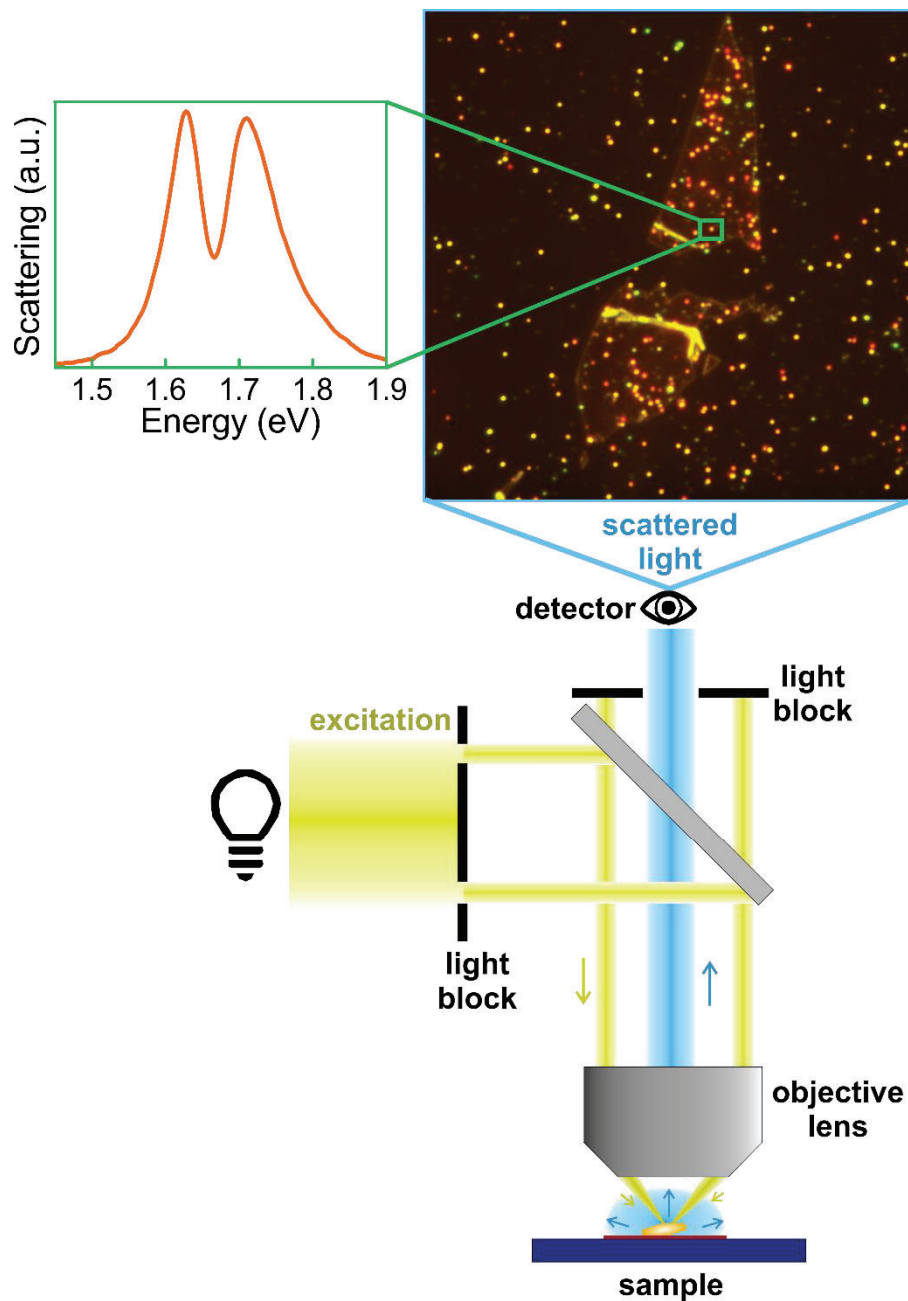


Figure 4.5. Dark-field microscopy. The sample is illuminated by high angular light beams and only scattered light at different angles reaches the detector. The image shows DF scattering of nanoparticles on a WSe_2 monolayer flake. The inset shows a scattering spectrum from a strongly coupled system.

4.4 Photoluminescence microscopy

Bulk WSe₂ has an indirect bandgap, and thus the PL of the crystal is very weak. However, as introduced in Chapter (2.3), when thinned down to a single layer, the material becomes a direct bandgap semiconductor. In order to understand *Paper III*, one has to understand the underlying radiative and non-radiative processes in these TMDC flakes. The semiconductor has several higher order electronic states which themselves have a full band of vibrational states. When excited by a photon, an electron can occupy an excited electronic state with vibrational component. From there it can relax to the energetical lowest electronic state via release of phonons. From this state the electron can relax to a vibrational excited ground state level through either emission of phonons (non-radiative) or photons (radiative). The ratio of radiative to non-radiative rates determines the luminescence strength of the material. Analysis of the emission wavelength and intensity offers insight in the internal band-structure as well as coupling between the excitons in WSe₂ to the plasmons in the BP. When the exciton lower electronic energy level is hybridized with the plasmon resonance from the BP (strong coupling regime), the PL spectrum differs from the bare exciton PL spectrum in WSe₂ monolayers, as explained in section (3.6). Few-layers of WSe₂, have still measurable PL, though several orders of magnitude less, and decreasing with an increasing number of layers. Therefore, in *Paper III* we focused on monolayers as well as bilayers.

To investigate the PL response from the strongly coupled system, a setup as illustrated in Figure 4.6 is employed. The sample is illuminated with a white light LED (Cool LED, pE-300). First the light beam is made colinear, then spectrally filtered by a band pass filter (Chroma, HQ470/40x) to have only light with short wavelength and high excitation energy left. A mirror reflects the light in the objective lens where it is focused on the sample. The focus spot has the size of the full field of view, illuminating the whole sample evenly. Wide-field illumination enables analyzing of many individual particles at once. The sample will, according to its absorption and scattering cross-sections scatter light elastically and inelastically. An objective lens collects all lights from the sample and a long pass filter (Chroma, HQ500LP) transmits only the light that is emitted via inelastic processes from the sample. Finally, the detection setup is the same as for DF in the previous section. An LCTF will filter the light spectrally and for linear polarization. The transmitted photons are then detected with an EM-CCD.

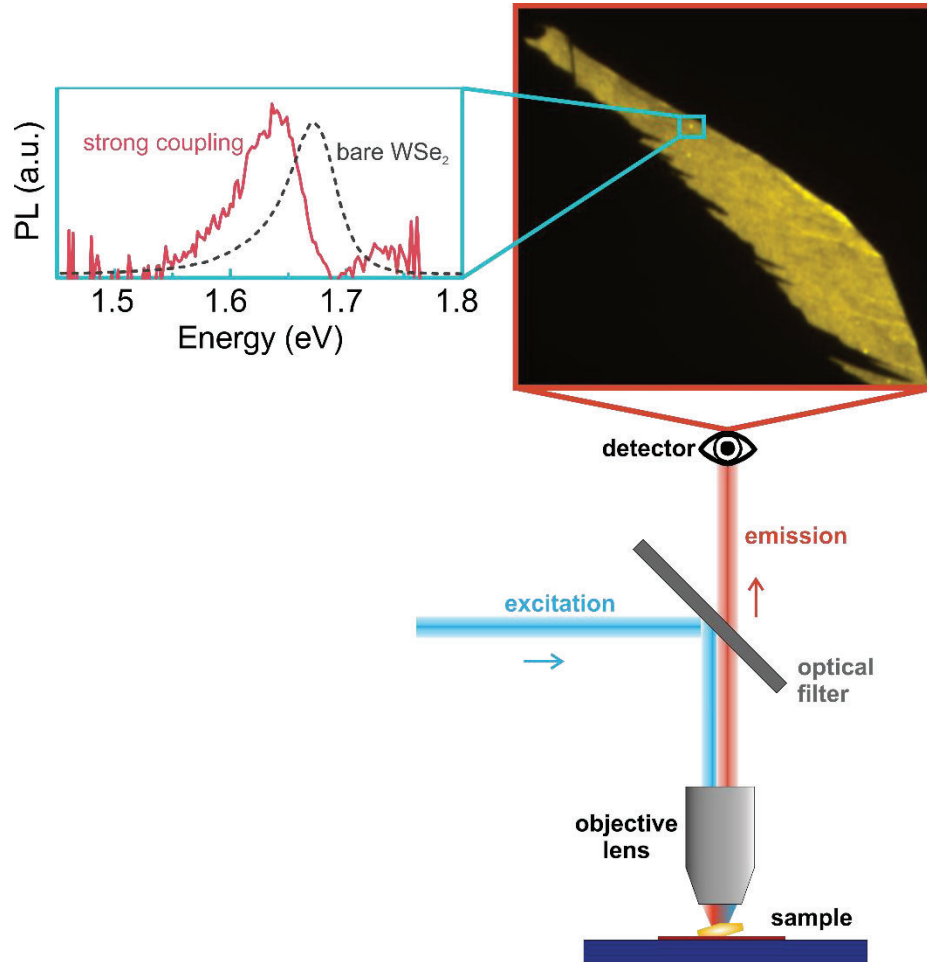


Figure 4.6. Illustration of photoluminescence microscopy. High energy excitation of the sample (blue) follows radiation via inelastic processes (red) which is collected by a hyperspectral imaging system. The image displays a WSe₂ monolayer, the bright spots are strongly coupled nanoparticles. The inset shows PL spectrum of a strongly coupled system (red solid line) versus uncoupled PL from excitons in WSe₂ (dark dashed line).

4.5 Hyperspectral imaging system

The most common way of doing a spectral analysis of nanoscopic samples is to use a spectrometer. A spectrometer utilizes gratings to spread the spectral components of the incoming light on a CCD camera [148]. The very nature of this analysis restricts the method to a single particle analysis.

A different approach, based on the hyperspectral imaging system, enables large scale analysis of many particles simultaneously. It consists of a liquid crystal tunable filter (LCTF) (VariSpec SNIR, 650 – 1100 nm) and an electron-multiplying charge-coupled device (EM-CCD) camera (Andor, iXon DV887). The LCTF utilizes a Lyot-Öhman filter concept for enabling monochromatic light transmission [149-151]. The camera subsequently takes large scale images at each respective wavelength. In post processing the corresponding images can be fused in a single hyperspectral image stack, containing a full spectrum at each pixel. The LCTF is built by stacking several Lyot-cells after each other, each consisting of two linear polarizers with a liquid crystal cell sandwich in between. The crystal cell acts as a retarder for the wavelength λ and can be tuned by applying different voltages. Each subsequent crystal cell has double the thickness as the previous one and the transmission through a single cell is determined by:

$$T = \frac{1}{2} \cos^2 \left(\frac{\pi \beta d}{\lambda} \right) \quad (4.1)$$

Where β is the birefringent of the cell with length d . The factor $\frac{1}{2}$ is a consequence of using linear polarizers. The final transmission for the chosen wavelength λ becomes then:

$$T \sim \prod_n^N \frac{1}{2} \cos^2 \left(\frac{n \pi \beta d}{\lambda} \right) \quad (4.2)$$

The resulting transmission for individual Lyot filters with different thickness is plotted in Figure 4.7 (a). When adding these filters in a row the final transmission is a product of all individual filters. Normalized transmission spectra for a single filter against a filter set with three filters and finally with ten filters are shown in Figure 4.7 (b). The filter becomes more and more narrow in the transmission window, the more filters are used. Note however, the spectra are normalized for visibility. Owing to the linear polarizer, every filter has a loss in an ideal case of 50%. In practice, the choice of the number of filters depends on the targeted

spectral transmission linewidth against the total transmission efficiency. In case of the filter used in these studies, the transmission linewidth was 10 nm.

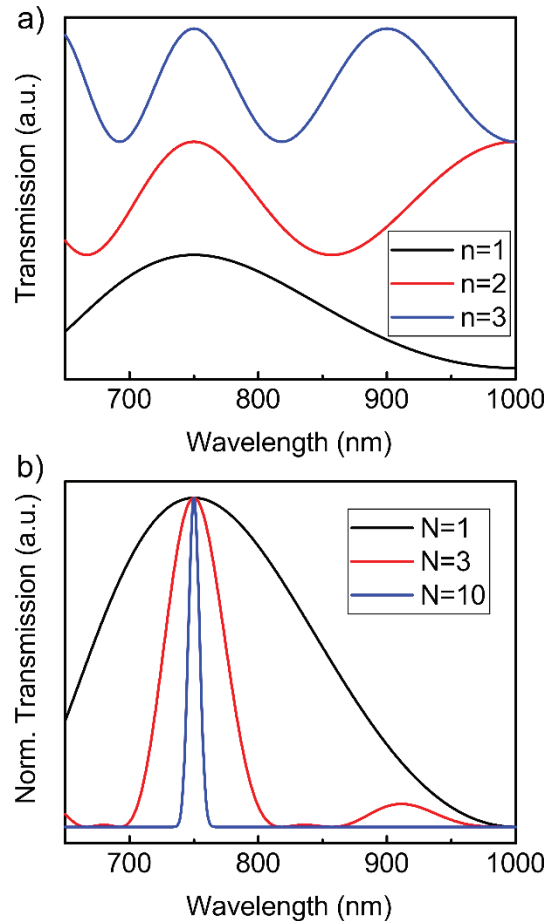


Figure 4.7. Lyot filter transmission for a wavelength $\lambda = 750$ nm. (a) Transmission spectra for three individual Lyot filters with a different thickness. (b) Normalized transmission spectra for a filter set of 1, 2 and 3 Lyot filters in a row.

To begin creating a hyperspectral image, the LCTF is tuned to the first target wavelength. Light from the sample is spectrally filtered by the LCTF and collected by a camera. Subsequently the wavelength for the peak transmission of the LCTF will be tuned by a small increment and again captured by the camera. The process will be repeated until the full range of interest is covered. Afterwards, in a post processing step, each individual image will be labeled with the corresponding wavelength and concatenated to the final hyperspectral image. The information stored in a hyperspectral image is displayed in Figure 4.8.

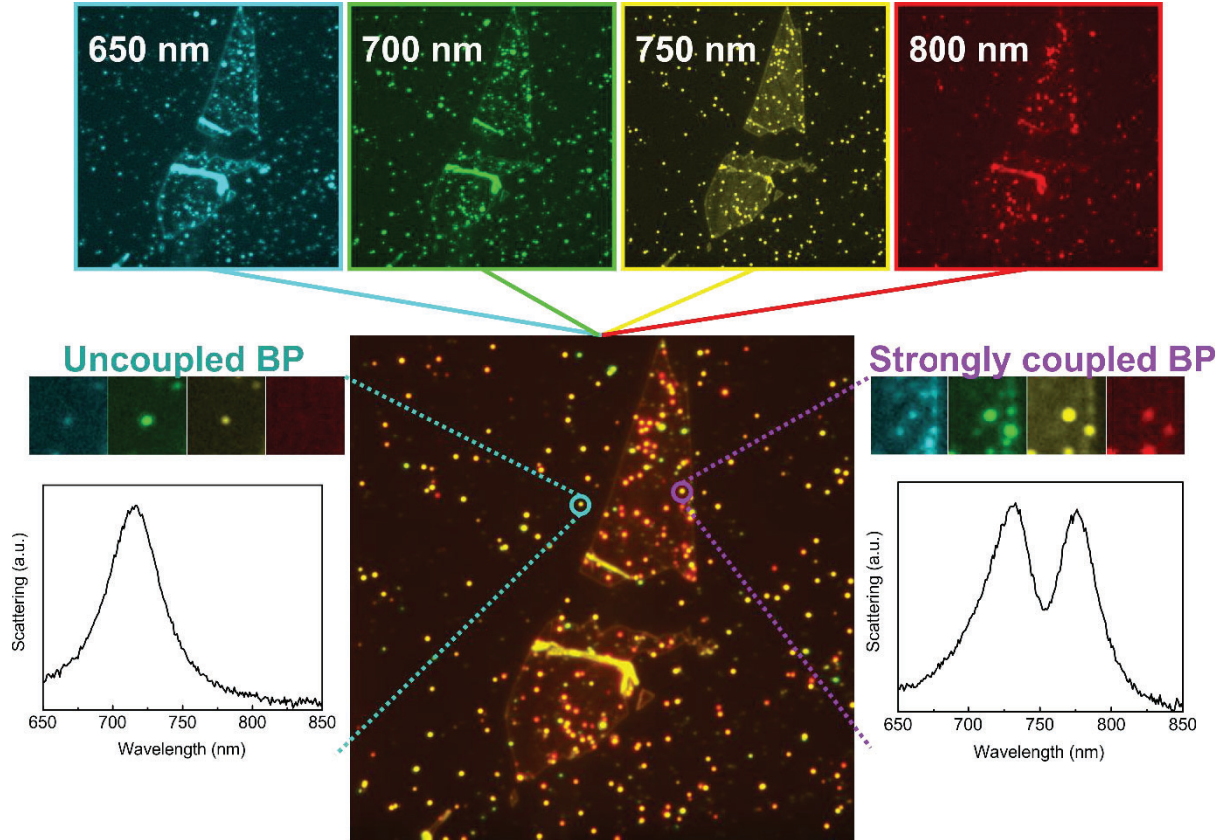


Figure 4.8. Hyperspectral imaging technique. Each pixel contains the information of the full spectrum of the collected light. Left inset shows the spectral information of an uncoupled BP on Si/SiO₂ substrate. Right inset shows a scattering spectrum of a BP strongly coupled to the excitons in the underlying WSe₂ flake.

4.6 Electron microscopy

All the afore mentioned methods are either limited by the diffraction of light or by relying on a physical probe to study the topography. However, for precise non-intrusive analysis of the nanoparticles studied in this thesis, electron microscopy has been employed. The BPs or nanoholes appear in DF or PL studies as mere bright dots, and while polarization dependent measurements can be used to determine the orientation of some particles, they contain no information about the actual size and composition. Electron microscopy can analyze structures even on an atomic level, as can be seen in *Paper I*. In the studies done for this thesis, scanning electron microscopy (SEM) and tunneling electron microscopy (TEM) has been employed to correlate the actual shape and orientation of the nanoparticles with the data as obtained from light microscopy. SEM is a necessary step to confirm that each measurement has been done on an isolated nanoparticle and furthermore has been used to analyze the aspect ratio, which correlates to the LSPR frequency (Figure 4.9). The drawback of electron microscopy is, that the electron bombardment of the sample is quite harsh and results in modification and damage of the optical properties of the strongly coupled samples, especially for the TMDC material.

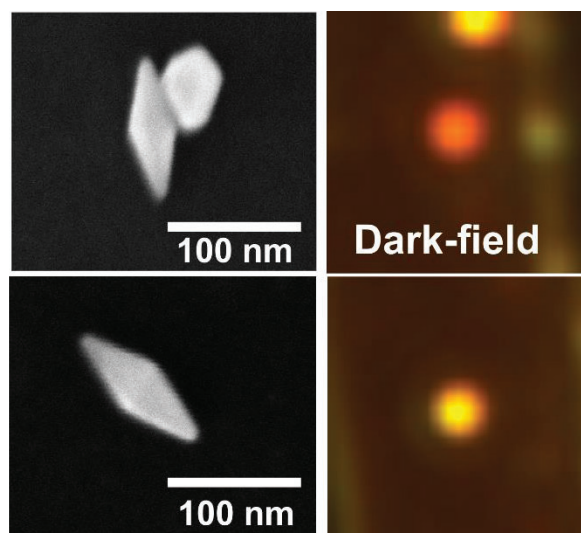


Figure 4.9. *Correlating DF images with SEM. Electron microscopy is necessary to confirm the actual particle shape and surrounding.*

4.7 Reflectivity measurements

An important optical property of nanostructures is the efficiency to absorb light. Absorption represents the oscillator strength of an optical mode such as excitons in TMDC. Reflection spectra at normal incidence were collected using a 20x objective (Nikon, $NA = 0.45$) to determine the absorption of the TMDCs. The sample is illuminated by a bright-light halogen light source and the reflected light is collected via a fiber and directed to a spectrometer. The extracted spectrum is subsequently normalized with reflection either from a standard dielectric-coated silver mirror, or light reflected from a substrate-area next to the sample of interest.

4.8 Nonlinear laser microscopy

An applied electric field pulls positive charges towards the direction of the field and negatively charged particles in the opposite direction. A photon is an electro-magnetic wave and in the visible to near-infrared region has a frequency several hundreds of THz . While electrons can react nearly instantaneously to the perturbation of such an electro-magnetic wave, nuclei are too heavy to follow this fast oscillation. As a result, the electrons will be shifted from their equilibrium positions and hence induce a dipole moment. For low electric field intensities, the electron response can be assumed to be harmonic. However, for higher field intensities the electrons can't follow the electric field linearly any longer, which will create an anharmonic response. The polarization can be written as a function of the susceptibility χ :

$$P(t) = \epsilon_0 [\chi^{(1)}E(t) + \chi^{(2)}E^2(t) + \chi^{(3)}E^3(t) + \dots] \quad (4.3)$$

Where ϵ_0 is the electric permittivity in vacuum and $E(t)$ is the applied electric field [109, 152]. $\chi^{(n)}$ is the nonlinear susceptibility of the n^{th} order. From expression (4.3) one can derive that the resulting intensities will be clearly identifiable by correlating the intensity of a measured signal to the incoming intensity. Furthermore, a first order process can be a single photon process, while for a second order process two incoming photons are required and even more for higher order processes. This can directly be translated to the general probability of such a process taking place, since the probability decreases with the number of photons required for a specific process. Nonlinear microscopy offers several major advantages compared to

conventional linear microscopy. In confocal microscopy the excitation volume is rather larger, because of the simplicity of the process, many molecules will be excited at once. In nonlinear microscopy the target process only takes place in the high intensity center of the focus, reducing intrinsically the excitation volume. Furthermore, the probability of nonlinear processes depends on the material, resulting in chemical and geometrical specificity of the sample [109].

The following sections are giving an overview of the different nonlinear microscopy techniques that have been employed. Nonlinear microscopy was not part of the main study in this thesis, and thereby found its way only in the methods section. The study of nonlinear effects on strongly coupled systems will be discussed in the outlook.

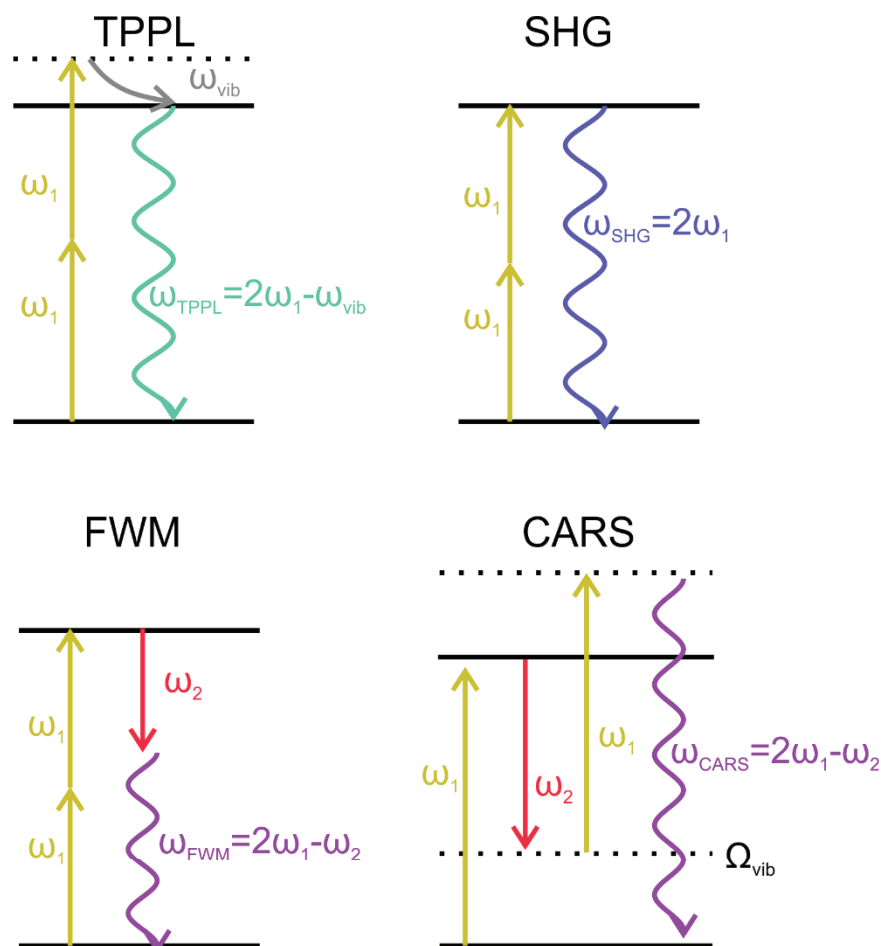


Figure 4.10. Nonlinear microscopy techniques. Two-photon photoluminescence (TPPL), second harmonic generation (SHG), four-wave mixing (FWM) and coherent anti-Stokes Raman scattering (CARS). Solid lines represent electronic states, whereas dashed lines represent vibrational excited or virtual states. Straight arrows indicate an excitation photon, whereas the wavy arrows represent an emitted photon. Color scheme of the arrows is chosen to loosely represent to the energy spectrum of light. The gray arrow indicates vibrational relaxation.

4.8.1 Introduction to different nonlinear laser microscopy methods

In this section several nonlinear microscopy techniques that have been employed in this thesis are explained and discussed.

The first techniques are **two-photon excited photoluminescence** (TPPL) and **second harmonic generation** (SHG). Both processes rely on excitation with two photons during the lifetime of a (virtual) state. The different methods, in an illustrative energy diagram, are shown in Figure 4.10. From this perspective, the major difference between TPPL and SHG is that SHG is the direct result of a special case of sum frequency generation and the signal is at $\omega_{SHG} = \omega_1 + \omega_1$ where ω_1 is the frequency of two incident photons with a fixed phase relationship. SHG is a quasi-elastic scattering process since the energy is conserved between the three participating photons. Therefore, the linewidth of the final SHG signal correlates directly with the linewidth of the excitation laser. SHG is a highly specific process because one of the requirements is the lack of a center of inversion symmetry.

This specificity however is fulfilled in uneven numbers of WSe₂ layers [100, 153-156]. The hexagonal structure, as discussed in section (2.3) features in bulk form a d_{6h} symmetry which is then reduced in a monolayer to d_{3h} . In SHG this results in a 6-fold polarization dependent intensity pattern as can be seen in Figure 4.11 (a). The orientation of the flower pattern is correlated to the crystal axis and allows the determination of the crystalline structure of the sample. Furthermore, the symmetry of the polarization pattern can be interpreted as specific strain on the WSe₂ layer [157]. In a strain-free layer, the polarization measurement should return the symmetric shape following a $\cos^2 3\theta$ dependence. However, the fact that the shape in Figure 4.11 (a) is clearly distorted leads to the conclusion of stress in the layer. As a two-photon process, SHG is expected to have a quadratic intensity dependence on the incident light field. This is confirmed by the intensity measurement in Figure 4.11 (b) where the slope of 1.95 on a log-log scale confirms this nonlinearity. Like other optical excitation processes, SHG benefits by an increased probability when one of the light-fields is resonant on an actual excitation state in substrate [106]. And unlike TPPL, SHG is a coherent process that requires energy conservation between all interacting photons. Therefore, SHG probes excited states directly, which can be seen as a slight blue-shift of the SHG peak signal compared to the PL emission of the same excitonic state in Figure 4.11 (c).

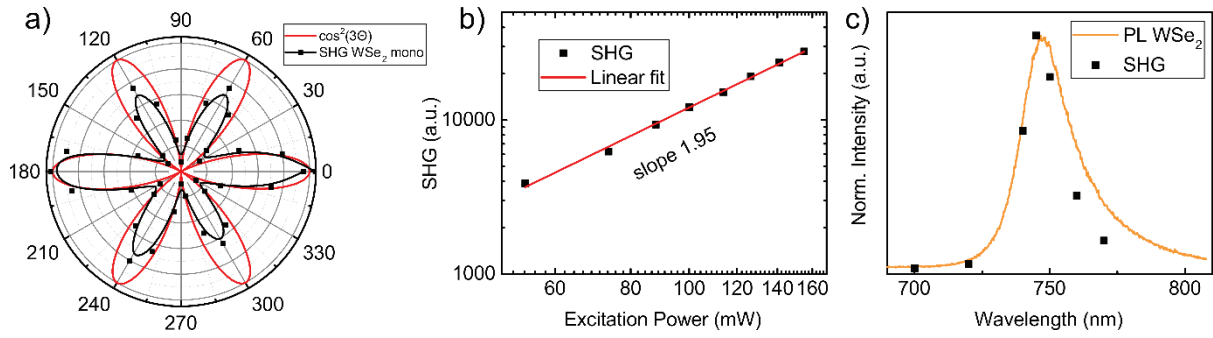


Figure 4.11. SHG of a WSe₂ monolayer. (a) Polarization dependent SHG (black squares). Black solid line is a guideline for visibility and the red line is the simulated polarization dependence. (b) SHG intensity against incident intensity on a log-log scale. (c) Tuning of the SHG signal over the A-exciton resonance plotted against PL on a normalized intensity scale.

TPPL, albeit also being a two-photon excitation process, is an incoherent process. The finally emitted photon has no fixed phase relation to the incident photons. Two photons of lower energy excite a molecule in a vibrationally and electronically excited state, see Figure 4.10. Subsequently, the molecule will relax via phonon emission to the electronically excited state and can finally relax to the molecular ground state through emission of a photon with higher energy than a single excitation photon. The main process is simple photoluminescence and the advantage of using two lower energy photons compared to a single higher energy photon is: First, infrared photons have a lower scattering probability, and in biological samples have a deeper penetration depth. Second the probability of a two-photon process is lower than for a one-photon process, which results in a lower background emission. TPPL from gold itself is a rather weak and inefficient process and a result of pumping the material above the interband transitions [158, 159]. A tremendous enhancement can be achieved when studying TPPL from surface defects and plasmonic nanoparticles [159-164], where the latter was done in *Paper IV*. As mentioned above, TPPL is an incoherent process, meaning that the phase of the interacting photons is not important. However, when the excitation of such a process happens on a timescale, shorter than the decoherence time of a plasmon oscillation, then the interaction between photons and a plasmon can result in a coherent TPPL response. This peculiarity has been demonstrated in *Paper IV*.

Four-wave mixing (FWM) depends on the third order nonlinear susceptibility and is the combination of three waves with a fourth one:

$$\pm\omega_1 \pm \omega_2 \pm \omega_3 = \omega_4 \quad (4.4)$$

FWM is a parametric process meaning it underlies energy conservation. Still, the number of possible combinations can be with 81 substantial and will always generate background signal [165]. Often the FWM process is reduced to degenerate FWM, whereby $\omega_1 = \omega_2$ which reduces possible combinations. Furthermore, some combinations are for symmetry reasons not allowed [165]. One of the most common combinations is illustrated in Figure 4.10. Knowing the individual frequencies and the fact that FWM is a parametric process, the emission frequency can be readily determined from expression (4.4). In practice, a spectrometer can be used to analyze the signal at this specific frequency (see Figure 4.14 (a)), or via a band-pass filter, only a single combination of possible processes can be singled-out. The probability for a third order process is expected to be lower, than for a second order nonlinear process. However, SHG had the strict requirement of the absence of an inversion symmetry, which is not necessary for a third order process. Furthermore, by having one or more of the participating wave-fields resonant on an electronic state or plasmon resonance, the signal one can enhance by several orders of magnitude [166-169].

When a molecule is excited by a laser, it will after a while relax to ground state. This relaxation can take place radiatively and non-radiatively. In Raman spectroscopy, the observed signal is photon emission from the molecule, after an inelastic scattering process with the incident photon. An energy transfer from the photon to the molecule can drive the molecule to an energetically higher vibrational state with energy Ω_{vib} and the released red-shifted photon has now the energy $\omega_{Stokes} = \omega_{incident} - \Omega_{vib}$. The inverse is also possible, though less likely, to transfer the energy of an already excited vibrational mode to the incident photon. The inelastic scattered blue-shifted photon is called anti-Stokes $\omega_{anti-Stokes,AS} = \omega_{incident} + \Omega_{vib}$. Collecting all inelastic scattered photons and knowing the incident photons energy, the phonon band of a molecule can be recreated. In principle, by focusing only on a single frequency it is possible to detect only molecules with this specific vibrational mode in a solution. However, the Raman process itself is incoherent and a rather weak process. In order to enhance the contrast and detection speed one can employ **coherent anti-Stokes Raman scattering (CARS)** microscopy [170]. CARS is basically degenerate FWM but resonant on a vibrational mode of a target molecule. By tuning the excitation frequencies, here called $\omega_{Pump \rightarrow P}$ and $\omega_{Stokes \rightarrow S}$, so that their difference matches a vibrational mode $\Omega_{vib} = \omega_P - \omega_S$, results in a resonant response of the nonlinear optical process. In CARS the resonant vibration is driven coherently,

increasing the efficiency of this process by several orders of magnitude compared to ordinary Raman microscopy [170], and thereby CARS is feasible for using it as an imaging technique. The final emission at the so-called anti-Stokes frequency is $\omega_{AS} = 2\omega_p - \omega_s$. The intensity in CARS depends nonlinearly on the pump beam's power as well as linearly on the probe's power, making power dependence measurements a popular tool for confirming the CARS process. The intensity is proportional to:

$$I_{CARS} \propto \left| \chi_{nonlinear \rightarrow NL}^{(3)} \right|^2 I_p^2 I_s \quad (4.5)$$

$$\begin{aligned} \left| \chi_{nonlinear \rightarrow NL}^{(3)} \right|^2 &= \left| \chi_{resonant \rightarrow R}^{(3)} + \chi_{nonresonant \rightarrow NR}^{(3)} \right|^2 \\ &= |\chi_{NR}|^2 + |\chi_R(\Omega)|^2 + 2\chi_{NR} \text{Re}\{\chi_R(\Omega)\} \end{aligned} \quad (4.6)$$

Where $\text{Re}\{\chi_R\}$ is the real part of the resonant term of the third order nonlinear susceptibility. The first term of (4.6) is independent of the vibrational mode Ω and is the result of an electronic response of the material, thereby leading to a constant non-resonant background [170]. The second term contains only resonant information and is the desired signal contribution. The second term furthermore shows a quadratic dependence of the CARS signal on the concentration of molecules in the excitation focus. The last term is a mixed term making any quantitative analysis of CARS very challenging. Nevertheless, CARS is a popular tool in biological imaging, due to its intrinsic chemical specificity and non-invasiveness, since no extra staining is needed [109, 171].

Note, that in the description of nonlinear processes phase mismatch of the interacting waves has not been considered. However, it is of utmost importance and most nonlinear microscopy methods require coherence and phase-matching. For example, the intensity of the CARS signal depends on [109]:

$$I_{CARS} \sim I_p^2 I_s \text{sinc}^2 \left(\frac{\Delta k L}{2} \right) \quad (4.7)$$

th $\Delta k = k_p - k_s + k_p - k_{as}$, the phase mismatch between all participating electromagnetic waves, L is the coherent interaction length inside the sample medium and $I_{p,s}$ are the incident intensities at the pump and Stokes wavelength, respectively. In a birefringent perfect crystal without any loss the coherence length could be arbitrarily large [152]. How critical phase-matching is, is demonstrated in Figure 4.12. A similar phase requirement is valid for all different coherent nonlinear microscopy techniques. In a colinear excitation setup, the

interaction length is limiting the efficiency and nonlinear crystals often are fabricated of short blocks with alternating orientation of the crystal axis for constructive interference, so-called quasi-phase matching [152]. To avoid the need of a perfect phase matching, all excitation light beams are focused through a high numerical aperture objective lens on the sample. Inside the focus area nearly all k -vectors are present and the phase-matching condition is relaxed [109].

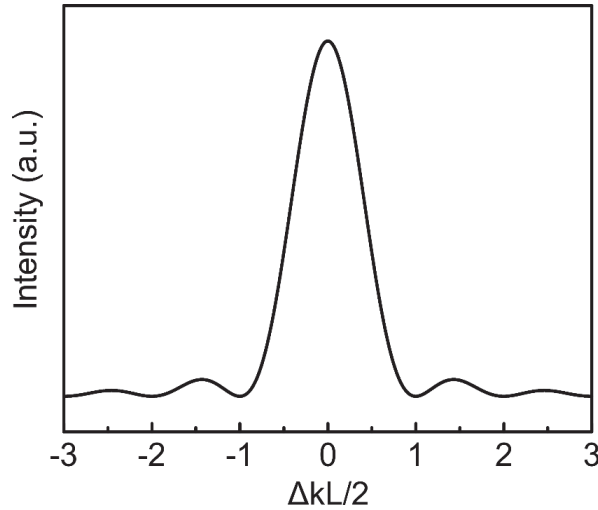


Figure 4.12. *Phase matching condition in nonlinear microscopy.*

4.8.2 Nonlinear laser microscope

The nonlinear laser microscope is illustrated in Figure 4.13. One or more pulsed excitation beams are focused onto the sample with a high numerical aperture (NA) objective lens. Three different laser sources have been employed throughout these studies:

First, a 76 MHz repetition rate laser with a pulse length of 7.5 ps (HighQ laser, picoTRAIN) with wavelength of 1064 nm, which has been employed as ω_2 in the methods in Figure 4.10. A frequency-doubled output was used to pump an optical parametric oscillator (OPO) (Levante, Emerald), where via parametric down-conversion a high energetic photon is split in two lower energy photons enabling wavelength tuning from 650 nm to 990 nm and furthermore 1100 nm to 1700 nm. The picoTRAIN has been used for all FWM measurements, including the CARS measurements for *Paper V*.

Second, a single-box version of the previous setup with 80 MHz repetition rate and 2 ps pulse length with one output at 1032 nm and a tunable second output between 700 nm and 990 nm and 1080 nm to 1950 nm (A.P.E. Berlin, picoEmerald S). The picoEmerald S was the replacement of the former and has been employed in the SHG experiments as described in the previous section.

Third, a 85 MHz repetition laser around 790 nm with a tunable pulse length down to 10 fs (Octavius 85M, Menlo Systems). The Octavius has been used to probe the coherent TPPL response with ultrashort pulses on gold nanorods in *Paper IV*.

Laser excitation and signal collection is done through the same high NA objective lens. A filter set, specific for each experiment blocks all excitation light, as well as possible background signals. An example is illustrated in the wavelength spectrum in Figure 4.13, where a band-pass filter can be used to filter out only the desired FWM or CARS signal, since both processes are coherent and feature a narrow bandwidth. Furthermore, by collecting and analyzing the desired emission frequency with a time-correlated single photon detector, coherent (instantaneous) and incoherent (depending of the life-time of an electronic state) processes can be distinguished. By applying time-gating and opening the detection window only for the short coherent processes, nearly all incoherent signals can be excluded, as seen in the life-time diagram in Figure 4.13. As single photon detectors either photomultiplier tubes (PMTs) or avalanche photodiodes (APDs) have been employed. The PMTs (Becker & Hickl, HPM-100-40) in combination with a time-correlated single photon counting (TCSPC) card (Becker & Hickl, SPC-150) offer a time-resolution of < 4 ps which corresponded to the pulse length of the equipped laser system.

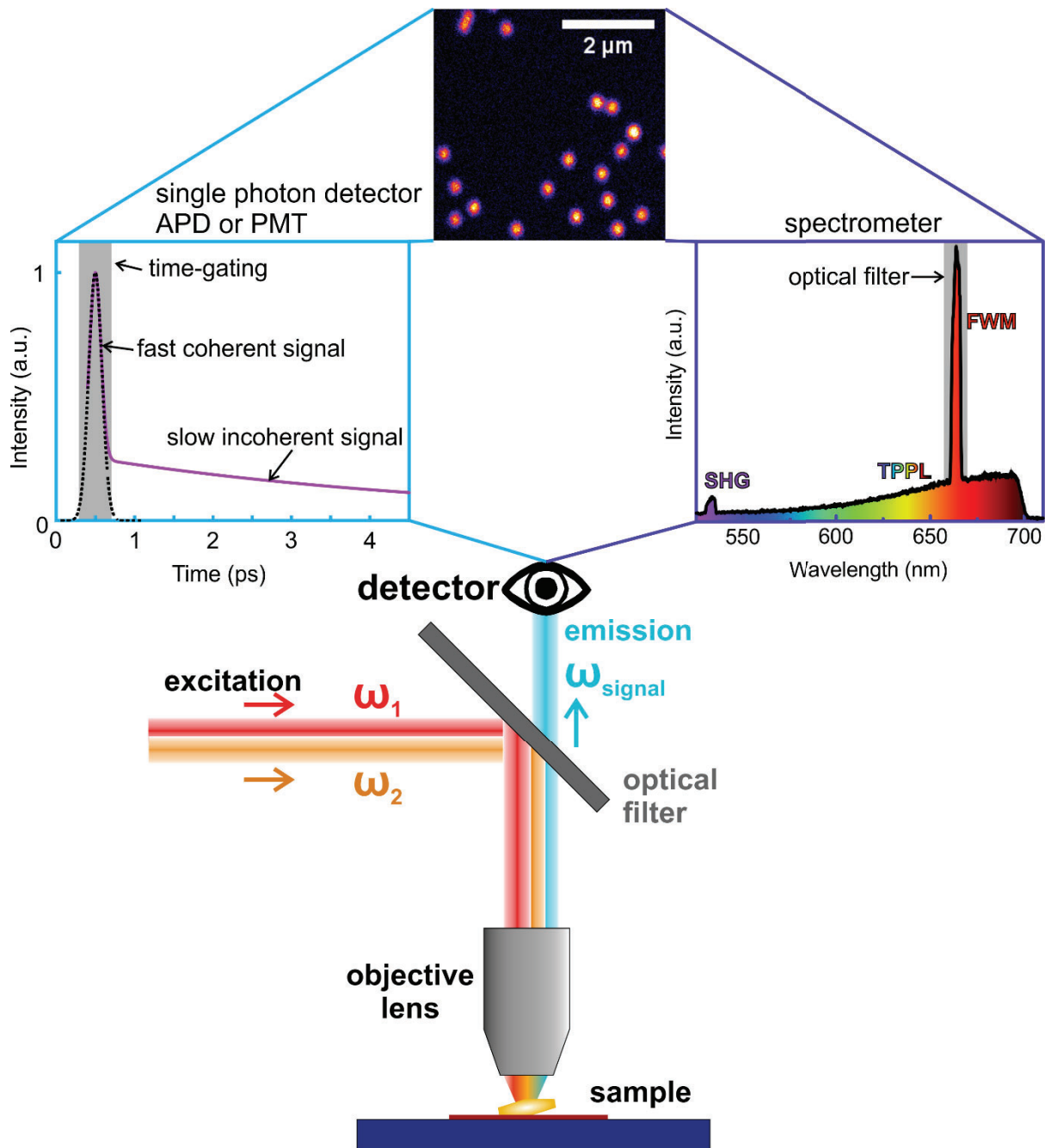


Figure 4.13. Nonlinear laser microscope. Excitation with pulsed laser light at frequencies ω_1 and ω_2 . A filter set enables detection of the desired emission signal. The detection takes place either via a spectrometer or via a time-correlated single photon detector. The image shows FWM intensity from a low density nanohole film with individual nanoholes.

4.8.2 Plasmon enhanced four-wave mixing

FWM is a third order nonlinear optical process, which means that the intensity of the signal depends on the coincidence of three phase-related photons. The probability for this is rather low. In order to modify and enhance the signal, one or more of the participating wave-fields can be tuned to the energy resonance of a localized plasmon. As described in section (2.2.2), when a plasmon is driven at resonance, the field will be squeezed into a small hotspot below the diffraction limit of light, where the electric field intensity is the strongest. The strong electric fields can boost the FWM by several orders of magnitude [166-169].

The plasmonic structure of interest in the studies for this thesis were nanoholes in an optically thin gold film. In the previous section (4.1.2) the fabrication of such a sample is described and several linear optical properties are shown and discussed. The extinction spectrum, shown in Figure 4.2 (c), indicates two different plasmon resonances, which are correlated to the hole geometry and nearest neighbor distance. The DF scattering spectra in Figure 4.2 (d) highlight the LSP resonance of an individual hole. FWM of such a gold film with nanoholes has been demonstrated by Hagman *et al.* [166], where they found different FWM intensities for films with different hole density and diameter. However, the analysis was restricted to high density nanohole films. The emission spectrum of a nanohole film with excitation at $\omega_1 = 817 \text{ nm}$ and $\omega_2 = 1064 \text{ nm}$ is shown in Figure 4.14 (a). The spectrum features two narrow peaks on a relative broad background. The two peaks can be easily identified as SHG and FWM signals respectively, since both are coherent parametric processes and are determined by $\omega_{SHG} = \omega_2 + \omega_2 = 2.33 \text{ eV} \approx 532 \text{ nm}$ and $\omega_{FWM} = \omega_1 + \omega_1 - \omega_2 = 1.87 \text{ eV} \approx 663 \text{ nm}$. The linewidth of each of the two processes is determined by the linewidth of the excitation laser, since no energy loss takes place in a coherent process, and ultimately by the resolution of the spectrometer. The broad background is the TPPL signal from the gold, which is further enhanced by the presence of the plasmon [159-164]. The signal is cut off at longer wavelength due to a set of filters that blocks all excitation wavelengths. Separation of the incoherent and coherent signals can be done by applying a narrow bandpass filter at the corresponding wavelengths (grey area in Figure 4.13 right hand side). Furthermore, incoherent processes depend on inelastic relaxation processes and the life-time of interacting electronic states in the material and have thereby a rather long life-time themselves. An interesting example can be found in *Paper IV*: The life-time of incoherent PL exceeds several picoseconds, compared to a coherent process that correlates to the plasmon decoherence time of a few femtoseconds. This

leads to another possibility to further distinguish between incoherent and coherent signal by employing time-gating (grey area in Figure 4.13 left hand side).

The FWM signal, when scanned over a small area of a high density nanohole film is shown in Figure 4.14 (b). The inset shows an SEM of the sample in a different area. The intensity distribution over the image indicates that some holes have a stronger FWM intensity while others show a weaker signal. Since two different localized plasmons are present in this interaction, the arising question is: Which plasmon oscillation is most crucial for this FWM process?

In order to answer this question, individual hole samples have been fabricated via HCL, as described in section (4.1.2). The concentration of beads in solution is lowered, resulting in a low density of holes in the final gold film. The distance between the holes is large enough to treat them as individual holes. FWM with fixed frequencies has been measured on different hole sizes. As a reminder the FWM intensity at the frequency $\omega_{FWM} = \omega_1 + \omega_1 - \omega_2$, has a square power depends on one of the two incident frequencies and is linear power dependent on the other. Two sets of measurements on nanoholes with different diameters in either a 20 nm thin gold film or 30 nm, etched down from a 300 nm or 200 nm sized plastic bead, respectively are plotted in Figure 4.14 (c).

As discussed in Chapter (2), a modified film or particle thickness shifts the resonance energy of the LSP resonance. This is evident by the two peaks in the intensity spectrum of the 20 nm gold film at 125 nm and 250 nm diameter, respectively. These maxima correspond well with the above-mentioned hypothesis of intensity dependence of the FWM signal. The first peak with a smaller hole diameter and corresponding higher energy LSPR, thereby can be identified as a plasmon resonance at the frequency of ω_1 . While the second maximum of the 250 nm holes corresponds to a plasmon frequency resonating at ω_2 . Another interesting observation is that the FWM intensity is clearly stronger on resonance with ω_1 , which is expected as this is the degenerate excitation frequency.

Finally, the linewidth of the first maximum for the LSPR at ω_1 is sharper than the linewidth for the second maximum at ω_2 . Two different effects could have the origin for this phenomenon. First, FWM depends quadratically on one of the excitation frequencies and linearly on the other. Second, larger diameter holes have a broader scattering resonance compared to smaller ones [78, 172].

The 30 *nm* thin film shows only a single maximum. Note that, the plasmon frequency shifts towards higher energies with an increasing film thickness. To achieve a resonance match with the same frequency ω_1 as in the thinner gold film, the corresponding hole diameter needs to be larger. And clearly, the peak intensity is found for a diameter of 160 *nm*, which corresponds to the 125 *nm* hole diameter in the 20 *nm* thin gold film. This set of measurements has been done by etching a different batch of plastic spheres with a starting diameter of 200 *nm*. The corresponding second maximum would be for nanoholes with a larger diameter than the initial starting size of the plastic spheres and was thereby out of the measurement scope. These values correspond well with work done previously in this group and other literature [63, 68, 75, 145, 166, 168, 172].

An alternative sample with individual nanoholes, fabricated via focused ion beam (FIB) milling is shown in Figure 4.14 (d). The diameter of the holes is kept constant and the image indicates a nearly equal intensity emitted from all individual holes. These results allow to speculate: Which of the two participating plasmons is most relevant? Being on resonance with the LSPR seems most relevant. When analyzing Figure 4.14 (b) and (d) and the data from (c), it is evident that nearly no FWM can be detected when no hole, and thereby no LPSR, is part of the light-matter interaction.

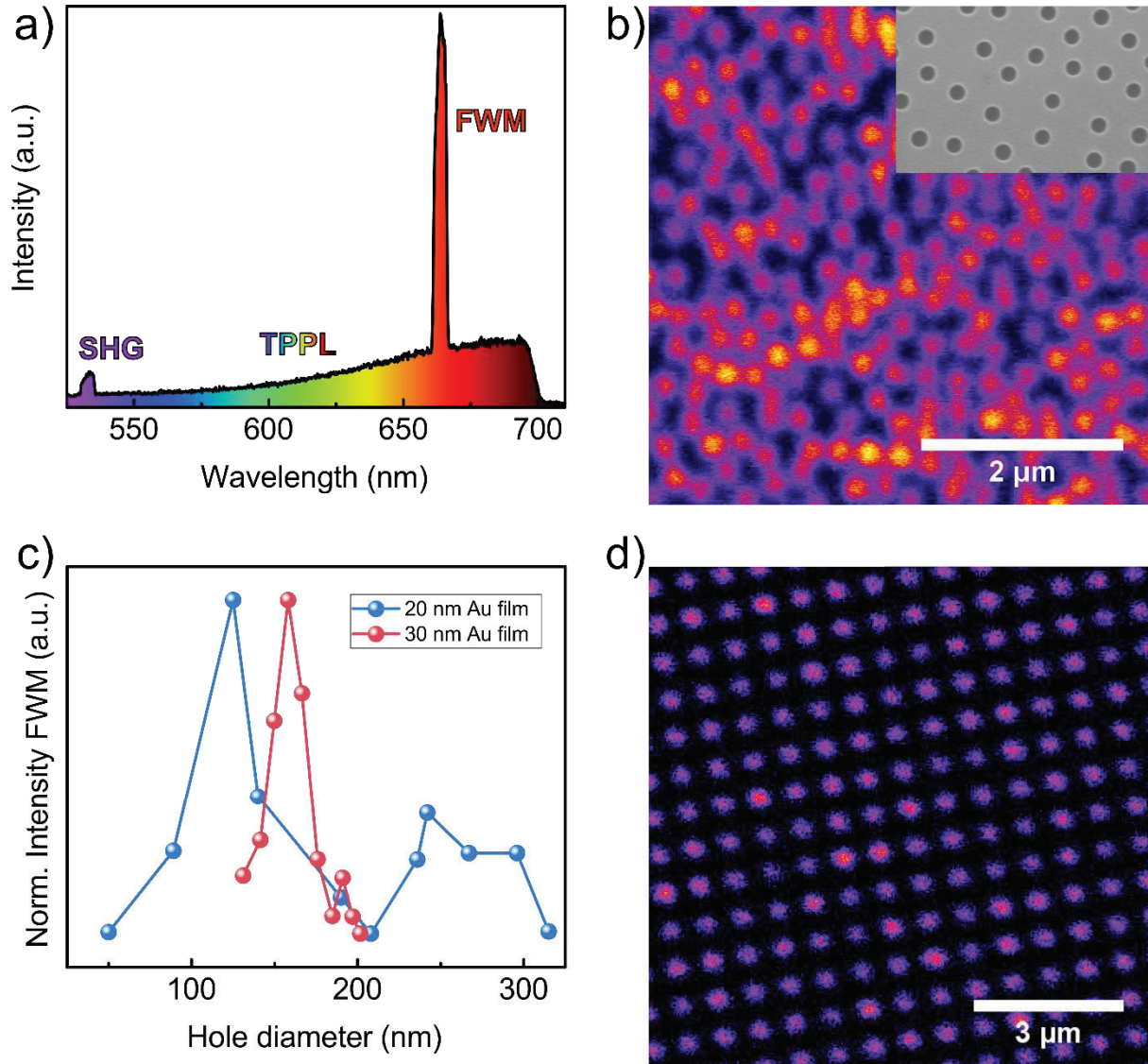


Figure 4.14. (a) Emission spectrum of a nanohole in a thin gold film excited in a FWM configuration. (b) FWM intensity of a thin gold film with a high density of nanoholes. Inset is an SEM image of such a sample with the same scale bar. (c) FWM intensity of individual nanoholes plotted against the hole diameter. (d) FWM of an array of holes with the same geometrical shape.

4.8.3 Near- and far-field microscopy

The original idea was to investigate the near-field of the FWM signal from a high-density nanohole gold film. Electric field intensities could be simulated, however, the quest of measuring experimentally the near-field distributions had not been done yet. Did the signal come from inside the hole, or from the edge? Are the SPP resonances strongly involved? Does signal emission only take inside a single hole, or also through scattering of the SPPs at neighboring holes? These and more questions were on the agenda.

The combination of nonlinear optical microscopy and a nanometer sized open-aperture tip for signal collection or excitation had been demonstrated by Namboodiri *et al.* and Schaller *et al.* [173, 174]. For this approach the sample has been excited with the 7.5 ps picoTRAIN laser and collection was done via an open aperture tip mounted on an AFM scanning stage (MultiView 2000TM, Nanonics). The scanning near-field optical microscopy (SNOM) was done with different open aperture tips, directly available from Nanonics with a diameter ranging from 50 nm to 500 nm. Note that, the transmission through a nano-sized aperture is $t \sim \left(\frac{r}{\lambda}\right)^4$, which means that only a small fraction of the total emitted signal will be collected. Furthermore, FWM is a third order nonlinear process, and albeit being on resonance with LSPRs the total signal is still relatively weak. Before the nonlinear experiments were conducted, a simple scan with the open aperture system over one of the laser beams in the focus region has been done. The effectiveness of SNOM, showing on a logarithmic scale the central part of the focus, as well as up to five Airy disk rings is demonstrated in Figure 4.15 (a). However, when switching to FWM no signal from the nanohole film could be detected through the open-aperture tip. The conclusion from these experiments is, that the peak power per pulse, which reflects the electric field intensity, was not high enough to generate enough nonlinear signal to be detectable. The previously mentioned works on near-field CARS, employed ultrafast lasers with a pulse length of only a few hundred femtoseconds, with up to several orders of magnitude shorter than the laser that was employed in the studies for this thesis.

A new approach was to reduce the order of nonlinearity to SHG and furthermore chose a sample that has a high nonlinear susceptibility. Nanorods made of lithium niobate (LiNbO₃) generate a high amount of SHG even under non-resonant excitation as can be seen in Figure 4.15 (b). Subsequently to the far-field SHG scan an open aperture tip ($d = 250$ nm) is brought in contact with the sample and positioned in the focus of the excitation beam. The sample is then

scanned via piezo-electric scanning of the sample-stage, assuring always good overlap between excitation beam and collection tip. After several low incident intensity trials, without being able to collect any signal, the incident laser intensity has been increased and the subsequent scan showed signal loss in the feedback for the scanning system. Conducting another far-field SHG measurement of the sample shows that the nanorod has been split in several pieces, see Figure 4.15 (c).

For further investigations the open aperture tip has been replaced with a standard AFM tip. Scanning the same sample with the same configuration, except now with an AFM tip, results in a repeatable non-destructive measurement. The combination of simultaneously scanning the topography and applying nonlinear optical microscopy, can directly relate geometrical shapes to the nonlinear optical properties. As evident when comparing Figure 4.15 (d) and (e), the higher SHG intensity at the end of the nanorod does not seem to be correlated to an edge scattering effect, but rather because the nanorod is much thicker. Since LiNbO_3 is a strong nonlinear optical crystal, this leads to the higher amount of SHG generation.

The interpretation of this leads to the following conclusion for the nonlinear SNOM experiments: The average laser power, necessary with a picosecond long laser pulse and high repetition rate, is too high for such an open aperture tip approach. The needed peak power to generate enough SHG photons per pulse is too low to be detected. Increasing the power, increases the average power and the heat generated inside the focus is too much and most likely damaging the tip, resulting in feedback loss for the scanner and subsequent sample damage. For the measurements with an AFM tip, the average incident power was lower, and furthermore the tip itself is much smaller, with a tip end curvature radius of $< 10 \text{ nm}$ compared to an open-aperture tip with a diameter of around $> 300 \text{ nm}$ (taking into account the aperture diameter plus cladding).

An example for topography measurements in combination with nonlinear laser microscopy can be seen in *Paper V*. There the topological features of a wrinkled hydrogel for cell growth have been investigated.

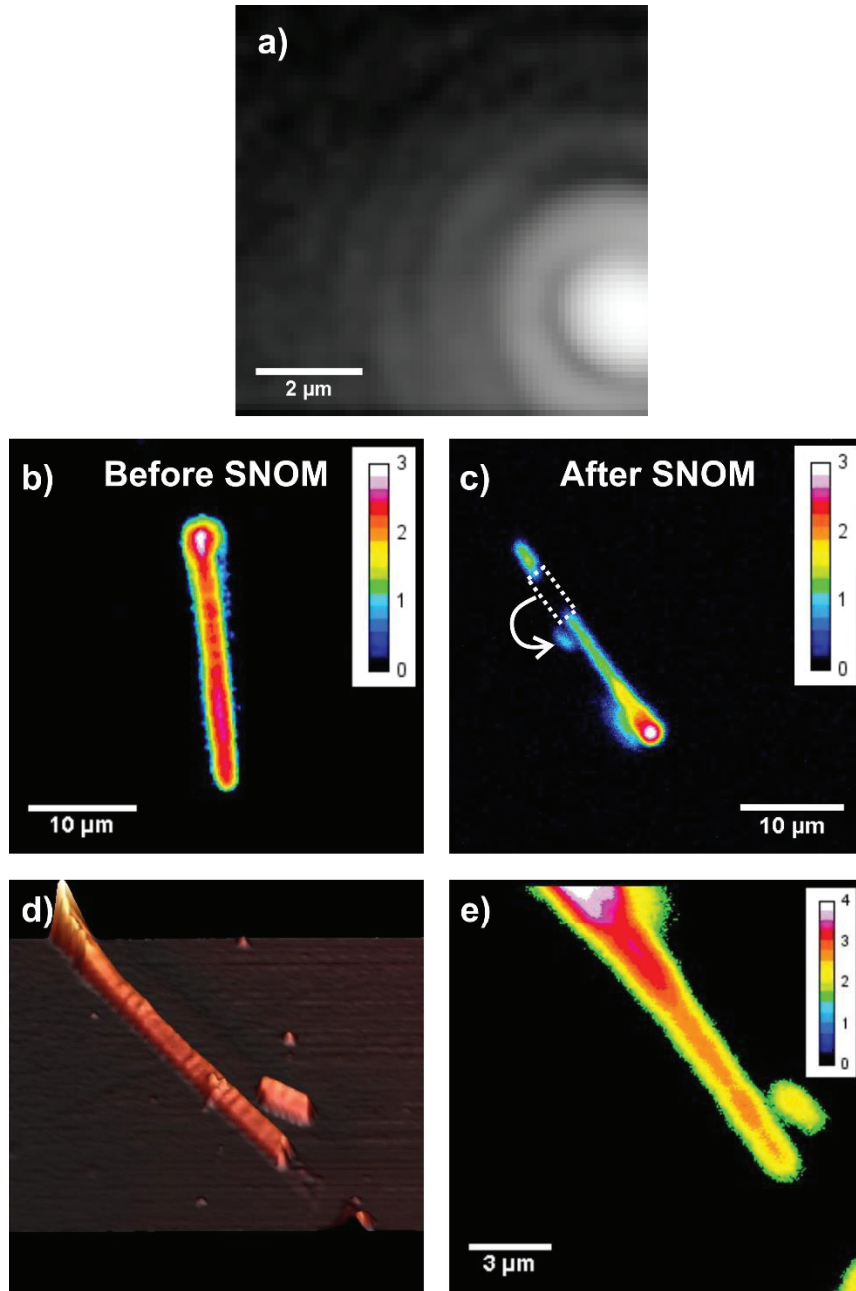


Figure 4.15. Results after nonlinear near-field experiments. (a) SNOM scan of the focus of a laser spot. Intensity is plotted on a log scale. (b), (c) Far-field SHG of a nanorod (b) before and (c) after SNOM experiments. The dashed white square marks an area where the SNOM tip destroyed the nanorod. (d), (e) Simultaneous scan of the same nanorod with (d) AFM and (e) far-field SHG. Scale bar in all SHG images is logarithmic.

Chapter 5: Summary and Outlook

In this Chapter, a short summary and discussion about each appended paper is given. It is a more personal reflection from the beginning of each project to the time of writing this thesis. As stated in the beginning of this thesis, lots of research still needs to be done in the single plasmonic particle strong coupling regime. Therefore, in this PhD project, the focus has been on single plasmonic particle studies with excitons in WSe₂ few-layers. The final goal would be to reach quantum optical processes at ambient conditions in an easily accessible open resonator system.

5.1 Discussion of appended papers

Paper I:

Strong light-matter coupling between plasmons in individual gold bi-pyramids and excitons in mono- and multilayer WSe₂

The goal is to reach single- or few-emitter strong coupling at ambient conditions in order to investigate quantum optical processes. One way to approach this goal is to move from closed optical cavities with large mode volumes to small plasmonic particles, where the coupling takes place mainly in the hot-spot region. As a short reminder, the coupling strength of a system depends on:

$$g = \mu_e \sqrt{N} |E_{vac}| \propto \mu_e \sqrt{\frac{N}{V_m}} \quad (5.1)$$

with E_{vac} and V_m being the vacuum field and the mode volume of the optical resonator, μ_e the transition dipole moment between the ground and excited state of an emitter and N is the number of emitters participating in the coupling process. Expression (5.1) shows, that in order to reach the strong coupling regime with a single or few emitters, one needs an emitter with a large transition dipole moment and a resonator with a small, nanoscopic mode volume. Several publications show strong coupling with individual plasmonic nanostructures, but they often feature several hot-spots interacting with the emitter material. The gold nanobipyramids have peculiar properties: Deposited on a flat substrate, only one of the two tips with a hot-spot, will

be in contact with the underlying emitter material. This reduces the whole strong light-matter interaction to a single hot-spot! With such a small nanoscopic mode volume, the other part of expression (5.1) is a strong dipole moment. TMDC mono and few-layer flakes have tightly bound excitons with strong dipole moments (in WS_2 it is estimated to be as high as $\mu_{\text{WS}_2} = 56 \text{ Debye}$) [175]. The LSPR of the bipyramid is tuned to the exciton resonance of WSe_2 , where the exciton transition dipole moment should be in the same order of magnitude as from WS_2 [42]. As a result, strong coupling of excitons in WSe_2 mono- and multilayer with plasmons in the BP is shown. The whole process takes place at ambient conditions and within a single hot-spot.

However, expression (5.1) does not take disorder and misalignment of excitons to the electric field of the plasmon into account. Furthermore, as shown in the paper, the coupling strength per individual exciton also depends on the position inside the hot-spot. This makes it in practice possible to extract an average coupling strength of all excitons, but impossible to determine a precise number of coupled excitons. The number of coupled excitons in this system can only be estimated to be somewhere between a few dozens and up to a hundred excitons.

Paper II:

Self-Hybridized Exciton-Polaritons in Multilayers of Transition Metal Dichalcogenides for Efficient Light Absorption

When exfoliating TMDC material from the bulk crystal and transferring it to the final substrate, often bigger multilayers with several hundred nanometer thickness are also transferred. Some of them showed very interesting colorful patterns, like Fabry-Pérot cavities. Indeed, first reflection measurements revealed that some flakes have optical cavity resonances. Furthermore, when the thickness of the flake, with corresponding cavity resonance, matches with its own exciton resonance, they strongly couple to each other. Two distinct dips in reflection can be attributed to the polaritonic states. This leads to a tremendous increase in absorption over the whole visible spectrum with potential applications in light-harvesting or photovoltaics.

My contributions for this study were of supporting nature with discussions and normal incidence reflection measurements. Furthermore, knowledge and access of topography

sensitive methods allowed to contribute with AFM measurements for determination of the thickness of the corresponding TMDC flakes, such as Figure 4.4.

Paper III:

Asymmetric photoluminescence from upper and lower polariton in a strongly coupled single nanoparticle plasmon mono- and bilayer WSe₂ system

This project is a follow-up study of *Paper I*, where the strongly coupled system, composed of plasmons in a BP and excitons in WSe₂, had been studied in a dark-field scattering configuration. Before, only elastic scattering processes had been investigated and it was shown that DF scattering shows the same polarization dependence as an uncoupled BP. In this project the study was extended to measuring the photoluminescence from the same strongly coupled system. Due to the formation of new hybrid states, a modified PL emission spectrum, as compared to uncoupled exciton PL, is expected. At zero plasmon-exciton detuning, the DF scattering spectrum indicates a balanced spectrum with two peaks of equal proportions. The UP and LP are composed each by the same plasmonic and excitonic fractions. However, PL from a strongly coupled system at zero detuning features an asymmetric emission spectrum between the upper and lower polariton. Most PL emission takes place at the LP energy position.

In this study, it is shown that the PL emission is always asymmetric and depends on the plasmon-exciton detuning. Furthermore, PL emission from the polaritons has the same polarization depends as DF scattering. This asymmetric emission is a result of phonon assisted relaxation pathways via a large number of incoherent dark states. These are unavailable in elastic scattering, which leads to the discrepancies between DF and PL spectra.

Paper IV:

Phase control of plasmon enhanced two-photon photoluminescence in resonant gold nanoantennas

This paper is a result of a collaboration with Professor Niek van Hulst at the Institute for Photonic Sciences (ICFO, Spain). It was the first time to get hands-on experience with an ultrafast few-femtoseconds laser system. The project pre-existed already in Niek's group with

some preliminary data. For a pure two-photon excitation process the probability scales with the inverse of the pulse duration. Gold nanorods have an intermediate short-lived state ($\sim 600\text{fs}$) and previous studies have shown that this state leads to a saturation for two-photon absorption (TPA) even for excitation pulses that are shorter [176]. However, these studies were limited to a shortest pulse length of $\sim 50\text{fs}$. For a pulse length in the order of the plasmon decoherence time (few tens of femtoseconds), the efficiency for a two-photon process increases again. This has led to the study of time-dependent coherence of TPPL of gold nanoantennas. The reason for another increase in two-photon excitation was the coherent driving force of the LSPR of the gold nanorod. In order to prove this, phase control experiments ranging from several hundred picoseconds down to $\sim 15\text{fs}$, have been conducted. And indeed, the experimental results demonstrated a coherent photoluminescence response in the ultra-short excitation regime and becomes incoherent for an excitation pulse-length longer than the plasmon decoherence-time. This project was very important to me, because these were the first successful nonlinear microscopy studies on plasmonic structures since the beginning of my PhD employment.

Paper V:

Micro- and nano-patterned elastin-like polypeptide hydrogels for stem cell culture

A huge topic in bio- and medical science is cell growth. Lots of effort is put in creating artificial structures that should mimic, in a controlled way, the natural environment of the cells of interest, to promote and potentially manipulate cell growth. After successfully establishing a setup for simultaneous collection of nonlinear optical signals and topography measurements via AFM (see Chapter (4.8.3)), this study was done in collaboration with the Heilshorn Biomaterials Group (Stanford University). They provided nano- and microwrinkled PDMS molds for fabricating the same structure in a hydrogel, which would be used for cell growth. The advantage of using multimodal nonlinear microscopy is to visualize different specific molecules simultaneously without the need of an external, potentially intrusive, marker. At the same time, AFM can be employed to study precise topological elements such as wrinkle size and periodicity, especially for subwavelength structures.

This study was my first publication and furthermore, gave me the opportunity to work with biological samples. To see, how the cells align on the final hydrogel substrate and move in

time, was a very different experience compared to the fixed metallic nanostructures in my other PhD projects.

5.2 Outlook

Single plasmonic particle strong coupling is still a rather young field in science. It combines areas of physics from quantum optics and material science. It enabled manipulation of photostability of molecules [29, 30] and coupling to a single molecule at room temperature [177, 178]. For several years, scientists have investigated the fundamental underlying processes of strong coupling and introduced many ways to model this kind of interaction. In this thesis only a few models with the focus on the classical field of physics, are discussed, such as the classical coupled oscillator model (COM, Chapter 3.2) and coupled mode theory (CMT, Chapter 3.3). However, many questions are still unanswered. In particular, for the effect of asymmetric PL emission from a strongly coupled system. Several different models were published recently [134-136], showing a strong interest by the scientific community. Furthermore, single- and few-emitter strong coupling to a plasmonic mode has recently been calculated via time-dependent density-functional theory [179], opening new theoretical possibilities for in-depth studies of polaritons.

While the goal of coupling an optical cavity to a single emitter has not been achieved with the systems studied in this thesis, García-Vidal et al. have indicated the possibility of retaining and enhancing nonlinearities, even if the number of emitters is large [180].

Additional to the linear excitation regime, a lot of interest is shown into studies of the nonlinear excitation regime of strongly coupled systems. From photon blockade [26] to enhanced second-harmonic generation [181] and third harmonic generation [182], many different investigations have been conducted on closed optical cavities. This inspired a set of first experiments on the strongly coupled system, as employed in this thesis. SHG from WSe₂ monolayers is a very efficient process and found its application for strain measurements and determination of the orientation of the crystal lattice in such TMDC few-layers, as discussed in Chapter 4.1. The SHG generation is most efficient when on resonance with the exciton absorption peak. Furthermore, it can be expected that the gold bipyramid will feature some SHG signal. A large

surface to volume ratio of the metal nanoparticle could lead to SHG generation at the metal-air interface. Owing to the plasmonic resonance, the SHG signal is expected to be enhanced, similar to the gold nanoantennas used in *Paper IV*. For the coupled system it is expected that the generated SHG signal will be maximized at the newly formed polariton frequencies, as shown by Chervy et al. [181]. Additionally, like DF scattering and PL emission, the SHG generation could be following the dipole orientation of the plasmonic particle. However, first experiments on the strongly coupled system with the picoEmerald S laser system did not result in enough meaningful data. The efficiency of a nonlinear process scales with the pulse length of the excitation laser, which in this case was rather long with 2 ps. Often, sample damage was found before enough data for clear interpretation could be collected. With a more sophisticated laser system for excitation, more experiments can be done. An interesting question to solve in this coupled system is the effect of the orientation of the BP towards the crystal lattice of the TMDC. Coupling of the excitons to the LSPR takes place independent of the orientation of the flake. However, in the SHG process, the crystal lattice plays a crucial role. Potentially a strong SHG enhancement for the coupled system at the polariton frequencies takes place only when the BP is aligned correctly towards the crystal lattice of WSe₂. Owing to the drop-casting method in the sample fabrication, the orientation of the BPs is random, and with enough particles it is possible to cover many angles. A different approach can be to employ an AFM tip to move the BPs on the sample as demonstrated in [183].

Often, elastic DF scattering is employed to study the strongly coupled system, which must be treated carefully. A splitting in a DF spectrum of a coupled system could be due to electromagnetic induced transparency. Therefore, PL offers a new route to studying the strongly coupled system to strengthen the possible conclusions. For *Paper III*, the study was limited to mono- and bilayers of WSe₂, due to the low PL emission from multilayer TMDCs. However, this also limits the study to emission mainly due to the excitonic material. Plasmonic gold nanoparticles also feature a photoluminescence response, as shown in *Paper IV*. The PL from the gold nanoparticle was unavailable in the study in *Paper III* with excitation via a white light LED source. With a short-pulsed laser excitation, the study could be extended to PL from a hybrid system composed of BPs coupled to thicker multilayer TMDC, where the PL emission would originate mainly from the gold nanoparticle.

Finally, in the study in *Paper I*, it is demonstrated that the mode volume is stronger located inside the TMDC with an increasing number of layers. A new pathway for increasing the

coupling efficiency could be to ‘flip’ the TMDC material around the BP tip. Thereby the overlap between the hotspot of the plasmonic BP and excitons in the TMDC material is improved.

Acknowledgements

This thesis could have not been without the tremendous support from my friends, colleagues and family. I am sitting here, writing the last lines in this thesis. I am overly exhausted, could sleep all day and can hardly focus on a full sentence. But deep down, I am super happy and satisfied that I did it. I can hardly believe it myself, but I actually managed to write a full PhD thesis! Reaching this goal, was a long and stony pathway through a labyrinth of obstacles, which didn't just lead to this thesis but also helped me finding myself. There were many times that I struggled, but even more people to help me up and continue.

For this I want to thank my colleagues and friends in the **Bionanophotonics group**. In particular:

- My examiner Professor **Mikael Käll**, for offering me shelter under his wings and taking care that I had enough time to finish a (decent) PhD.
- My supervisor Associate Professor **Timur Shegai**. After getting stuck in my previous PhD project you managed to offer me a new beginning. A new exciting project and many people who could help me out when in need. I might have not always been the ideal student, but together we managed to pull this off :-)
- **Battulga Munkhbat**, you had to suffer the longest. We joined at the same time and you had to survive through me complaining about everything for more than two years. You helped me constantly with experiments and discussions, even though you had 10-hour shifts. Kicking my butt to stay on track and focus on work work work ;-)
- **Ankit Bisht**, we started together, but you found your way out of Academia earlier, showing me, there is an exit. Also, the coolest Indian with your white shirt and sunglasses on our boat trip.
- **Luis Martins**, finally someone who complains more than me. The man with the constant smile on his face :-) How about another trip with an electric car in winter? And still, you never turned away when I had something to discuss. And many thanks for your book, now I know how humanity will end!
- **Betül Küçüköz**, thanks for encouraging me every day and listen to my mostly ridiculous questions about nature and life. Thanks for joining me every morning for a coffee, even though you often didn't need one.
- And of course, **Martin Wersäll**. The man, the Rockstar, the theoretical experimentalist, the legend, the myth. And the only Swede in Timurs group. Thanks for all your effort, even after you left for a new job. I still sometimes dream of our boat trips, and I hope that we can meet again in your amazing vacation stuga! And these ribs in home-made sauce prepared in the smoker..... Also, since your departure, I am the oldest group member, minus Timur, making me kind of a senior researcher :-)
- **Adriana Canales Ramos**, one of the strongest and smartest women in science. Thanks, for your constant positive attitude and smiles. Also, thanks for teaching me some theory stuff on my level.

- **Denis G. Baranov**, for delivering the theoretical support for my experiments and thanks for your fantastic 3D rendered images (the only reason why my paper is so awesome and gets citations).
- **Andreas Dahlin** and **Kunli Xiong** for helping me out with cleanroom fabrication methods.
- **Jorge Cuadra**, for answering the question: How much chill can a single person have?
- And all the other amazing people in the **Bionanophotonics group**, thank you for being part of my daily life, interesting discussions, and amazing kick-off meetings!

Was that all? Not even close, that barely covered the last two years of my PhD. My humble beginnings were in a completely different group. The first three years of my PhD were an emotional and scientific rollercoaster, and I am grateful to many persons who helped me finding a way through this time:

- **Alexandra Paul**, my longest friendship, you were with me from the very first day in Sweden. We suffered, we celebrated and even managed to write a paper together. We went together through all the ups and downs. And somehow you never left your aim out of sight. You always found your way to stay on track and reach your goal. I really admire that you fought for your own goals and even for others too. I hope your career will bring you far and that someday I can greet you with ‘Professor Paul’ :-)
- **Juris Kiskis**, thanks for all the help in the lab. Thank you for being a great colleague, friend and flat mate. You were a brilliant mind and I will always remember you.
- Also, I am deeply grateful for all the effort from Professor **Pernilla Wittung-Stafshede**. I still don’t know, how a single person can be so good and efficient. You took care of me when I had lost my way and worked hard on giving me everything I need to finish my PhD. You didn’t hesitate one second, even though it meant that I’ll leave not just your group but even for a completely different department. Thank you for believing in me.
- My first supervisor **Annika Enejder**, we had many differences on all kinds of levels, but you were the one person bringing me to Sweden and starting everything. For that I am grateful.
- The whole **FINON** project, where I met many awesome friends! Finally, with me graduating, this project is concluded :-)
- Professor **Niek van Hulst** and his group for an awesome time in Spain. It was a fantastic experience to work on an ultrafast laser on nanoparticles. I am sure that my schedule was a bit more relaxed compared to everybody else at ICFO, but this made my time there very special.
- Also, special thanks to my **friends in Germany**, I really miss our gaming evenings.... Can’t somebody quickly build a time-machine?

During my whole PhD, I met lots of nice friends and I am super happy that you all were part of my life here in Sweden: **Duong, Sebastian, Leo, Mahesh, Istvan, Sandra, Juan-Carlos, Nisha, Stephanie, Akanksha, Erik, ...** I could continue this list longer and longer, but it is getting late and the night is dark and full of terrors...

And finally, I want to thank my **family**, old and new. My parents **Regina** and **Klaus** for always supporting me, independent of which decision or direction I took. My siblings **Nicole, Tobias** and **Tabea** for teaching me how to share, forgive and hold together! My grandparents for an always open door and the constant little financial extra boost on nearly every occasion, while still reminding me on the reality: ‘You studied at the University, but what can you do?’

And most important my new family: **Diana Margarida da Costa Ribeiro**, love of my life, my Portuguese princess. You gave me so much more than I ever imagined! We started both in the same research group, unaware of what we will become. Then we went from colleagues to friends, to flat mates, to a couple and now even to parents! Which brings me to my other greatest achievement during my PhD: **Liam Maximilian Ribeiro Stührenberg**! You are the reason why I am super tired and exhausted. You took all my sleep... but gave me instead so much more in return. You taught me how to be patient (very patient) and to finally feel like I’m an adult! And every time I see your smile, everything is forgiven. You are the best thing (sorry, Diana) in my life!

And **Tiger**....wait, what? We have a cat? How did that happen? Typical, he just wanted to be the last....

BIBLIOGRAPHY

1. Helmholtz and H. Fripp, *On the Limits of the Optical Capacity of the Microscope*. The Monthly Microscopical Journal, 1876. **16**(1): p. 15-39.
2. Hon., A., *The Relation of Aperture and Power in the Microscope**. Journal of the Royal Microscopical Society, 1882. **2**(3): p. 300-309.
3. El-Sayed, I.H., X.H. Huang, and M.A. El-Sayed, *Selective laser photo-thermal therapy of epithelial carcinoma using anti-EGFR antibody conjugated gold nanoparticles*. Cancer Letters, 2006. **239**(1): p. 129-135.
4. He, H., C. Xie, and J. Ren, *Nonbleaching fluorescence of gold nanoparticles and its applications in cancer cell imaging*. Analytical Chemistry, 2008. **80**(15): p. 5951-5957.
5. Wu, X., et al., *High-Photoluminescence-Yield Gold Nanocubes: For Cell Imaging and Photothermal Therapy*. Acs Nano, 2010. **4**(1): p. 113-120.
6. Anker, J.N., et al., *Biosensing with plasmonic nanosensors*. Nature Materials, 2008. **7**(6): p. 442-453.
7. Zijlstra, P., J.W.M. Chon, and M. Gu, *Five-dimensional optical recording mediated by surface plasmons in gold nanorods*. Nature, 2009. **459**(7245): p. 410-413.
8. Akimov, A.V., et al., *Generation of single optical plasmons in metallic nanowires coupled to quantum dots*. Nature, 2007. **450**(7168): p. 402-406.
9. Kolesov, R., et al., *Wave-particle duality of single surface plasmon polaritons*. Nature Physics, 2009. **5**(7): p. 470-474.
10. Falk, A.L., et al., *Near-field electrical detection of optical plasmons and single-plasmon sources*. Nature Physics, 2009. **5**(7): p. 475-479.
11. Koller, D.M., et al., *Organic plasmon-emitting diode*. Nature Photonics, 2008. **2**(11): p. 684-687.
12. Chang, C., et al., *Efficient Solar-Thermal Energy Harvest Driven by Interfacial Plasmonic Heating-Assisted Evaporation*. Acs Applied Materials & Interfaces, 2016. **8**(35): p. 23412-23418.
13. Vieu, C., et al., *Electron beam lithography: resolution limits and applications*. Applied Surface Science, 2000. **164**: p. 111-117.
14. Hanarp, P., et al., *Control of nanoparticle film structure for colloidal lithography*. Colloids and Surfaces a-Physicochemical and Engineering Aspects, 2003. **214**(1-3): p. 23-36.
15. Fang, C.H., et al., *Facile Growth of High-Yield Gold Nanobipyramids Induced by Chloroplatinic Acid for High Refractive Index Sensing Properties*. Scientific Reports, 2016. **6**.

16. Li, Q., et al., *Production of Monodisperse Gold Nanobipyramids with Number Percentages Approaching 100% and Evaluation of Their Plasmonic Properties*. Advanced Optical Materials, 2015. **3**(6): p. 801-812.
17. Liu, M.Z. and P. Guyot-Sionnest, *Mechanism of silver(I)-assisted growth of gold nanorods and bipyramids*. Journal of Physical Chemistry B, 2005. **109**(47): p. 22192-22200.
18. Martinez-Torres, P.G., et al., *Facile Nanostructured Substrate Preparation Using Gold Nanocuboids for SERS*. Nanomaterials and Nanotechnology, 2015. **5**.
19. Purcell, E.M., *Spontaneous Emission Probabilities at Radio Frequencies*. Physical Review, 1946. **69**(11-1): p. 681-681.
20. Dulkeith, E., et al., *Fluorescence quenching of dye molecules near gold nanoparticles: Radiative and nonradiative effects*. Physical Review Letters, 2002. **89**(20).
21. Cao, E., et al., *Exciton-plasmon coupling interactions: from principle to applications*. Nanophotonics, 2018. **7**(1): p. 145-167.
22. Fano, U., *Atomic Theory of Electromagnetic Interactions in Dense Materials*. Physical Review, 1956. **103**(5): p. 1202-1218.
23. Hopfield, J.J., *Theory of the Contribution of Excitons to the Complex Dielectric Constant of Crystals*. Physical Review, 1958. **112**(5): p. 1555-1567.
24. Kaluzny, Y., et al., *Observation of Self-Induced Rabi Oscillations in 2-Level Atoms Excited inside a Resonant Cavity - the Ringing Regime of Super-Radiance*. Physical Review Letters, 1983. **51**(13): p. 1175-1178.
25. Volz, T., et al., *Ultrafast all-optical switching by single photons*. Nature Photonics, 2012. **6**(9): p. 605-609.
26. Birnbaum, K.M., et al., *Photon blockade in an optical cavity with one trapped atom*. Nature, 2005. **436**(7047): p. 87-90.
27. Khitrova, G., et al., *Vacuum Rabi splitting in semiconductors*. Nature Physics, 2006. **2**(2): p. 81-90.
28. Kasprzak, J., et al., *Bose-Einstein condensation of exciton polaritons*. Nature, 2006. **443**(7110): p. 409-414.
29. Munkhbat, B., et al., *Suppression of photo-oxidation of organic chromophores by strong coupling to plasmonic nanoantennas*. Science Advances, 2018. **4**(7).
30. Peters, V.N., et al., *Effect of strong coupling on photodegradation of the semiconducting polymer P3HT*. Optica, 2019. **6**(3): p. 318-325.
31. Schwartz, T., et al., *Reversible Switching of Ultrastrong Light-Molecule Coupling*. Physical Review Letters, 2011. **106**(19).

32. Shalabney, A., et al., *Coherent coupling of molecular resonators with a microcavity mode*. Nature Communications, 2015. **6**.
33. Thomas, A., et al., *Ground-State Chemical Reactivity under Vibrational Coupling to the Vacuum Electromagnetic Field*. Angewandte Chemie-International Edition, 2016. **55**(38): p. 11462-11466.
34. Galego, J., F.J. Garcia-Vidal, and J. Feist, *Suppressing photochemical reactions with quantized light fields*. Nature Communications, 2016. **7**.
35. Savasta, S., et al., *Nanopolaritons: Vacuum Rabi Splitting with a Single Quantum Dot in the Center of a Dimer Nanoantenna*. Acs Nano, 2010. **4**(11): p. 6369-6376.
36. Wu, X.H., S.K. Gray, and M. Pelton, *Quantum-dot-induced transparency in a nanoscale plasmonic resonator*. Optics Express, 2010. **18**(23): p. 23633-23645.
37. Christopoulos, S., et al., *Room-temperature polariton lasing in semiconductor microcavities*. Physical Review Letters, 2007. **98**(12).
38. Hakala, T.K., et al., *Bose-Einstein condensation in a plasmonic lattice*. Nature Physics, 2018. **14**(7): p. 739-+.
39. Geisler, M., et al., *Single-Crystalline Gold Nanodisks on WS₂ Mono- and Multilayers for Strong Coupling at Room Temperature*. Acs Photonics, 2019. **6**(4): p. 994-1001.
40. Kleemann, M.E., et al., *Strong-coupling of WSe₂ in ultra-compact plasmonic nanocavities at room temperature*. Nature Communications, 2017. **8**.
41. Wen, J.X., et al., *Room-Temperature Strong Light-Matter Interaction with Active Control in Single Plasmonic Nanorod Coupled with Two-Dimensional Atomic Crystals*. Nano Letters, 2017. **17**(8): p. 4689-4697.
42. Zheng, D., et al., *Manipulating Coherent Plasmon-Exciton Interaction in a Single Silver Nanorod on Monolayer WSe₂*. Nano Letters, 2017. **17**(6): p. 3809-3814.
43. Cuadra, J., et al., *Observation of Tunable Charged Exciton Polaritons in Hybrid Monolayer WS₂-Plasmonic Nanoantenna System*. Nano Letters, 2018. **18**(3): p. 1777-1785.
44. Schlather, A.E., et al., *Near-Field Mediated Plexcitonic Coupling and Giant Rabi Splitting in Individual Metallic Dimers*. Nano Letters, 2013. **13**(7): p. 3281-3286.
45. Wersall, M., et al., *Observation of Mode Splitting in Photoluminescence of Individual Plasmonic Nanoparticles Strongly Coupled to Molecular Excitons*. Nano Letters, 2017. **17**(1): p. 551-558.
46. Zengin, G., et al., *Realizing Strong Light-Matter Interactions between Single-Nanoparticle Plasmons and Molecular Excitons at Ambient Conditions*. Physical Review Letters, 2015. **114**(15).

47. Leng, H.X., et al., *Strong coupling and induced transparency at room temperature with single quantum dots and gap plasmons*. Nature Communications, 2018. **9**.
48. Melnikau, D., et al., *Rabi Splitting in Photoluminescence Spectra of Hybrid Systems of Gold Nanorods and J-Aggregates*. Journal of Physical Chemistry Letters, 2016. **7**(2): p. 354-362.
49. Weisbuch, C., et al., *Observation of the Coupled Exciton-Photon Mode Splitting in a Semiconductor Quantum Microcavity*. Physical Review Letters, 1992. **69**(23): p. 3314-3317.
50. Saleh, B.E.A. and M.C. Teich, *Fundamentals of Photonics*. 2007: Wiley.
51. Barth, M., et al., *Nanoassembled Plasmonic-Photonic Hybrid Cavity for Tailored Light-Matter Coupling*. Nano Letters, 2010. **10**(3): p. 891-895.
52. Srinivasan, K., M. Borselli, and O. Painter, *Cavity Q , mode volume, and lasing threshold in small diameter AlGaAs microdisks with embedded quantum dots*. Optics Express, 2006. **14**(3): p. 1094-1105.
53. Ebbesen, T.W., *Hybrid Light-Matter States in a Molecular and Material Science Perspective*. Accounts of Chemical Research, 2016. **49**(11): p. 2403-2412.
54. Schuller, J.A., et al., *Plasmonics for extreme light concentration and manipulation (vol 9, pg 193, 2010)*. Nature Materials, 2010. **9**(4).
55. Drude, P., *Zur Elektronentheorie der Metalle*. Annalen der Physik, 1900. **306**(3): p. 566-613.
56. Drude, P., *Zur Elektronentheorie der Metalle; II. Teil. Galvanomagnetische und thermomagnetische Effecte*. Annalen der Physik, 1900. **308**(11): p. 369-402.
57. Bohren, C.F. and D.R. Huffman, *Absorption and scattering of light by small particles*. 1983: Wiley.
58. Maier, S.A., *Plasmonics: Fundamentals and Applications*. 2007: Springer US.
59. Ashcroft, N.W. and N.D. Mermin, *Solid State Physics*. 1976: Cengage Learning.
60. Lässer R., S.N.V., *Interband optical transitions in gold in the photon energy range 2-25 eV*. Solid State Communications, 2002. **37**(6): p. 507-509.
61. Johnson, P.B. and R.W. Christy, *Optical Constants of the Noble Metals*. Physical Review B, 1972. **6**(12): p. 4370-4379.
62. Novotny, L., *Strong coupling, energy splitting, and level crossings: A classical perspective*. American Journal of Physics, 2010. **78**(11): p. 1199-1202.
63. Dahlin, A.B., et al., *Plasmonic Nanopores in Metal-Insulator-Metal Films*. Advanced Optical Materials, 2014. **2**(6): p. 556-564.

64. Joshi, G.K., et al., *Highly Specific Plasmonic Biosensors for Ultrasensitive MicroRNA Detection in Plasma from Pancreatic Cancer Patients*. Nano Letters, 2014. **14**(12): p. 6955-6963.
65. Larsson, E.M., S. Syrenova, and C. Langhammer, *Nanoplasmonic sensing for nanomaterials science*. Nanophotonics, 2012. **1**(3-4): p. 249-266.
66. Li, N., et al., *DNA-assembled bimetallic plasmonic nanosensors*. Light-Science & Applications, 2014. **3**.
67. Wadell, C., et al., *Hysteresis-Free Nanoplasmonic Pd-Au Alloy Hydrogen Sensors*. Nano Letters, 2015. **15**(5): p. 3563-3570.
68. Xiong, K.L., G. Emilsson, and A.B. Dahlin, *Biosensing using plasmonic nanohole arrays with small, homogenous and tunable aperture diameters*. Analyst, 2016. **141**(12): p. 3803-3810.
69. Mesch, M., et al., *Nonlinear Plasmonic Sensing*. Nano Letters, 2016. **16**(5): p. 3155-3159.
70. Miljkovic, V.D., et al., *Optical Forces in Plasmonic Nanoparticle Dimers*. Journal of Physical Chemistry C, 2010. **114**(16): p. 7472-7479.
71. Barnes, W.L., A. Dereux, and T.W. Ebbesen, *Surface plasmon subwavelength optics*. Nature, 2003. **424**(6950): p. 824-830.
72. Sambles, J.R., G.W. Bradbery, and F.Z. Yang, *Optical-Excitation of Surface-Plasmons - an Introduction*. Contemporary Physics, 1991. **32**(3): p. 173-183.
73. Ebbesen, T.W., et al., *Extraordinary optical transmission through sub-wavelength hole arrays*. Nature, 1998. **391**(6668): p. 667-669.
74. Bethe, H.A., *Theory of diffraction by small holes*. Physical Review, 1944. **66**(7/8): p. 163-182.
75. Sannomiya, T., et al., *Investigation of Plasmon Resonances in Metal Films with Nanohole Arrays for Biosensing Applications*. Small, 2011. **7**(12): p. 1653-1663.
76. Dahlin, A.B., et al., *Electrochemical Crystallization of Plasmonic Nanostructures*. Nano Letters, 2011. **11**(3): p. 1337-1343.
77. Junesch, J., T. Sannomiya, and A.B. Dahlin, *Optical Properties of Nanohole Arrays in Metal-Dielectric Double Films Prepared by Mask-on-Metal Colloidal Lithography*. ACS Nano, 2012. **6**(11): p. 10405-10415.
78. Priekulis, J., et al., *Optical spectroscopy of nanometric holes in thin gold films*. Nano Letters, 2004. **4**(6): p. 1003-1007.
79. Kang, E.S.H., H. Ekinge, and M.P. Jonsson, *Plasmonic fanoholes: on the gradual transition from suppressed to enhanced optical transmission through nanohole arrays*

- in metal films of increasing film thickness*. Optical Materials Express, 2019. **9**(3): p. 1404-1415.
80. Yang, P.F., et al., *Thickness Tunable Wedding-Cake-like MoS₂ Flakes for High-Performance Optoelectronics*. Acs Nano, 2019. **13**(3): p. 3649-3658.
 81. Lopez-Sanchez, O., et al., *Ultrasensitive photodetectors based on monolayer MoS₂*. Nature Nanotechnology, 2013. **8**(7): p. 497-501.
 82. Blauth, M., et al., *Ultracompact Photodetection in Atomically Thin MoSe₂*. ACS Photonics, 2019. **6**(8): p. 1902-1909.
 83. Ross, J.S., et al., *Electrically tunable excitonic light-emitting diodes based on monolayer WSe₂ p-n junctions*. Nature Nanotechnology, 2014. **9**(4): p. 268-272.
 84. Zhang, Y.J., et al., *Electrically Switchable Chiral Light-Emitting Transistor*. Science, 2014. **344**(6185): p. 725-728.
 85. Sumesh, C.K., *Towards efficient photon management in nanostructured solar cells: Role of 2D layered transition metal dichalcogenide semiconductors*. Solar Energy Materials and Solar Cells, 2019. **192**: p. 16-23.
 86. Bromley, R.A., A.D. Yoffe, and R.B. Murray, *Band Structures of Some Transition-Metal Dichalcogenides .3. Group VI a - Trigonal Prism Materials*. Journal of Physics Part C Solid State Physics, 1972. **5**(7): p. 759-&.
 87. Frindt, R.F., *Single Crystals of Mos₂ Several Molecular Layers Thick*. Journal of Applied Physics, 1966. **37**(4): p. 1928-&.
 88. Ribeiro-Soares, J., et al., *Group theory analysis of phonons in two-dimensional transition metal dichalcogenides*. Physical Review B, 2014. **90**(11).
 89. Alexeev, E.M., et al., *Resonantly hybridized excitons in moire superlattices in van der Waals heterostructures*. Nature, 2019. **567**(7746): p. 81-+.
 90. Jin, C.H., et al., *Observation of moire excitons in WSe₂/WS₂ heterostructure superlattices*. Nature, 2019. **567**(7746): p. 76-+.
 91. Ruiz-Tijerina, D.A. and V.I. Fal'ko, *Interlayer hybridization and moire superlattice minibands for electrons and excitons in heterobilayers of transition-metal dichalcogenides*. Physical Review B, 2019. **99**(12).
 92. Seyler, K.L., et al., *Signatures of moire-trapped valley excitons in MoSe₂/WSe₂ heterobilayers*. Nature, 2019. **567**(7746): p. 66-+.
 93. Tran, K., et al., *Evidence for moire excitons in van der Waals heterostructures*. Nature, 2019. **567**(7746): p. 71-+.
 94. Zhang, N., et al., *Moire Intralayer Excitons in a MoSe₂/MoS₂ Heterostructure*. Nano Letters, 2018. **18**(12): p. 7651-7657.

95. He, K.L., et al., *Tightly Bound Excitons in Monolayer WSe₂*. Physical Review Letters, 2014. **113**(2).
96. Li, Y.L., et al., *Measurement of the optical dielectric function of monolayer transition-metal dichalcogenides: MoS₂, MoSe₂, WS₂, and WSe₂*. Physical Review B, 2014. **90**(20).
97. Ramasubramaniam, A., *Large excitonic effects in monolayers of molybdenum and tungsten dichalcogenides*. Physical Review B, 2012. **86**(11).
98. Rasmussen, F.A. and K.S. Thygesen, *Computational 2D Materials Database: Electronic Structure of Transition-Metal Dichalcogenides and Oxides*. Journal of Physical Chemistry C, 2015. **119**(23): p. 13169-13183.
99. Yan, T.F., et al., *Photoluminescence properties and exciton dynamics in monolayer WSe₂*. Applied Physics Letters, 2014. **105**(10).
100. Zeng, H.L., et al., *Optical signature of symmetry variations and spin-valley coupling in atomically thin tungsten dichalcogenides*. Scientific Reports, 2013. **3**.
101. Arora, A., et al., *Excitonic resonances in thin films of WSe₂: from monolayer to bulk material*. Nanoscale, 2015. **7**(23): p. 10421-10429.
102. Fox, A.M. and D.P.A.M. Fox, *Optical Properties of Solids*. 2001: Oxford University Press.
103. Chernikov, A., et al., *Exciton Binding Energy and Nonhydrogenic Rydberg Series in Monolayer WS₂*. Physical Review Letters, 2014. **113**(7).
104. Cheiwchanchamnangij, T. and W.R.L. Lambrecht, *Quasiparticle band structure calculation of monolayer, bilayer, and bulk MoS₂*. Physical Review B, 2012. **85**(20).
105. Qiu, D.Y., F.H. da Jornada, and S.G. Louie, *Optical Spectrum of MoS₂: Many-Body Effects and Diversity of Exciton States*. Physical Review Letters, 2013. **111**(21).
106. Wang, G., et al., *Giant Enhancement of the Optical Second-Harmonic Emission of WSe₂ Monolayers by Laser Excitation at Exciton Resonances*. Physical Review Letters, 2015. **114**(9).
107. Lidzey, D.G., et al., *Strong exciton-photon coupling in an organic semiconductor microcavity*. Nature, 1998. **395**(6697): p. 53-55.
108. Torma, P. and W.L. Barnes, *Strong coupling between surface plasmon polaritons and emitters: a review*. Reports on Progress in Physics, 2015. **78**(1).
109. Cheng, J.X. and X.S. Xie, *Coherent Raman Scattering Microscopy*. 2016: CRC Press.
110. Wadell, C., T.J. Antosiewicz, and C. Langhammer, *Optical Absorption Engineering in Stacked Plasmonic Au-SiO₂-Pd Nanoantennas*. Nano Letters, 2012. **12**(9): p. 4784-4790.

111. Haus, H.A., *Waves and fields in optoelectronics*. 1984: Prentice Hall, Incorporated.
112. Fan, S.H., W. Suh, and J.D. Joannopoulos, *Temporal coupled-mode theory for the Fano resonance in optical resonators*. Journal of the Optical Society of America a-Optics Image Science and Vision, 2003. **20**(3): p. 569-572.
113. Gerry, C., P. Knight, and P.L. Knight, *Introductory Quantum Optics*. 2005: Cambridge University Press.
114. Walls, D.F. and G.J. Milburn, *Quantum optics*. 1995: Springer-Verlag.
115. Baranov, D.G., et al., *Novel Nanostructures and Materials for Strong Light Matter Interactions*. Acs Photonics, 2018. **5**(1): p. 24-42.
116. Zengin, G., et al., *Approaching the strong coupling limit in single plasmonic nanorods interacting with J-aggregates*. Scientific Reports, 2013. **3**.
117. Antosiewicz, T.J., S.P. Apell, and T. Shegai, *Plasmon-Exciton Interactions in a Core-Shell Geometry: From Enhanced Absorption to Strong Coupling*. Acs Photonics, 2014. **1**(5): p. 454-463.
118. Rajendran, S.K., et al., *Direct evidence of Rabi oscillations and antiresonance in a strongly coupled organic microcavity*. Physical Review B, 2015. **91**(20).
119. Heiss, W.D., *Repulsion of resonance states and exceptional points*. Physical Review E, 2000. **61**(1): p. 929-932.
120. Stührenberg, M., et al., *Strong Light-Matter Coupling between Plasmons in Individual Gold Bi-pyramids and Excitons in Mono- and Multilayer WSe₂*. Nano Letters, 2018. **18**(9): p. 5938-5945.
121. Murata, N., R. Hata, and H. Ishihara, *Crossover between Energy Transparency Resonance and Rabi Splitting in Antenna-Molecule Coupled Systems*. Journal of Physical Chemistry C, 2015. **119**(45): p. 25493-25498.
122. Wang, G., et al., *Colloquium: Excitons in atomically thin transition metal dichalcogenides*. Reviews of Modern Physics, 2018. **90**(2).
123. Palummo, M., M. Bernardi, and J.C. Grossman, *Exciton Radiative Lifetimes in Two-Dimensional Transition Metal Dichalcogenides*. Nano Letters, 2015. **15**(5): p. 2794-2800.
124. Gehlhaar, R., et al., *Time-resolved and cw photoluminescence from strongly coupled organic microcavities*. Journal of Luminescence, 2004. **110**(4): p. 354-358.
125. Agranovich, V., H. Benisty, and C. Weisbuch, *Organic and inorganic quantum wells in a microcavity: Frenkel-Wannier-Mott excitons hybridization and energy transformation*. Solid State Communications, 1997. **102**(8): p. 631-636.

126. Guebrou, S.A., et al., *Coherent Emission from a Disordered Organic Semiconductor Induced by Strong Coupling with Surface Plasmons*. Physical Review Letters, 2012. **108**(6).
127. Agranovich, V.M., M. Litinskaia, and D.G. Lidzey, *Cavity polaritons in microcavities containing disordered organic semiconductors*. Physical Review B, 2003. **67**(8).
128. Litinskaya, M., P. Reineker, and V.M. Agranovich, *Fast polariton relaxation in strongly coupled organic microcavities*. Journal of Luminescence, 2004. **110**(4): p. 364-372.
129. Litinskaya, M., P. Reineker, and V.M. Agranovich, *Exciton-polaritons in organic microcavities*. Journal of Luminescence, 2006. **119**: p. 277-282.
130. Coles, D.M., et al., *Vibrationally Assisted Polariton-Relaxation Processes in Strongly Coupled Organic-Semiconductor Microcavities*. Advanced Functional Materials, 2011. **21**(19): p. 3691-3696.
131. Lidzey, D.G., et al., *Hybrid polaritons in strongly coupled microcavities: experiments and models*. Journal of Luminescence, 2004. **110**(4): p. 347-353.
132. Michetti, P. and G.C. La Rocca, *Polariton states in disordered organic microcavities*. Physical Review B, 2005. **71**(11).
133. Michetti, P. and G.C. La Rocca, *Simulation of J-aggregate microcavity photoluminescence*. Physical Review B, 2008. **77**(19).
134. Herrera, F. and F.C. Spano, *Dark Vibronic Polaritons and the Spectroscopy of Organic Microcavities*. Physical Review Letters, 2017. **118**(22).
135. Neuman, T. and J. Aizpurua, *Origin of the asymmetric light emission from molecular exciton-polaritons*. Optica, 2018. **5**(10): p. 1247-1255.
136. del Pino, J., et al., *Tensor Network Simulation of Non-Markovian Dynamics in Organic Polaritons*. Physical Review Letters, 2018. **121**(22).
137. Scherer, P. and S.F. Fischer, *The Displaced Harmonic Oscillator Model*, in *Theoretical Molecular Biophysics*. 2010, Springer Berlin Heidelberg: Berlin, Heidelberg. p. 205-208.
138. Castellanos-Gomez, A., et al., *Deterministic transfer of two-dimensional materials by all-dry viscoelastic stamping*. 2d Materials, 2014. **1**(1).
139. Antonelou, A., et al., *MoS₂/h-BN heterostructures: controlling MoS₂ crystal morphology by chemical vapor deposition*. Journal of Materials Science, 2017. **52**(12): p. 7028-7038.
140. Shree, S., et al., *Accessing high optical quality of MoS₂ monolayers grown by chemical vapor deposition*. arXiv preprint arXiv:1907.03342, 2019.

141. Kobayashi, Y., et al., *Growth and Optical Properties of High-Quality Monolayer WS₂ on Graphite*. *Acs Nano*, 2015. **9**(4): p. 4056-4063.
142. Liu, J., et al., *A comprehensive comparison study on the vibrational and optical properties of CVD-grown and mechanically exfoliated few-layered WS₂*. *Journal of Materials Chemistry C*, 2017. **5**(43): p. 11239-11245.
143. Zhang, Y., et al., *Controlled Growth of High-Quality Monolayer WS₂ Layers on Sapphire and Imaging Its Grain Boundary*. *Acs Nano*, 2013. **7**(10): p. 8963-8971.
144. Li, Q.Y., et al., *Patterning Poly(dimethylsiloxane) Microspheres via Combination of Oxygen Plasma Exposure and Solvent Treatment*. *Journal of Physical Chemistry B*, 2015. **119**(42): p. 13450-13461.
145. Park, T.H., et al., *Optical properties of a nanosized hole in a thin metallic film*. *Acs Nano*, 2008. **2**(1): p. 25-32.
146. Kou, X.S., et al., *Growth of gold bipyramids with improved yield and their curvature-directed oxidation*. *Small*, 2007. **3**(12): p. 2103-2113.
147. Chow, T.H., et al., *Gold Nanobipyramids: An Emerging and Versatile Type of Plasmonic Nanoparticles*. *Acc Chem Res*, 2019. **52**(8): p. 2136-2146.
148. Mason, S., *Lines of light: The sources of dispersive spectroscopy, 1800-1930 - Brand, JCD*. *Nature*, 1996. **381**(6582): p. 488-488.
149. Beeckman, J., K. Neyts, and P.J.M. Vanbrabant, *Liquid-crystal photonic applications*. *Optical Engineering*, 2011. **50**(8).
150. Kopp, G., *Tunable Birefringent Filters Using Liquid Crystal Variable Retarders*. *Polarization Analysis and Measurement II*, 1994. **2265**: p. 193-201.
151. Morris, H.R., C.C. Hoyt, and P.J. Treado, *Imaging Spectrometers for Fluorescence and Raman Microscopy - Acoustooptic and Liquid-Crystal Tunable Filters*. *Applied Spectroscopy*, 1994. **48**(7): p. 857-866.
152. Boyd, R.W., *Nonlinear Optics*. 2013: Elsevier Science.
153. Mennel, L., M. Paur, and T. Mueller, *Second harmonic generation in strained transition metal dichalcogenide monolayers: MoS₂, MoSe₂, WS₂, and WSe₂*. *Apl Photonics*, 2019. **4**(3).
154. Ribeiro-Soares, J., et al., *Second Harmonic Generation in WSe₂*. *2d Materials*, 2015. **2**(4).
155. Seyler, K.L., et al., *Electrical control of second-harmonic generation in a WSe₂ monolayer transistor*. *Nature Nanotechnology*, 2015. **10**(5): p. 407-411.
156. Xia, J., J.X. Yan, and Z.X. Shen, *Transition metal dichalcogenides: structural, optical and electronic property tuning via thickness and stacking*. *Flatchem*, 2017. **4**: p. 1-19.

157. Mennel, L., et al., *Optical imaging of strain in two-dimensional crystals*. Nature Communications, 2018. **9**.
158. Mooradian, A., *Photoluminescence of Metals*. Physical Review Letters, 1969. **22**(5): p. 185-+.
159. Zheng, J., et al., *Different sized luminescent gold nanoparticles*. Nanoscale, 2012. **4**(14): p. 4073-4083.
160. Beversluis, M.R., A. Bouhelier, and L. Novotny, *Continuum generation from single gold nanostructures through near-field mediated intraband transitions*. Physical Review B, 2003. **68**(11).
161. Boyd, G.T., Z.H. Yu, and Y.R. Shen, *Photoinduced Luminescence from the Noble-Metals and Its Enhancement on Roughened Surfaces*. Physical Review B, 1986. **33**(12): p. 7923-7936.
162. Castro-Lopez, M., et al., *Aluminum for Nonlinear Plasmonics: Resonance-Driven Polarized Luminescence of Al, Ag, and Au Nanoantennas*. Nano Letters, 2011. **11**(11): p. 4674-4678.
163. Ko, K.D., et al., *Investigation of the nonlinear optical response from arrays of Au bowtie nanoantennas*. Photonic and Phononic Properties of Engineered Nanostructures, 2011. **7946**.
164. van Nieuwstadt, J.A.H., et al., *Strong modification of the nonlinear optical response of metallic subwavelength hole arrays*. Physical Review Letters, 2006. **97**(14).
165. Levenson, M.D., *Introduction to nonlinear laser spectroscopy*. 1982: Academic Press.
166. Hagman, H., et al., *Plasmon-enhanced four-wave mixing by nanoholes in thin gold films*. Optics Letters, 2014. **39**(4): p. 1001-1004.
167. Jin, B.Y. and C. Argyropoulos, *Enhanced four-wave mixing with nonlinear plasmonic metasurfaces*. Scientific Reports, 2016. **6**.
168. Subramaniam, N., et al., *Nonlinear plasmonic behavior of nanohole arrays in thin gold films for imaging lipids*. Applied Physics Letters, 2018. **112**(23).
169. Cox, J.D. and F.J.G. de Abajo, *Plasmon-Enhanced Nonlinear Wave Mixing in Nanostructured Graphene*. Acs Photonics, 2015. **2**(2): p. 306-312.
170. Evans, C.L. and X.S. Xie, *Coherent Anti-Stokes Raman Scattering Microscopy: Chemical Imaging for Biology and Medicine*. Annual Review of Analytical Chemistry, 2008. **1**: p. 883-909.
171. Yue, S.H., M.N. Slipchenko, and J.X. Cheng, *Multimodal nonlinear optical microscopy*. Laser & Photonics Reviews, 2011. **5**(4): p. 496-512.
172. Rindzevicius, T., et al., *Nanohole plasmons in optically thin gold films*. Journal of Physical Chemistry C, 2007. **111**(3): p. 1207-1212.

173. Namboodiri, M., et al., *Scanning near-field optical coherent anti-Stokes Raman microscopy (SNOM-CARS) with femtosecond laser pulses in vibrational and electronic resonance*. Optics Express, 2013. **21**(1): p. 918-926.
174. Schaller, R.D., et al., *Chemically selective imaging of subcellular structure in human hepatocytes with coherent anti-stokes Raman scattering (CARS) near-field scanning optical microscopy (NSOM)*. Journal of Physical Chemistry B, 2002. **106**(34): p. 8489-8492.
175. Sie, E.J., et al., *Valley-selective optical Stark effect in monolayer WS₂*. Nature Materials, 2015. **14**(3): p. 290-294.
176. Biagioni, P., et al., *Dependence of the two-photon photoluminescence yield of gold nanostructures on the laser pulse duration*. Physical Review B, 2009. **80**(4).
177. Chikkaraddy, R., et al., *Single-molecule strong coupling at room temperature in plasmonic nanocavities*. Nature, 2016. **535**(7610): p. 127-130.
178. Santhosh, K., et al., *Vacuum Rabi splitting in a plasmonic cavity at the single quantum emitter limit*. Nature Communications, 2016. **7**.
179. Rossi, T.P., et al., *Strong plasmon-molecule coupling at the nanoscale revealed by first-principles modeling*. Nature Communications, 2019. **10**.
180. Saez-Blazquez, R., et al., *Enhancing photon correlations through plasmonic strong coupling*. Optica, 2017. **4**(11): p. 1363-1367.
181. Chervy, T., et al., *High-Efficiency Second-Harmonic Generation from Hybrid Light Matter States*. Nano Letters, 2016. **16**(12): p. 7352-7356.
182. Barachati, F., et al., *Tunable Third-Harmonic Generation from Polaritons in the Ultrastrong Coupling Regime*. Acs Photonics, 2018. **5**(1): p. 119-125.
183. Sivun, D., et al., *Anticorrelation of Photoluminescence from Gold Nanoparticle Dimers with Hot-Spot Intensity*. Nano Letters, 2016. **16**(11): p. 7203-7209.